Ruthenium dissolution in direct methanol fuel cells

Dipl.-Phys. Alexander Schökel

TECHNISCHE
UNIVERSITÄT
DARMSTADT

Ruthenium dissolution in direct methanol fuel cells

Vom Fachbereich Material- und Geowissenschaften

der Technischen Universität Darmstadt

zur Erlangung des Grades

eines Doktors der Naturwissenschaften

(Dr. rer. nat.)

genehmigte Dissertation

von Dipl.-Phys. Alexander Schökel

aus Wiesbaden

1. Prüfer: Prof. Dr. Christina Roth

2. Prüfer: Prof. Dr. Wolfgang Ensinger

Tag der Einreichung: 16.12.2014

Tag der mündlichen Prüfung: 06.03.2015

Darmstadt 2015

D17

Diese Arbeit wurde in der Zeit von Oktober 2008 bis März 2013 im BMWi-Projekt „Kanadisch-Deutsche Brennstoffzellenkooperation - Verbesserung der Leistung und Alterungsstabilität von Direktmethanol-Brennstoffzellen der kW-Klasse“ (FKZ 0327853-C) mit den Partnern National Research Council Canada, Forschungszentrum Jülich und Fraunhofer Institut für Solare Energiesysteme Freiburg durchgeführt.

„In bunten Bildern wenig Klarheit,

viel Irrtum und ein Fünkchen Wahrheit“

Johann Wolfgang von Goethe, Faust, Der Tragödie erster Teil

Zusammenfassung

Die Lebensdauer einer Direktmethanol-Brennstoffzelle (DMFC) wird hauptsächlich durch die Degradation der Membran-Elektroden-Einheit (MEA) bestimmt. Dabei spielen sowohl die Abnahme der Protonenleitfähigkeit der Polymermembran, als auch die Alterung der Elektrodenkatalysatoren eine wichtige Rolle. Ein Degradationsmechanismus der eingesetzten Katalysatoren ist die Rutheniumauflösung. Diese Arbeit widmet sich der Analyse der Auflösung, Migration und Abscheidung von Ruthenium in einer DMFC Einzelzelle während der frühen Betriebszeiten zwischen der ersten Inbetriebnahme und etwa 100 h Betriebsstunden.

Um den Auflösungs- und Wanderungsprozess zu verfolgen, ist es notwendig geringe Spuren von Ruthenium innerhalb der MEA zu verfolgen. Hierfür wurden Messungen mittels Röntgenfluoreszenzspektroskopie (XRF), Röntgenabsorptionsspektroskopie (XAS), induktiv gekoppeltes Plasma Massenspektrometrie (ICP-MS) und Cyclovoltammetrie (CV) durchgeführt. Die Charakterisierung der Katalysatoren selbst wurde durch Röntgenpulverbeugung (XRD) und Röntgenphotoelektronenspektroskopie (XPS) vorgenommen. Die Bedingungen der Brennstoffzellentests wurden explizit so gewählt, dass extreme Betriebsbedingungen wie Brennstoffverarmung oder beschleunigte Alterung durch erhöhte Elektrodenpotentiale vermieden wurden. Jeder DMFC Test wurde potentiostatisch kontrolliert bei einem Zellpotential durchgeführt. Nach jedem DFMC Test wurde die Zelle demontiert, die MEA entfernt, getrocknet und die beiden Elektrodenkatalysatoren von der Membran separiert, um einzeln analysiert zu werden. Um die Auswirkung des Herstellungsprozesses auf die Rutheniumauflösung zu untersuchen, kamen zwei verschiedene Herstellungstechniken für die MEAs zum Einsatz: ein nasses Direktsprühverfahren und ein trockenes Decal-Transferverfahren.

Wie die Ergebnisse von XRD Messungen belegen, haben sich die kristallinen Anteile der kommerziellen, rußgeträgerten Platin-Ruthenium Anodenkatalysatoren und Platin Kathodenkatalysatoren unter den gewählten Betriebsbedingungen nicht verändert. Die ermittelten Gitterparameter von 3,916 für den Platin und 3,866 für den Platin-Ruthenium Katalysator sind in guter Übereinstimmung mit den Literarturwerten für diese Materialien. Auch XPS Messungen zeigten keine signifikanten Änderungen der Katalysatorzusammensetzung nach dem DMFC Betrieb.

XAS Messungen hingegen gaben Hinweise darauf, dass ein Übertrag von Ruthenium schon bei der Herstellung der MEA erfolge. Während XAS nur eine qualitative Analyse der Proben ermöglichte, konnte mittels XRF und komplementären ICP-MS Analysen eine quantitative Bestimmung der migrierten Rutheniummengen vorgenommen werden. Obwohl erwartet wurde, dass durch das nasse Sprühverfahren während der Herstellung eine größere Menge Ruthenium auf der Kathodenseite migrieren würde, zeigte sich, dass der Übertrag von Ruthenium beider Herstellungstechniken in der gleichen Größenordnung von etwa 0,02 Gew.% lag. Hervorzuheben ist, dass dieser Transfer von Ruthenium schon während der Herstellung geschah und somit bevor die MEA in eine DMFC eingesetzt wurde. Nach dem Zusammenbau der Zelle und der

Inbetriebnahme der DMFC übertrug ein schneller Auflösungsprozess zusätzliche 0,2 Gew.% Ruthenium auf die Kathodenseite. Hierbei scheint die Herstellungstechnik die Rutheniummigration zu beeinflussen. Die gesprühten MEAs wiesen einen deutlich höheren Rutheniumtransfer von etwa 0,3 Gew.% in den ersten 2 Betriebsstunden auf. Während der nächsten 100 Betriebsstunden der Zelle unter Leerlaufbedingungen wurden weitere 0,3 Gew.% Ruthenium durch einen langsameren Prozess übertragen. Die Prozesse könnten aus zwei unterschiedlichen Rutheniumquellen gespeist werden. Stark lösliche Rutheniumspezies wie z.B. Hydroxide könnten die Quelle für den schnellen Auflösungsprozess darstellen. Der langsamere Prozess könnte hingegen von schwerer aufzulösenden Oxiden gespeist werden.

ICP-MS Analysen verschiedener Lösungsmittel zeigten, dass sowohl Wasser als auch Methanol Ruthenium aus dem Platin-Ruthenium Katalysator auswaschen können. Demgegenüber ist Ameisensäure in der Lage auch Platin zu lösen, neben großen Mengen Ruthenium. Ameisensäure als ein mögliches Nebenprodukt nicht-vollständiger Methanoloxidation könnte somit eine wichtige Rolle bei der Rutheniumauflösung in DMFCs spielen.

Abstract

The lifetime of a direct methanol fuel cell (DMFC) is mostly determined by the degradation of its active component, the membrane electrode assembly (MEA). Besides degradation of the proton conducting membrane, the aging of the electrodes and especially the catalysts therein is the major limiting factor. One of the catalyst degradation mechanisms is ruthenium dissolution. This work is the first extensive study on the dissolution, migration and deposition of ruthenium in a DMFC single cell during early operation, i.e. between first start-up of the cell till approx. 100 h of operation.

To analyze the dissolution process it is necessary to track the trace amounts of ruthenium being dissolved and transported through the MEA. For this task x-ray fluorescence spectroscopy (XRF), x-ray absorption spectroscopy (XAS), inductively coupled plasma mass spectrometry (ICP-MS) and cyclic voltammetry (CV) were used. The characterization of the catalysts itself was carried out by x-ray powder diffraction (XRD) and x-ray photoelectron spectroscopy (XPS). Fuel cell tests were explicitly not including any extreme operation conditions, such as fuel starvation or accelerated aging protocols. Each DMFC test was run at one specific potential for the duration of the test. After operation the cells were disassembled, the MEA removed, dried and cathode and anode catalysts removed from the membrane to be analyzed separately. Two different MEA fabrication techniques, wet spray coating and dry decal transfer, were used to produce MEAs. The fabrication techniques are compared in respect to their influence on ruthenium dissolution.

It is shown, that the crystalline fraction of the commercial platinum-ruthenium on carbon anode catalyst and platinum on carbon cathode catalyst does not change under the operation conditions investigated. The mean lattice parameters of the platinum and platinum-ruthenium catalysts are 3.916 and 3.866, respectively, as determined by XRD measurements. Both values are in good agreement with the lattice parameters reported in literature. Also the XPS measurements do not show any significant change in the catalyst composition after operation in the DMFC.

XAS measurements gave evidence that a transfer of ruthenium already takes place during fabrication of the MEA. While XAS could only be used for qualitative analysis of the samples, XRF and complementary ICP-MS analyses provided quantitative measurements for the migrated ruthenium. Even though it was expected that the wet spray coating technique causes a higher amount of ruthenium to migrate onto the cathode side, the Ru transfer of both techniques in the order of 0.02 wt%. It is important to note, that this transfer happened during fabrication and before the MEA was even assembled inside a DMFC. After cell assembly and start of DMFC operation a fast dissolution process transfers an additional 0.2 wt% ruthenium onto the cathode side. Here the fabrication technique seems to influence the ruthenium crossover. The sprayed MEAs show a significantly higher Ru transfer of about 0.3 wt% during the first 2 h of operation. Over the next 100 h of cell operation of the decal MEAs at open circuit conditions another 0.3 wt% ruthenium are transferred by a presumably slower process. It can be assumed that

there are two sources of ruthenium feeding these two processes. Highly soluble ruthenium species like hydroxides could by the source for the fast dissolution process, while the slower process is fed by harder to dissolve oxides.

ICP-MS analyses of different solvents after leaching experiments using the platinum-ruthenium catalyst show that both water and methanol can dissolve low amounts of ruthenium from the catalyst. In contrast formic acid, which is also present in DMFCs as a product of an incomplete methanol oxidation side reaction, has the capability to dissolve significant amounts of ruthenium and even to attack platinum. Consequently, formation of formic acid inside the DMFC and ruthenium dissolution may be closely correlated.

1. Introduction

The landscape of energy storage and conversion is becoming more diverse. As of now, no single technology is capable of scaling from the smallest mobile devices up to large grid infrastructures. In the foreseeable future there will be a mix of different systems each with their merits and flaws, which make them particularly suited for a given task.

In the field of portable, automotive and off-grid systems lithium ion battery, redox flow battery and fuel cell technologies are currently the most promising candidates. This work is focusing on the latter.

The principles of fuel cells were published by Christian Friedrich Schönbein and William Grove already in 1839. But outside the laboratory the first fuel cells were used only in the late 1950s and early 60s (e.g. NASA Space Program). The fuel cells developed in the mid-1950s at the General Electric laboratories were ion-exchange membrane fuel cells. They belong to the same category of polymer electrolyte fuel cells (PEMFC) as the Nafion® based fuel cells still used today as well as in this work.

PEMFCs can be operated with a variety of different fuels like hydrogen, alcohols and other liquid fuels (e.g. formic acid). Besides hydrogen the direct alcohol fuel cells (DAFC) and in particular the direct methanol fuel cell (DMFC) are the most common forms of low temperature, i.e. below 120 °C, fuel cells used today. Liquid fuels have many advantages in handling and storage compared to gaseous fuels. Also the volumetric energy density of alcohols is comparably large: Methanol has an energy density of 15.6 MJ/l in contrast to 4.5 MJ/l for compressed hydrogen at 690 bar. The downside is, that DMFCs usually have a lower efficiency and power density because of the slower kinetics of methanol oxidation compared to hydrogen oxidation.

Compared with rechargeable batteries, especially lithium based batteries, the market share of fuel cells is very low. This is mainly due to their higher costs, which are driven by the noble metal catalysts, the membrane and the overall lifetime of the DMFC system. Periodically updated reports[1] of the U.S. Department of Energy's (DOE's) Office of Energy Efficiency and Renewable Energy (EERE) [1] list a set of goals addressing these shortcomings. One of these is concerning the long term stability of DMFCs.

In the majority of cases the end of life of a DMFC is not defined by a complete failure of the cell, but by the slow, but constant degradation of performance reaching a level where the power, that can be delivered, is not sufficient for the application anymore. Usually different degradation mechanisms contribute to this aging. This work is focusing on ruthenium dissolution and migration during early operation times (0 – 100 h) of a single cell DMFC.

[1] For the most recent version see http://www1.eere.energy.gov/hydrogenandfuelcells/mypp/

Following this introduction a literature survey on the topic of catalyst degradation and ruthenium dissolution in DMFCs outlines the available scientific data at the beginning of my research. A short overview of the basic principles of direct methanol fuel cells, ruthenium dissolution and the analytical techniques used are given in the theory chapter. In the experimental section of this work the setup and procedures of fuel cell experiments, sample handling and the analyses of the catalysts are described. The fourth chapter presents the results and proposes interpretations of the findings. A short discussion of the results can be found in chapter 5 which lead to a conclusion and outlook in the last chapter.

1.1. Motivation & literature survey

Currently platinum-ruthenium alloys are the favored materials for DMFC anode catalysts. While catalytically active sites of platinum are responsible for the stepwise oxidation of the methanol, ruthenium is needed to provide oxygen species through the splitting of water. These oxygen species free the platinum surface from carbon monoxide intermediates [2]–[5] and complete the methanol oxidation reaction (MOR). Besides this co-catalytic effect of ruthenium there is evidence that there is also an electronic effect of Ru on Pt which influences the MOR [6].

A good review on the DMFC research was published by Ermete Antolini in 2010 [7]. And while Antolini finds many questions answered, he explicitly states that the mechanisms involved in the dissolution of ruthenium still need to be understood.

The unfortunate fact, that ruthenium is dissolved from the anode catalyst is known for a long time. By performing electrochemical stripping experiments on well-defined platinum-ruthenium electrodes Gasteiger et al. [8] have shown, that high anodic potentials above 750 mV vs. NHE will lead to ruthenium dissolution. However, under normal DMFC operation conditions the anode potential remains well below 750 mV vs. NHE as it was demonstrated by reference electrode measurements [9], [10]. In 2004 Zelenay [11] found ruthenium dissolved from the unsupported PtRu black anode catalyst and migrated onto the Pt black cathode catalyst even when no current was drawn from the fuel cell. The evidence was delivered by carbon monoxide (CO) stripping measurements of the cathode catalyst. CO stripping is done by letting carbon monoxide adsorb on the catalyst surface, purge with an inert gas to remove any excess CO and measuring the oxidation current when a positive potential sweep is applied to the catalyst. Comparison of the data obtained from pure platinum catalysts and catalysts containing increasing amounts of ruthenium can then be used as a fingerprint to identify pure Pt catalysts and catalysts contaminated with Ru. The advantage of CO stripping is its high sensitivity for the catalyst composition, but as many other fingerprinting methods this can give only qualitative information.

Today carbon supported nanoparticle PtRu catalysts are the most common choice for fuel cell electrodes. They are commercially available, show good performance and a relatively low degradation during operation, thus enabling DMFC stack lifetimes of more than 10.000 hours [12], [13]. But ruthenium dissolution is also found when using supported catalysts [14]–[16]. Again CO stripping was used to verify the redeposition of migrated Ru onto the cathode catalysts.

There are a number of publications reporting ruthenium dissolution and migration in fuel cell stacks [14], [17]–[20]. Because the conditions in a stack are more corrosive, due to extreme operation conditions, such as fuel depletion, flooding, water starvation etc., the amount of migrated ruthenium on the cathode catalysts is larger than in single cells. This makes it possible to detect the Ru with element sensitive techniques like energy dispersive X-ray analysis (EDX), which needs several atom% elemental concentration to give reliable data. The advantage of higher Ru amounts being dissolved comes at the cost of loss of control over the actual operation conditions. In a fuel cell stack the individual cells are all electrically, thermally and via their fuel feeds connected to each other. This makes it very difficult if not impossible to determine which specific condition led to what degree of Ru dissolution in each of the cells.

In single cell setups under normal operation conditions, i.e. no fuel depletion etc., the amount of transferred Ru is very low. Therefore many publications (see Table 1) need to rely on indirect proof of Ru on the cathode catalyst by electrochemical measurements, usually CO stripping. While there is little reason to question that ruthenium is causing the effects found, CO stripping is not an element sensitive analysis and there may be some other explanation for the changes observed. Furthermore CO stripping is not a quantitative technique and cannot provide information on the amount of Ru transferred from anode to cathode side. Park et al. [21] chose a different approach and analyzed the cathode of their MEA samples by time-of-flight mass spectrometry (TOF-SIMS). TOF-SIMS is a very sensitive method and capable of discriminating between elements. But also TOF-SIMS is not quantitative and the EDX analysis they performed only showed a ruthenium content of less than 0.3 atom%, likely the lower detection limit of the EDX.

A report by Cheng et al [22] linked the findings of their electrochemical analysis with a quantitative measurement of the ruthenium concentration using neutron activation analysis (NAA). But they subjected the catalyst samples only to accelerated aging via potential cycling, not a real fuel cell test. Even though this was done inside a single cell DMFC setup it is still a model and does not reflect the real conditions of DMFC operation. As Wasmus [3] put it "*[…] catalysis under fuel cell conditions is different from that observed by fundamental studies […]*". This holds true for effects like catalyst aging and degradation as well.

Table 1: Exemplary selection of references on ruthenium dissolution in DMFCs and model systems.

reference	type of system?	ruthenium dissolution found?	analysis method
Gasteiger 1994 [8]	model system	yes	CO stripping
Zelenay 2004 [11]	DMFC single cell	yes	CO stripping
Woo 2006 [23]	DMFC single cell	yes	EDX
Valdez 2006 [14]	DMFC stack	no	EDX
Wang 2008 [16]	DMFC single cell	yes	CO stripping
Park 2008 [21]	DMFC single cell	yes	TOF-SIMS
Liu 2009 [24]	model system	yes	ICP-MS
Cheng 2010 [22]	DMFC single cell	yes	CO stripping, NAA
Arlt 2011 [18]	DMFC stack	yes	XAS tomography
Park 2011 [25]	DMFC stack	yes	EDX, ICP-AES
Corpuz 2012 [26]	DMFC single cell	yes	CO stripping, EDX
Gerteisen 2012 [19]	DMFC stack	yes	MeOH stripping, EDX
Arlt 2013 [27]	DMFC single cell	yes	XAS imaging

The source of the dissolved ruthenium is also still under discussion. Zelenay et al. [11] proposed the diffusion of ca. 1 nm sized RuO_2 particles surrounded by structural water through the pores of the Nafion® membrane. In agreement, Corpuz et al. [26] observed that catalysts containing a larger amount of ruthenium oxides, especially hydrous oxides, seem to be more prone to dissolution. This they correlated to the higher amounts of transferred Ru found on the cathode catalysts. Park et al. [21] concluded from HR-TEM analysis that the Pt-Ru particles of their unsupported catalysts decomposed into small fragments, which could be easily oxidized. Wang et al. [28] observed that the content of metallic ruthenium decreases while the fraction of ruthenium oxides increases with time of operation. They interpreted these findings in terms of metallic Ru which is more easily dissolved from the catalyst, while the oxide is more stable. Moreover, the composition of the platinum-ruthenium catalyst is complex and changes during operation of the DMFC depending e.g. on the potential [29]–[31]. Hence, the catalyst composition and morphology are likely to influence the mechanism and extent of ruthenium dissolution. Furthermore, Arlt et al. [27] showed that the dissolution of ruthenium (and

platinum) is dependent on the local geometry of the fuel cell. The catalyst dissolution observed was more pronounced under the ribs of the flow field than under the channels.

To come closer to a full understanding of the processes involved in ruthenium dissolution in DMFCs a detailed, quantitative analysis of the amounts of ruthenium being dissolved under specific conditions seems necessary. This work aims at providing quantitative data of ruthenium dissolution during early operation from minutes to hours in a single cell DMFC. Two different MEA preparation techniques were used to produce MEAs, which were subjected to defined DMFC conditions and thereafter analyzed in respect to 1) catalyst structure by x-ray diffraction (XRD) and x-ray photoemission spectroscopy (XPS), 2) ruthenium dissolution and migration by synchrotron x-ray fluorescence spectroscopy (XRF) and inductively coupled plasma mass spectrometry (ICP-MS) and 3) catalytic changes due to ruthenium crossover by cyclic voltammetry (CV).

2. Theory

It is not in the scope of this work to review the theory behind all the experimental techniques and analytical methods used. Therefore this chapter will provide only the necessary background on DMFCs themselves, ruthenium dissolution in DMFCs and x-ray fluorescence spectroscopy (XRF). XRF was the single most important analytical technique for the quantitative measurement of ruthenium transferred onto the DMFC cathode catalysts. Therefore a more detailed insight into the technique and the data evaluation is given in this chapter.

2.1. Direct methanol fuel cells

Direct methanol fuel cells are typically realized as polymer electrolyte membrane fuel cells (PEMFC). A polymer membrane separates the two galvanic half-cells and the two chemical reactions therein; the methanol oxidation reaction (MOR) at the anode and the oxygen reduction reaction (ORR) at the cathode side (Figure 1).

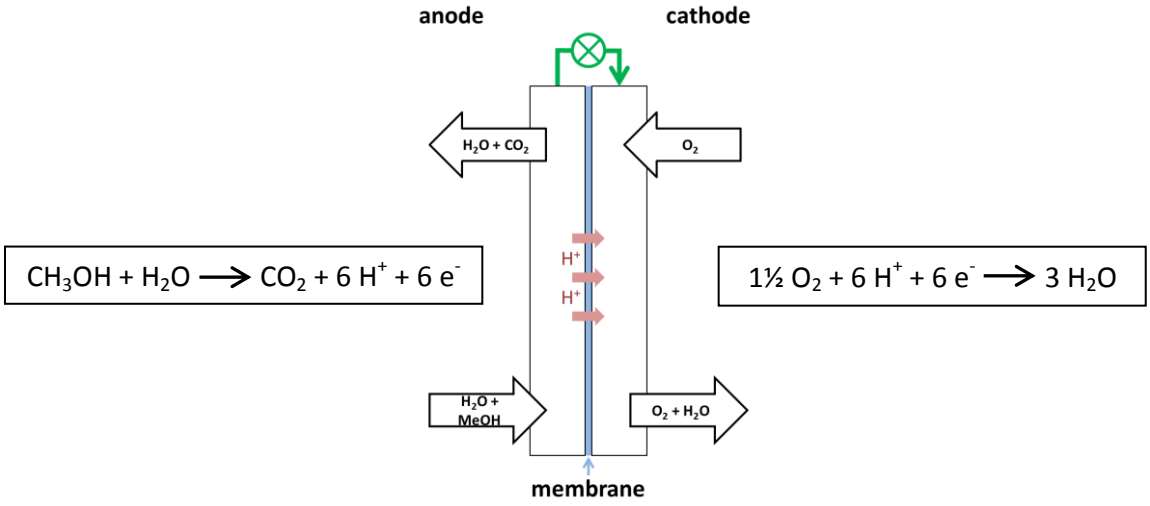

Figure 1: Working principle of a direct methanol fuel cell.

Both electrodes contain catalysts optimized for the respective reaction, a carbon supported platinum-ruthenium (Pt-Ru/C) nanoparticle catalyst for the MOR and a carbon supported platinum (Pt/C) nanoparticle catalyst for the ORR. Furthermore the electrodes contain Teflon® to adjust the hydrophobicity and a proton-conducting ionomer to facilitate the proton transport towards the membrane. The membrane itself consists of a proton-conducting polymer as well. The most commonly used ionomer is Nafion® made by DuPont, a fluorinated polycarbon similar to Teflon® with sulfonic acid end groups [32], [33]. Other polymers, e.g. sulfonated poly-ether-ether-ketone (sPEEK), are being discussed as alternatives. A Nafion® based membrane electrode

assembly (MEA) is shown in Figure 2. The size of the membrane shown is 7 x 7 cm², while the electrode area is 5 x 5 cm². Information on the manufacturing process of MEAs used in this work can be found in chapter 3.1.

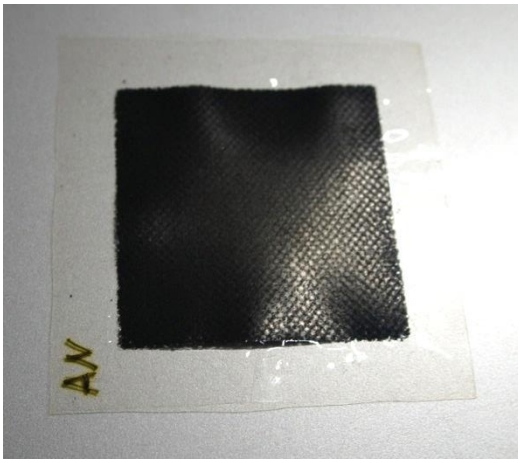

Figure 2: MEA produced by decal transfer of the electrodes onto a Nafion® membrane. Electrode size is 5 x 5 cm. The netlike structure originates from the screen printing of the electrode onto the transfer medium.

Figure 3 provides a schematic view of the structure of the electrode itself. Carbon particles and agglomerates are decorated with nanometer sized catalyst particles. Inside the porous structure formed by the carbon support ionomer fibers provide the conducting pathways for protons.

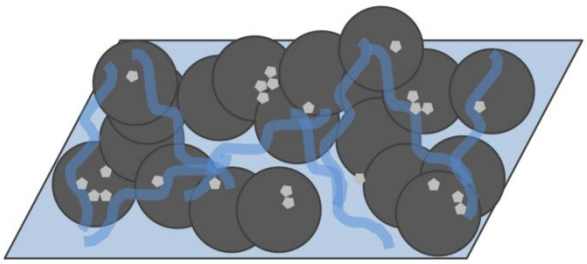

Figure 3: Schematic drawing of the DMFC electrode structure: platinum nanoparticle (light grey) decorated carbon (dark grey) dispersed on a Nafion® membrane (light blue) with ionomer fibers (blue).

Transmission electron microscope (TEM) micrographs in Figure 4 show the structure of a typical carbon supported platinum-ruthenium catalyst. The metal nanoparticles have a size of approximately 2 nm while the carbon support is composed of particles in the range of tens to hundreds of nanometers. The carbon particles themselves form agglomerates up to micrometers in size.

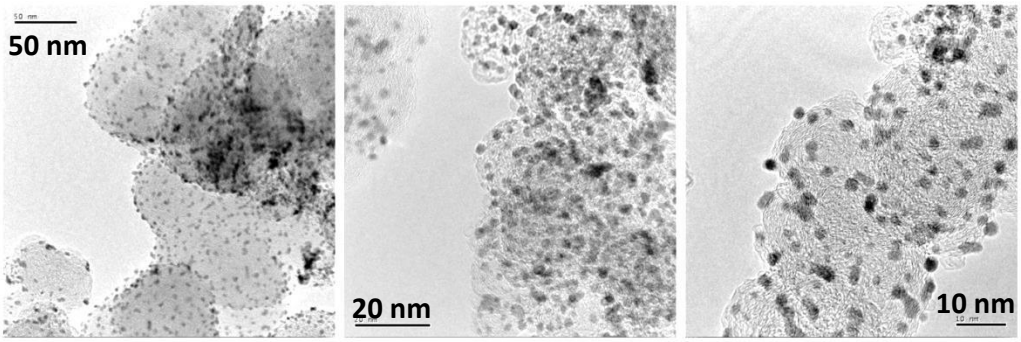

Figure 4: TEM micrographs of the HiSpec 12100 anode PtRu catalyst at different magnifications.

This anode catalyst and its respective cathode counterpart catalyze the reactions of the DMFC. As has been mentioned before, the net reaction of methanol oxidation:

$$CH_3OH + 1½\ O_2 + H_2O \rightarrow 3\ H_2O + CO_2$$

is separated into two half-cell reactions, the methanol oxidation reaction (MOR) taking place at the anode and the oxygen reduction reaction (ORR) at the cathode of the DMFC. Both reaction compartments are separated by a proton conducting membrane. Markovic et al. [34] propose two possible pathways for the mechanism of oxygen reduction at the cathode.

A direct 4 electron mechanism:

$$Pt + O_2 \rightarrow Pt - (O_2)_{ads}$$

$$Pt - (O_2)_{ads} + 4\ H^+ + 4\ e^- \rightarrow Pt + 2\ H_2O$$

And a series mechanism, where hydrogen peroxide as intermediate is formed:

$$Pt + O_2 \rightarrow Pt - (O_2)_{ads}$$

$$Pt - (O_2)_{ads} + 2\ H^+ + 2\ e^- \rightarrow Pt - (H_2O_2)_{ads}$$

$$Pt - (H_2O_2)_{ads} \rightarrow Pt - (O)_{ads} + H_2O$$

$$Pt - (O)_{ads} + 2\ H^+ + 2\ e^- \rightarrow Pt - (H_2O)_{ads}$$

$$Pt - (H_2O)_{ads} \rightarrow Pt + H_2O$$

The work of Markovic postulates that the O-O bond of the oxygen molecule is not broken and the pathway via the hydrogen peroxide intermediate is the dominant reaction pathway. The formation of hydrogen peroxide is especially important in the discussion of ionomer degradation and aging [35].

Lamy et al. [36]–[38] and Iwasita et al. [39] describe the MOR at the anode as a stepwise deprotonation of methanol:

$$Pt + CH_3OH \rightarrow Pt - (CH_3OH)_{ads}$$

$$Pt - (CH_3OH)_{ads} \rightarrow Pt - (CH_2OH)_{ads} + H^+ + e^-$$

$$Pt - (CH_2OH)_{ads} \rightarrow Pt - (CHOH)_{ads} + H^+ + e^-$$

$$Pt - (CHOH)_{ads} \rightarrow Pt - (COH)_{ads} + H^+ + e^-$$

$$Pt - (COH)_{ads} \rightarrow Pt - (CO)_{ads} + H^+ + e^-$$

Carbon monoxide binds strongly to the platinum surface under the conditions found in a DMFC, thus blocking the active sites of the Pt and poisoning the catalyst. If ruthenium is added to form an alloyed catalyst the splitting of water at the Ru can produce hydroxide species:

$$Ru + H_2O \rightarrow Ru - (H_2O)_{ads}$$

$$Ru - (H_2O)_{ads} \rightarrow Ru - (OH)_{ads} + H^+ + e^-$$

These oxygen species can react with the CO on the platinum surface, complete the oxidation of methanol and free the platinum active sites for further reactions:

$$Pt - (CO)_{ads} + Ru - (OH)_{ads} \rightarrow Pt + Ru + CO_2 + H^+ + e^-$$

This bifunctional mechanism of water splitting by ruthenium was first proposed by Watanabe et al. [2] and has been subject of different theoretical [40] and experimental [4], [5], [41] works. Besides the bifunctional mechanism also a ligand effect of Ru on Pt is discussed [6], [42], where the electronic structure of platinum is altered by alloying with ruthenium and in consequence the bonding strength of CO is weakened. Gasteiger et al. [8] have shown that a bulk 1:1 atomic ratio of Pt and Ru is the optimal composition for methanol oxidation. The surface ratio of Pt and Ru of the nanoparticles differs. Nitani et al. [43] found that a ruthenium rich surface composition of the catalyst is correlated with enhanced activity towards MOR.

While there are questions raised whether an alloyed PtRu catalyst or a platinum catalyst with ruthenium hydroxide species in close proximity is actually more active for the MOR [44], Luxton et al. [45] have shown, that Ru oxides seem to be more prone to dissolution. Especially for commercial catalysts long term stability is of importance. Therefore, most DMFC PtRu catalysts commercially available and widely used rely on 1:1 PtRu alloyed nanoparticles.

The oxidation of methanol to CO_2 is not always complete. Intermediates, such as formaldehyde, can also be products of an incomplete oxidation. Side reactions can lead to other products like formic acid. The production and rate of production of these products depend on the structure of the catalyst itself [5] as well as on the operation conditions of the DMFC [46], [47]. Formic acid might play a significant role in ruthenium dissolution as will be shown in this work (see chapter 4.6).

Other parasitic effects of real DMFC operation include the crossover of methanol [46], [48] and oxygen [49] through the membrane to the cathode and anode, respectively. Crossover of methanol will lead to a mixed potential at the cathode, which lowers the performance of the fuel cell and fuel efficiency. Oxygen crossover to the anode side lowers the fuel efficiency as well and might play a role in chemical changes of the catalyst. The presence of oxygen at the anode side could be involved in the side reaction leading to formic acid production.

Usually the performance of a fuel cell or FC stack is characterized by current-voltage curves (I-V curves) [50], [51]. Plotting the cell voltage versus the current density will lead to an I-V curve as shown in Figure 5. The current density is the cell current normalized to the area of the MEA. This ensures better comparability of cells or stacks of different sizes.

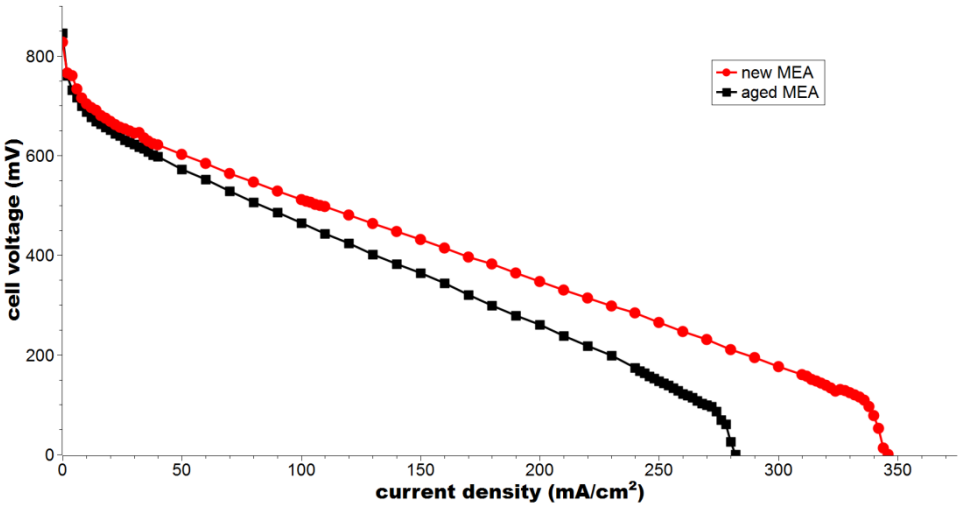

Figure 5: I-V curves of a DMFC at begin of operation (red) and after several hours of operation under varying load profiles (black).

The curve can be divided in three distinct regions: 1) the activation region at low current densities with a sharp drop in voltage, 2) the ohmic region exhibiting a linear dependency of voltage and current density and 3) the mass transport region at high current densities again with a sharp drop in voltage. It is important to notice, that the responsible processes, i.e. activation over-potential, ohmic losses and mass transport limitation, are present in the complete current range of DMFC operation. It is only their dominance in certain current density ranges, which gives these regions there specific names and profiles. Because of this superposition of different effects I-V curves have only limited informative value when analyzing specific processes inside fuel cells. The black curve in Figure 5 was recorded after the DMFC was operated for several hours under varying load profiles. It is obvious that the cell performed worse than at start-up. The exact changes inside the cell, which led to this performance loss, cannot be deduced from the I-V curve, though.

This work focusses strictly on ruthenium dissolution as one of the degradation mechanisms in DMFCs. Therefore, no further I-V curves are shown. To put the experiments in context with other published results a schematic I-V curve including the sample histories is given in Figure 17.

2.2. Ruthenium dissolution

The topic of ruthenium dissolution in DMFCs usually encompasses more than just the dissolution process itself. The migration of Ru through electrode and membrane and its deposition on the cathode or other components of the fuel cell are an integral part as well. This is because the dissolution of Ru inside a working fuel cell is intrinsically connected with the migration of the dissolved species due to diffusion, electro-migration and liquid flow and consequently the deposition of ruthenium along that way. A schematic representation of these linked processes is shown in Figure 6. All of these topics and interdependencies are usually subsumed under *ruthenium dissolution*.

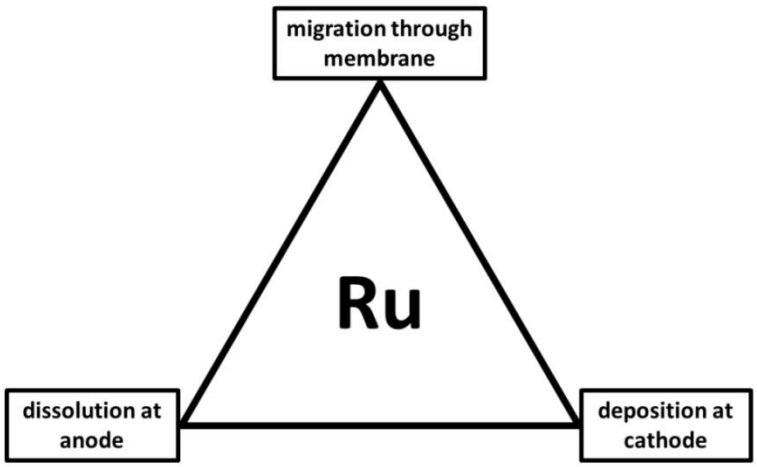

Figure 6: The problem of ruthenium dissolution is always connected with Ru migration and deposition as well.

Pure ruthenium is a noble metal and shows good stability against dissolution over a broad range of potential and pH [52], [53]. However, the corrosive environment in a DMFC has a severe influence on the stability of the supported platinum-ruthenium nanoparticle catalysts. A more detailed view of the platinum-ruthenium catalyst structure is necessary to understand the dissolution of ruthenium. Carbon supported platinum-ruthenium alloy nanoparticle catalysts have a complex composition of several different alloyed and non-alloyed phases [29], [43], [54]–[59]. Besides the carbon support and the Pt-Ru alloy crystallites also oxides of both platinum and ruthenium as well as hydrous ruthenium oxides [60] can be found. It is important to note, that the oxides and hydroxides are usually amorphous. Therefore their presence cannot be detected by means of x-ray diffraction (XRD), and other techniques like x-ray photoelectron spectroscopy (XPS) or x-ray absorption spectroscopy (XAS) have to be applied. Cyclic voltammetry (CV) can be used to indirectly determine even small changes in the catalyst composition and x-ray fluorescence spectroscopy (XRF) can be used to quantify the composition of a sample. A schematic overview of some possible anode catalyst components and applicable analytical techniques for their identification and characterization is shown in Figure 7.

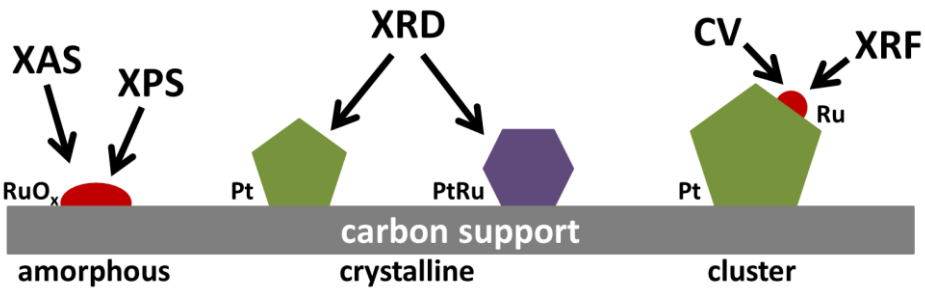

Figure 7: Overview of analysis methods and the specific chemical / structural characteristics they address.

The presence of several ruthenium containing species implies that dissolution can be fed by different ruthenium sources. Luxton et al. studied the dissolution properties of hydrous and anhydrous Ru oxides [45]. They found, that both acidic and basic conditions lead to the dissolution of ruthenium. The chemical environment inside a fuel cell catalyst is typically of acidic nature, mainly because of the sulfonic acid groups of the ionomer and chlorine impurities in the fuel [61], [62]. Chlorine impurities are an important issue for DMFC stacks with closed water cycles. These DMFC stacks often encounter significant ruthenium dissolution during their lifetime. In Figure 8 a scanning electron microscope (SEM) micrograph of a MEA cross section with an overlaid elemental mapping for ruthenium is shown. This MEA was operated inside a 60 cell DMFC stack for 3.000 hours.

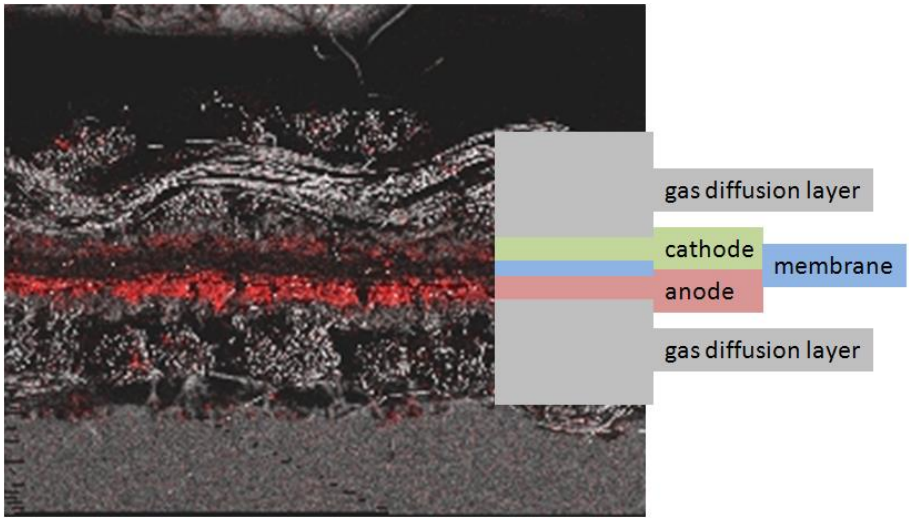

Figure 8: SEM micrograph of a MEA cross section with overlaid elemental mapping of ruthenium in red. The MEA was operated as part of a DMFC stack for 3.000 hours prior to disassembly.

As expected the highest concentration of Ru is found in the anode catalyst layer composed of supported platinum-ruthenium nanoparticles. But also at the formerly pure platinum cathode catalyst ruthenium can be found. Energy dispersive x-ray analysis allows only a qualitative measurement, but the detection limit of the instrument used is about 1-2 atom%. The clear Ru signal originating from the cathode can thus be estimated to indicate at least several atom% of Ru. Besides Ru on the cathode catalyst Mukerjee et al. found ruthenium also inside the Nafion® membrane [63].

Instead of performing analyses of deposited ruthenium Liu et al. [24] concentrated on measuring the dissolved Ru. They mounted two Nafion® membranes, each coated with an electrode on one side, one with a Pt/C catalyst and the other with a Pt-Ru/C catalyst, in an electrochemical cell setup. Effectively they split the membrane of a single cell DMFC and inserted a compartment filled with an electrolyte. From this electrolyte samples at different operation times of the DMFC-like setup were fed to an inductively coupled plasma mass spectrometer. The setup was operated for 696 h during which 13 ICP-MS measurements of the electrolyte were taken. They found 11.5 µg platinum and 857.3 µg ruthenium dissolved in the electrolyte after 696 h operation. These amounts are orders of magnitudes higher than the ones found in this work. Taking into account the findings of Luxton [45], the sulfuric acid electrolyte might be the reason for the pronounced Ru dissolution in their model system. In addition their accelerated aging protocol included a period of high anodic potential, which increased the amount of dissolved ruthenium even more. Different experiments on model systems [64], [65] have shown that high anodic potentials lead to the formation of ruthenium oxides. These oxides are again more susceptible to dissolution then Ru in its metallic state.

Changes of the PtRu catalyst are not limited to the formation of oxides but also can take place in the form of reordering of the atomic structure of the particles [29]. During this rearrangement the catalyst might also be more vulnerable to dissolution.

Ruthenium dissolution, migration and deposition have an overall negative effect on cell performance. The loss of Ru at the anode obviously results in a drop of its co-catalytic function for the bifunctional mechanism. This in turn leads to more catalytic sites of platinum being blocked by CO adsorbates and slower rates of methanol oxidation.The deposition of ruthenium in the membrane lowers the water uptake of Nafion® and increases the ionic resistance of the proton conductor [63]. And the deposition of Ru onto the platinum cathode catalyst lowers the catalyst's performance for the oxygen reduction reaction [66]. These combined negative effects make it so important to fully understand the processes involved and find ways to prevent the performance degradation.

2.3. X-ray fluorescence spectroscopy

X-ray fluorescence spectroscopy is the single most important technique in this thesis. It allows to quantify trace amounts of ruthenium in catalyst samples without the need for any chemical preprocessing of the materials (in contrast to e.g. inductively coupled plasma mass spectrometry).

XRF utilizes the photoelectric effect and the accompanied fluorescence for quantitative measurement and identification of elements in a sample. A schematic representation of the underlying processes is depicted in Figure 9.

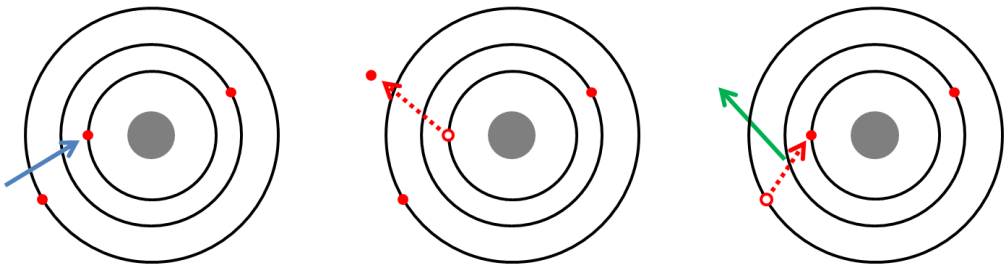

Figure 9: Principle of x-ray fluorescence.
(on the left) an x-ray photon (blue arrow) interacts with an inner shell electron, (in the middle) the electron is ejected as an photoelectron, (on the right) an electron from a higher energy outer shell fills the vacancy and the energy difference is converted to a fluorescence x-ray photon (green arrow).

An x-ray photon of sufficient energy can ionize electrons from inner shells. Usually K, L, M shells are targeted with XRF. The generated core hole is consecutively filled by an electron from an outer shell and the energy difference of the electronic states (outer shell – inner shell) is converted to a fluorescence photon. The binding energies of the electrons are element specific; therefore the energy difference carried by the fluorescence photon is as well. Using an energy discriminating detector the fluorescence spectrum can be analyzed with regard to the elements present in the sample.

As the yield of fluorescence photons coming from a specific element depends on the ionization cross-section of the electron, the amount of that element, the attenuation of the fluorescence photons while leaving the sample volume and the number of incident X-ray photons, it is possible to calculate the elemental concentration if all other factors are known. Another possibility is to use standards of the elements of interest and determine the fluorescence yield empirically. The latter method was used in this work. A detailed description of the Ru standard sample preparation can be found in 3.4.1.

The sensitivity of synchrotron XRF measurements is very high [67]–[69]. For most elements the detection limit is in the parts per billion range. To achieve the best possible detection limits a careful analysis of the data is mandatory [70]. Also precise quantification of elemental amounts requires the consideration of different effects that influence the fluorescence photon yield. Higher absorption edge energies and therefore fluorescence photon energies result in a better sensitivity as it is more likely that the fluorescence photons can leave the sample volume and reach the detector without being scattered or absorbed [71], [72]. But depending on the sample composition high fluorescence photon energies also increase the chance of a fluorescence photon interacting with another electron and producing a new photon of different energy. As an example in the PtRu catalysts studied there is a not negligible probability that a Ru K line fluorescence photon will in turn be absorbed by a platinum atom and lead to a Pt M line photon leaving the sample. This will shift the intensities of the observed fluorescence lines in the spectra and has to be accounted for when analyzing and fitting the data [73]. Another effect to be accounted for is the interference of spectral lines. If a sample is composed of several elements one or more fluorescence lines can overlap [74]. Besides these effects, which are linked to the sample composition and the physical processes therein, also the acquisition of data by the detector system can distort the spectra.

The energy discriminating detector used in this work was a silicon drift detector (SSD). The basic working principle of SSDs is similar to that of a photodiode with the difference that the depletion layer is enlarged by an external field [75]. An incident x-ray photon creates an electron-hole pair, which is separated in the space-charge region of the pn-junction and electron and hole drift towards the anode and cathode, respectively. This creates a measurable current, which is proportional to the energy of the x-ray photon. A high energy x-ray photon can create more electron-hole pairs and thus a higher current (see Figure 10).

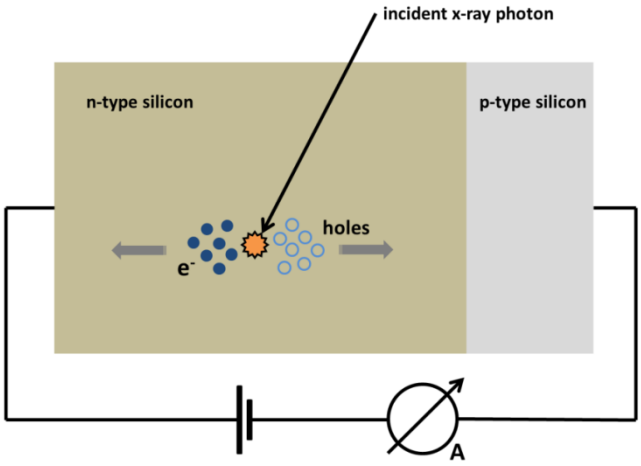

Figure 10: Working principle of an x-ray detector using a semiconductor diode.

As long as the amplifiers and other electronics are fast enough and the dead time is shorter than the events generated by multiple incoming photons, each photon and its energy can be determined. But if the flux of x-ray photons is too high, certain artifacts can appear. With a certain probability two photons with energies v_1 and v_2 can arrive within the period of time where these events cannot be separated by the detector / electronic system. In this case the detector system generates a signal, as if a photon with energy of $v_1 + v_2$ was detected. This leads to a so-called sum peak. Also a very high flux of photons of a single energy v_1 can produce a sum peak of the apparent energy of $(2 \cdot v_1)$. This special form of sum peaks is called pile-up peak. In Figure 11 a schematic XRF spectrum is depicted. The counts of the incident photons with energies v_1 and v_2 are shown in blue, while the aforementioned sum peak and pile-up artifacts are depicted in green and orange, respectively.

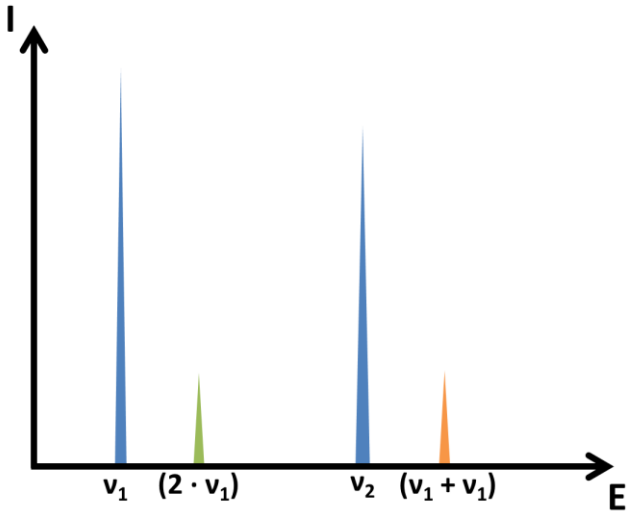

Figure 11: Schematic XRF spectrum showing the counts of the two incident x-ray photon energies v_1 and v_2 in blue, a sum peak (green) and a pile-up (orange) artefact.

The XRF analysis software accounts for both of these artifacts, but as these are stochastic processes there is no way to completely remove sum and pile-up peaks from a spectrum [76]. This is of importance, especially in this work, as the platinum M lines produce pile-up peaks around the energy where the ruthenium K-α line is expected. As described in the experimental section (see 3.5.1) a set of filters was used to reduce the platinum fluorescence signal and thereby avoiding / reducing the pile-up peak intensity. Still there are contributions of the platinum pile-up signal to the peak fitting of the ruthenium K-α line, which makes the error on quantifying the Ru amount larger especially for low Ru concentrations. The following XRF spectrum (see Figure 12) provides an example of two XRF measurements. One sample contains only ruthenium, while the other sample contains a high amount of platinum as well. The platinum M line pile-up peak overlaps with the ruthenium K line peak. This makes a deconvolution of the peaks necessary.

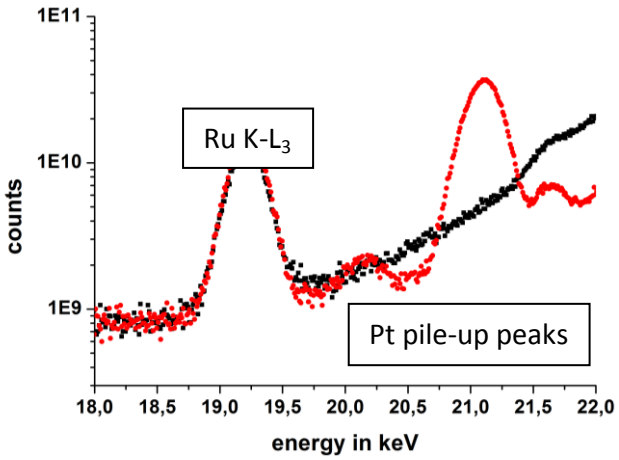

Figure 12: XRF spectra of a pure ruthenium reference sample (black) and a sample containing the same amount of Ru plus 15 wt% platinum (red).

Taking all these sometimes contradictory effects into account, choosing the right experimental parameters is difficult. To quantify trace amounts of ruthenium a high photon flux from the x-ray source is needed to generate as much fluorescence photons as possible. This was the main reason to conduct the XRF experiments at a synchrotron x-ray source. On the other hand the fluorescence from platinum can oversaturate the detector, because the samples contained around 15 wt% platinum. So the photon flux was adjusted till the detector could be operated in its optimal flux range. Still the platinum fluorescence was intense enough to produce pile-up artefacts. The artifacts interfered with the ruthenium signal to be measured as has been shown above. To reduce the pile-up peaks a set of filters was introduced between the sample and the detector. The filter setup reduced the pile-up artifacts, but simultaneously reduced the Ru signal as well. So the reduction of pile-up artifacts came at the expense of a worse lower detection limit for ruthenium. The high amounts of platinum also led to a higher absorption of ruthenium

fluorescence photons inside the sample volume and therefore lower numbers of photons reaching the detector.

The tradeoffs, that had to be made, led to a minimum detection limit for Ru in the range of about 0.012 wt% for the cathode catalyst samples analyzed. This is about two orders of magnitude more than the sub-ppm detection limits for metals which have been demonstrated in other works [67]–[69], where the sample properties were more favorable. The exact experimental parameters for the XRF experiments are listed in chapter 3.5.1.

3. Experimental

Studying the ruthenium dissolution and migration in 25 cm² single cell DMFCs requires careful trace analysis of ppm levels of Ru in the cathode materials. The anode catalysts on the other hand contain as much as 25 wt% of ruthenium. This demands extremely clean experimental procedures and handling to avoid any cross contamination.

A strict modus operandi was established to minimize the risk of contamination. There were separate tools (e.g. spatulas, mortars, scalpels, pressing matrices etc.) for handling cathode and anode material. Also all fuel cell components in contact with the MEA (flow fields, fittings) were only used on the cathode or anode side, respectively. Gas diffusion layers (GDL) were only used once and discarded immediately after cell disassembly. All tools, work surfaces and cell components were cleaned thoroughly using acetone and water after each single use.

All experiments in this work were conducted using the same catalysts from the same batches of Johnson Matthey HiSpec 12100 and HiSpec 13100. The characteristics of these catalysts are listed in Table 2 as stated by the manufacturer[2].

Table 2: Johnson Matthey HiSpec DMFC catalysts characteristics.

HiSpec Catalyst Type	**12100**	**13100**
Product Reference Number	S128526	S128538
Platinum, wt% (dry basis)	46.0 – 50.0	70.0 – 73.5
Ruthenium, wt% (dry basis)	23.5 – 25.0	
Platinum atomic% (from total metal)	48.0 – 52.0	
Ruthenium atomic% (from total metal)	48.0 – 52.0	
Maximum XRD Crystallite Size in nanometers	3.0	4.6
Maximum Lattice Parameter in nanometers	0.387	0.393

[2] Compiled from "4_hispec_catalyst_product_range.pdf" (version as of 07/01/2013) downloaded from: http://www.jmfuelcells.com/documents/fuel_cells/documents_library/4_hispec_catalyst_product_range

3.1. Preparation of membrane-electrode-assemblies (MEA)

Work by Zelenay et al. [11] suggests that ruthenium dissolution only takes place when the MEA is humidified. In good agreement, x-ray absorption spectroscopy measurements (see chapter 4.1.2) showed a ruthenium transfer from anode to cathode already during preparation by wet spraying (see below). To verify this, two different preparation methods were chosen to produce MEAs: a direct wet spray-coating of the Nafion® membrane and a dry decal transfer method.

Preparation of spray-coated MEAs was conducted at the Technische Universität Darmstadt (TU Darmstadt), while MEAs produced by the decal transfer method were provided by the Forschungszentrum Jülich (FZ Jülich).

3.1.1. Airbrush® spraying

Direct spray-coating of the membrane is one of the easiest methods to fabricate MEAs. The advantages are low cost of the necessary equipment, ease of the method itself and its suitability for small cell area and low quantity MEA production. The main disadvantage is that it is comparably time consuming. Still this technique is very well suited for research environments.

The equipment consists of a heated fixture, which uses vacuum to fix the membrane while spraying. The heating is needed to evaporate the solvents fast enough, so that no droplets may form on the membrane, which would lead to an uneven distribution of the catalyst. A picture of the spraying bench is shown in Figure 13.

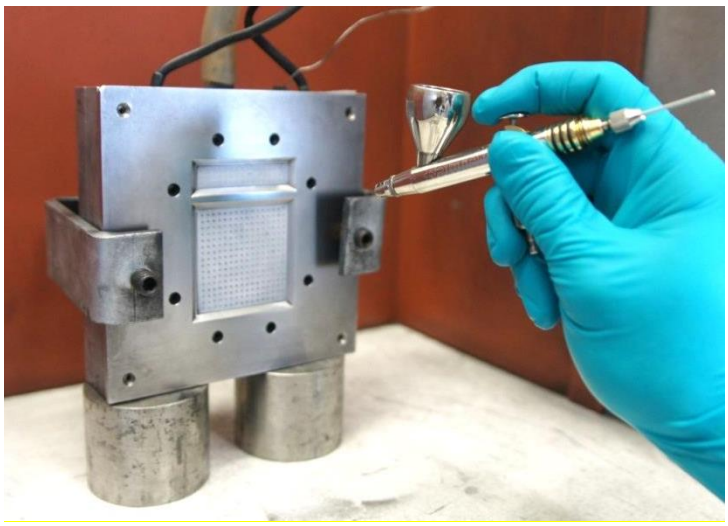

Figure 13: Photograph of MEA spraying fixture and Airbrush® pistol.

For spraying a commercial Airbrush® pistol was used. The pistol is fed with pure nitrogen to minimize the possibility of igniting the highly reactive catalyst.

To prepare an ink with the required high viscosity the following recipes were used:

Table 3: Ink recipes for wet Airbrush® spraying.

Anode	**Cathode**
220 mg HiSpec 12100	185 mg HiSpec 13100
9 ml water	9 ml water
10 ml isopropanol	10 ml isopropanol
1 ml 15% Nafion® solution (DuPont™ DE 521)	1 ml 15% Nafion® solution (DuPont™ DE 521)

First catalyst powder and water were mixed, then isopropanol and Nafion® solution were added. The ink was homogenized using an ultrasonic disperser. For spraying a Nafion® 117 membrane (thickness ca. 180 µm) was placed on a heated vacuum fixture. Using an Airbrush® pistol the ink was evenly spread over an area of 5 cm x 5 cm for the actual MEA and a 1 cm x 5 cm test area (see Figure 14). The purpose of the test area is to produce an as-prepared sample of each sprayed MEA under the same conditions.

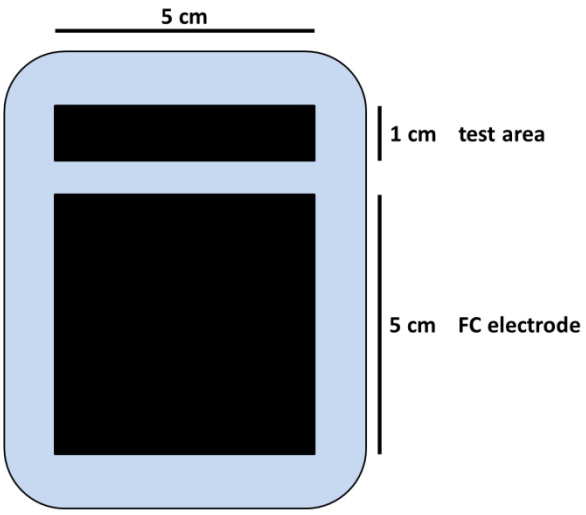

Figure 14: Schematic of MEA spraying mask.

3.1.2. Decal transfer method

As mentioned earlier, the FZ Jülich provided the MEAs produced by the decal transfer method. The electrode is first screen printed onto a Teflon® transfer medium, dried and consecutively hot pressed onto the Nafion® 117 membrane. The ink to be processed by screen printing needs a lower viscosity than that for spraying, so the recipes differ:

Table 4: Ink recipes for MEA fabrication by decal transfer.

Anode	**Cathode**
500 mg HiSpec 12100	750 mg HiSpec 13100
500 µl water	750 µl water
2700 µl 1-hexanol	3900 µl 1-hexanol
1160 µl 15% Nafion® solution (DE 521)	2150 µl 15% Nafion® solution (DE 521)
	75 µl 20% PTFE dispersion

Again the catalyst powder was first mixed with water to ensure that the highly active catalysts do not ignite the hexanol or the aliphatic alcohols in the Nafion® solution. After screen printing the ink onto a Teflon® transfer medium, it was hot pressed (2 min, 130 °C, 0.5 kN/cm²) onto a Nafion® 117 membrane. Freudenberg H2315 I3 carbon paper without micro porous layer was used as gas diffusion layer with all MEAs.

3.2. Fuel cell setup and operation conditions

The fuel cell used was a Quintech EFC-25-01 single test cell with graphite grid type [77] flow fields (see Figure 15). The electrode area was 5 x 5 cm². Temperature regulation of the cell was provided by two heating pads attached to the gold plated bipolar plates. Individual silicone gaskets for anode and cathode were used, which were cleaned together with all other fuel cell components after each use (see 3.4). The GDLs were only used once and immediately discarded after cell disassembly.

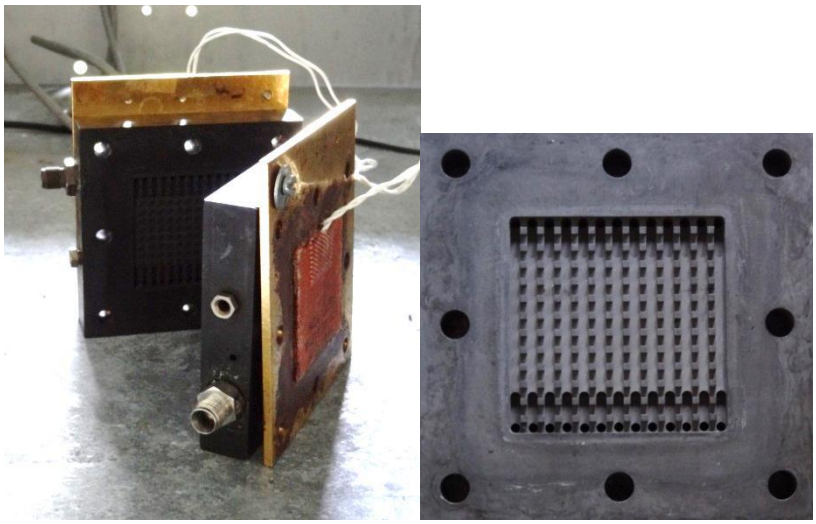

Figure 15: Gold plated bipolar plates with heating pads and graphite flow fields (left), close-up of flow field structure (right).

The modus operandi for cell assembly was as follows:

1. dedicated anode side bipolar plate and flow field placed in position with four electrically insulated screws (Teflon® sleeves)
2. anode side gasket and GDL placed onto the flow field
3. MEA (anode side down) positioned onto the GDL
4. GDL and cathode side gasket placed on top of MEA
5. dedicated cathode side flow field and bipolar plate joined with the other components
6. first all four nut bolts were fastened by hand, then clock- and stepwise with spanners to ensure even force distribution and tight sealing

Figure 16: Fuel cell test bench.

The fuel cell test bench was designed by Roth [78] and provides a very reliable operation due to its analog and manual design. For the experiments conducted no elaborate load protocols had to be followed and the stable operation for a given load preset for up to 100 hours and more was crucial. The original design (see Figure 16) is for hydrogen PEMFCs. To be operated with DMFCs a peristaltic pump was used for the anode fuel feed.

After connecting the fuel cell with the test bench, the cell heating was set to a fixed temperature of 70 °C. During heat-up no oxygen or methanol was supplied to the cell, thus air was in the anode and cathode compartments. When the cell reached its set temperature the oxygen flow was started at 100 ml/min and the 1 M methanol flow at 10 ml/min. As soon as the anode compartment was completely filled with fuel, i.e. the MeOH feed reached the outlet, the flow was reduced to 3 ml/min. This practice ensured that the cell was fully supplied with fuel as soon as possible. The starting point of operation was defined as the moment when the flow was set to 3 ml/min. The different fuel cell operation conditions of the experiments can be found in chapter 3.3.

The shutdown procedures started with switching off the heating and stopping the oxygen and methanol flows. Pure nitrogen was used to purge first the cathode compartment and thereafter the anode compartment. Then the connections of cell and test-bench were removed and the cell disassembled. Disassembly was following the assembly procedure described above in reverse order. The handling of the removed MEA is described in detail in chapter 3.4.

3.3. List of samples

The overview in Table 5 shows all cathode samples being subjected to fuel cell conditions. Regardless of the further operation parameters for the specific sample, all MEAs were run under OCV conditions for 30 min. This was to fully humidify the MEA and enable it to be operated at a given potential. This break-in procedure is very short compared to commercial procedures of stack systems where durations of up to several days are not uncommon.

Table 5: Description of sprayed and decal MEA samples DMFC history.

runtime [min]	cell potential [mV]	anode feed	sprayed MEA	decal MEA
30	OCV	1M MeOH	MEA_2510	CCM-6
630	OCV	1M MeOH	-	CCM-7
6030	OCV	1M MeOH	-	CCM-5
30 / 60	OCV / 600	1M MeOH	-	CCM-3
30 / 60	OCV / 500	1M MeOH	MEA_2610	-
30 / 60	OCV / 400	1M MeOH	MEA_2710	CCM-4
30 / 60	OCV / 200	1M MeOH	-	CCM-8
30	OCV	1M EtOH	MEA_1910	-
30	"OCV"	H_2O	MEA_1908	-

A graphic illustration of the decal MEA sample operation conditions is given in Figure 17.

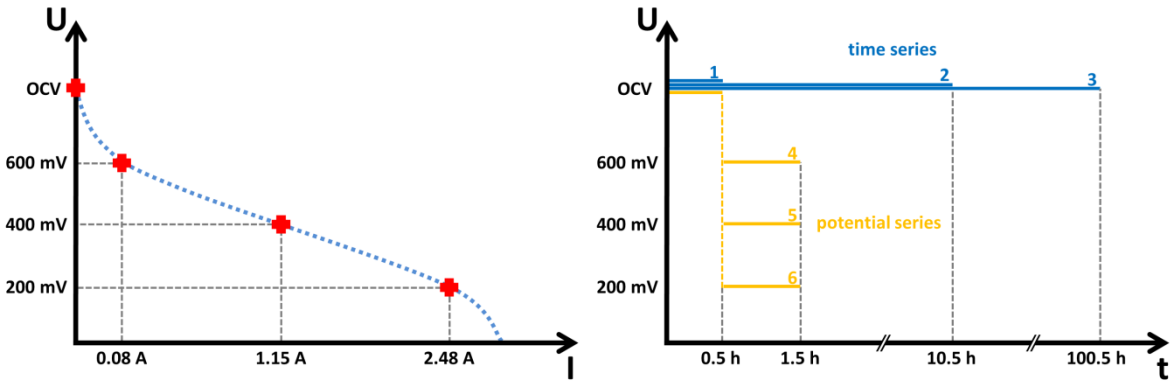

Figure 17: Diagram illustrating the DMFC operation parameters of the time series (1-3) and potential series (4-6) samples.

As all samples run through the necessary break-in procedure, a sprayed as well as a decal MEA were prepared for analysis immediately after break-in. Comparing these samples to MEA catalyst samples, which were never assembled in a DMFC, made it possible to monitor the changes induced by the break-in procedure.

Not listed in the table are the as-prepared samples, which were never assembled in a DMFC. There were two complete decal MEA catalysts processed to pellets right after fabrication. From

all sprayed MEAs there exist the 5 cm² testing stripes from the spraying process. These were also used to prepare pellet samples. In comparison there is a significant difference between the decal and sprayed as-prepared samples: the testing stripe is by a factor of 5 smaller than the whole 25 cm² electrode area of a decal MEA. Thus, also the amount of catalyst differs by a factor of 5 for these as-prepared samples.

3.4. Sample preparation

After dissembling the fuel cell, the still moist MEA was placed on a polycarbonate sheet anode side down and left to dry in air for about 30 min. Then the MEA was fixed, still with the anode side facing down, onto the sheet using adhesive tape and a second polycarbonate sheet was added on top as cover. This procedure was to ensure that no particles from the anode could be transferred onto the cathode during the following removal of the cathode catalyst.

The fixated MEA were further dried using an oven set to 60 °C under air for at least 3 hours. Afterwards the cathode catalyst layer was carefully removed using a scalpel. Immediately after the complete catalyst was removed the powder was weighted and 200 mg of cellulose were added. This mixture was grinded using an agate mortar and pistil till a homogenous powder was achieved. The powder was then transferred to a stainless steel pressing matrix (13 mm diameter) and pressed using a hydraulic press (pressure 5 tons for 1 min). The pellets were embedded in Kapton® tape for easy handling and protection from contamination.

After each sample all tools and fuel cell parts were vigorously cleaned with acetone and water and wiped dry. Only after all cathode samples were prepared the polycarbonate sheets were removed to expose the anodes and the anode samples were prepared in the same way as the cathode samples. This strict procedure ensured that all possible contamination with ruthenium from the anode material was minimized.

3.4.1. Reference samples (standards)

To prepare reference samples containing known amounts of ruthenium in the ppm range a tenfold dilution sequence of ruthenium(III)-chloride in methanol was used. Methanol as solvent was chosen because of the good solubility of $RuCl_3$ in MeOH and the possibility of evaporating at moderate temperatures.

In a small vial $RuCl_3$ was mixed with as much ICP grade MeOH as needed to form a 1000 ppm ruthenium solution. With this parent solution dilutions containing 100, 10, 1 and 0.1 ppm ruthenium were produced.

The highly hygroscopic ruthenium chloride contains crystal water. Because the amount of water is not precisely known, the solutions prepared in the aforementioned way do not contain the exact amount of Ru as calculated. Therefore the 1000 ppm parent solution was analyzed by ICP-MS to determine its ruthenium content. It was found that the actual amount of Ru was 860 ppm. This measured value of ruthenium content was used throughout the further analyses performed with these standards.

To produce the ruthenium reference pellets 0.5 ml of ruthenium dilution were added to 200 mg cellulose. After drying at 90 °C for 3 hours and grinding the cellulose powder, the pellets were pressed in the same way as the sample pellets (see description above).

For the references containing ruthenium and platinum 5 mg or 50 mg HiSpec 13100 (72 wt% platinum on carbon) were added to the 200 mg ruthenium cellulose powder to yield references containing ~1.5 wt% or ~15 wt% platinum, respectively.

3.5. Analysis methods

3.5.1. X-ray fluorescence spectroscopy

X-ray fluorescence spectroscopy measurements were carried out at the FLUO beamline at the ANKA synchrotron in Karlsruhe, Germany. The beamline is equipped with a double crystal monochromator, automated sample changer and a Vortex-60ET® SSD detector.

As mentioned in chapter 2.3, a way to reduce the generation of pile-up artifacts from the platinum had to be found. A set of filters was used to dampen the platinum M-lines as much as possible, without dampening the ruthenium fluorescence photons too much. The best tradeoff was found using the ruthenium-platinum reference samples and consisted of a stacked filter set of 40 µm copper, 20 µm cobalt and 15 µm titanium foils.

All measurements were done at a fixed x-ray energy of 27 keV. Each sample on the sample changer was carefully aligned to the point of x-ray beam and detector focus using a microscope with shallow depth of field. The accuracy of the sample position along the x-ray beam path was below 10 µm. Data acquisition and sample changer control were realized through the proprietary beamline control software.

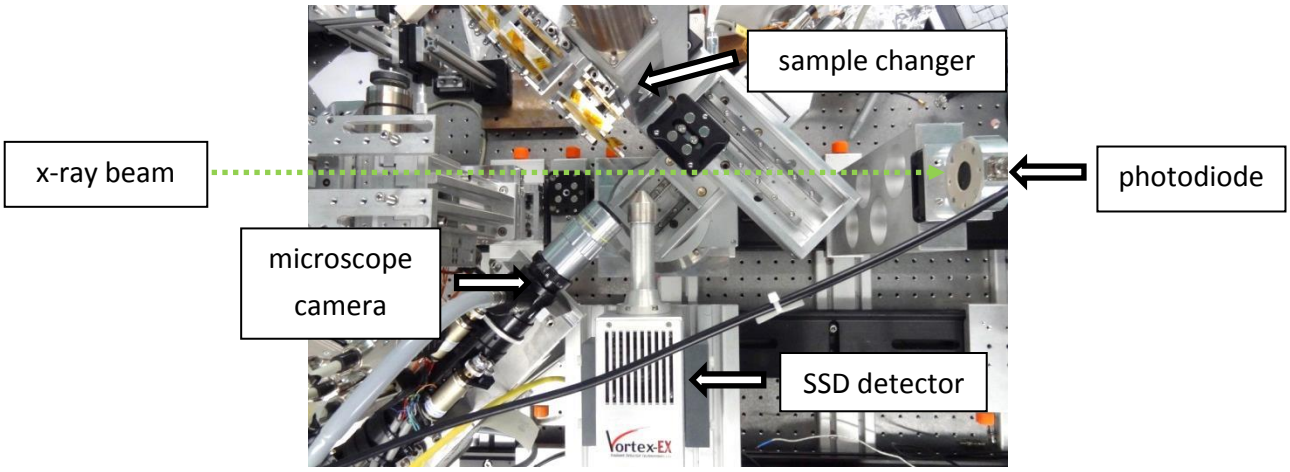

Figure 18: XRF beamline experimental setup of the FLUO beamline at ANKA, Karlsruhe.

Up to three sample pellets were mounted on a single holder (see Figure 19) and up to 7 sample holders were placed on the sample changer.

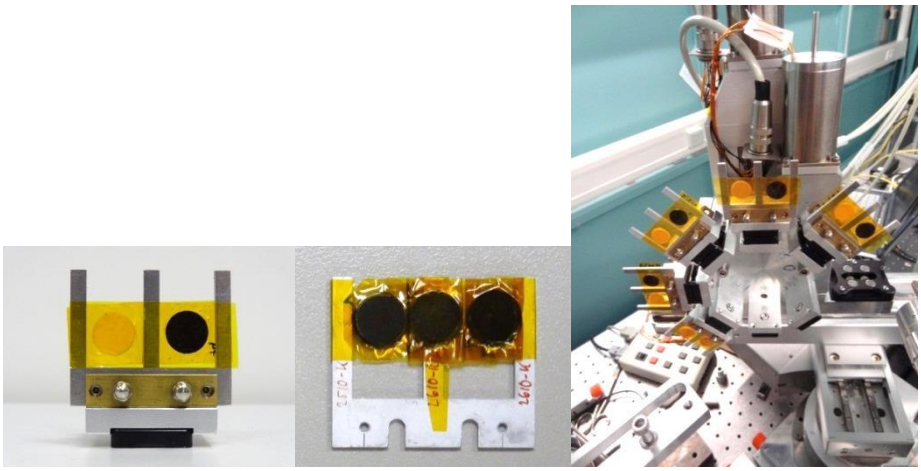

Figure 19: Sample holder with 2 (left) and 3 (middle) pellets mounted; sample changer with 5 out of 7 positions equipped with sample holders (right).

Before a new sample holder was positioned a short measurement without any sample in the beampath was recorded. Without a sample the relative x-ray intensity of the beam was recorded by a photodiode placed in front of the beam dump. This approach guaranteed that possible fluctuations in the x-ray intensity could be monitored and accounted for during data analysis. Each pellet was measured at three different positions on the pellet to check for any inhomogeneity in the pellet itself. Also at each of these three positions two spectra were recorded in direct succession to detect any possible variations in the detector system (i.e. SSD

detector, current amplifier, analog-digital conversion). This led to six fluorescence spectra for each sample.

Data analysis and fitting was done using the PyMca software package [79] provided by the Software Group of the European Synchrotron Radiation Facility (ESRF). First, all spectra were visually checked for any glitches or signs of detector saturation. Then one of the 1000 ppm ruthenium plus 15 wt% platinum reference sample spectra was used to calibrate the energy scale (correlate detector channels with absolute x-ray energy). With this calibration data a configuration file (see appendix, p. 86) for batch processing was generated. The processing of all spectra was then done using this single configuration file.

From the set of fitted parameters a subset containing only the platinum L-line and ruthenium K-line fitted curve areas was generated. Within this dataset a statistical analysis on the variation between the six spectra of each sample was conducted. It was found that the Pt L-line fitted areas show a standard variation up to 20 %, but the sum of all three L-line areas only varied by less than 5 %. The Pt L-lines are partly overlapping and therefore slight variations in the spectra could lead to significant differences in the fits of single peaks. The summed area of all L-line fits was more robust against this kind of influence. For the Ru K-lines the differences were greater. The Ru Kα lines fitted areas showed standard variations below 10 %, while for the much smaller Ru Kβ lines fitted areas up to 40 % variations were found. The Ru Kβ lines are comparably weak; Kα lines are expected to have ca. 5 times the intensity of the Kβ lines. So, the Kβ lines fit is much more susceptible to errors from noise and artifacts. For the calculation of ruthenium content in the samples the fitted areas of only the Ru Kα line and the summed Pt L-lines areas were used.

Because the scratched cathode samples contain not only cathode catalyst and migrated ruthenium, but also Nafion® and PTFE (see ink preparation in chapter 3.1.2), the amount of catalyst and therefore platinum is not known precisely. Assuming that the platinum content of the catalyst does not change significantly during operation, it is possible to use the platinum fluorescence signal to normalize the ruthenium signals. This can be expressed as the ratio:

$$A_{\mathrm{rel}}^{\mathrm{Ru}} = \frac{A^{\mathrm{Ru\ K\alpha}}}{A^{\mathrm{Pt\ L_1}} + A^{\mathrm{Pt\ L_2}} + A^{\mathrm{Pt\ L_3}}}$$

where A^X are the respective fitted areas.

To obtain quantitative Ru amounts a conversion factor for the normalized ruthenium signal is needed. To calibrate the XRF measurements reference samples as described in 3.4.1 were used. To account for possible matrix effects of the platinum catalyst references with no platinum, 1.5 wt% platinum and 15 wt% platinum were prepared. Figure 20 (no platinum), Figure 21 (1.5 wt%

Pt) and Figure 22 (15 wt% Pt) show plots of the data acquired on these groups of references as well as linear regression trend lines.

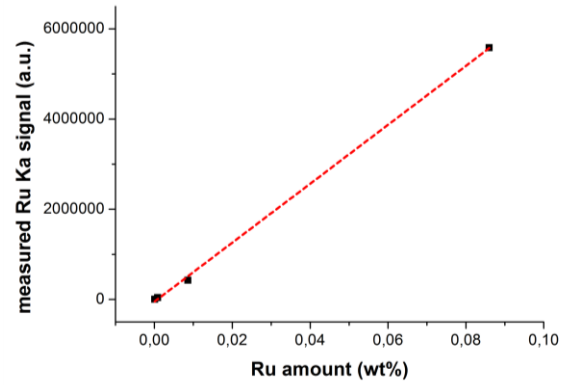

Figure 20: XRF calibration data for pure Ru standards.

With no platinum present in the samples (Figure 20) the linear dependency of ruthenium amount c_{Ru} weighted in and the integrated area of the Ru Kα line I_{XRF} can be described as follows:

$$I_{XRF} = -48684.38614 + 65351400 \cdot c_{Ru}$$

It is important to note, that even though there was no platinum in these samples, the same fitting parameters as for all other samples were used to maintain comparability (see appendix p. 86).

The next set of reference samples all contain 1.5 wt% platinum in addition to ruthenium. These samples were needed to determine the filters needed. In Figure 21 the ratio of the fitted areas under the Ru Kα and the Pt L lines is plotted against the amount of ruthenium in the reference.

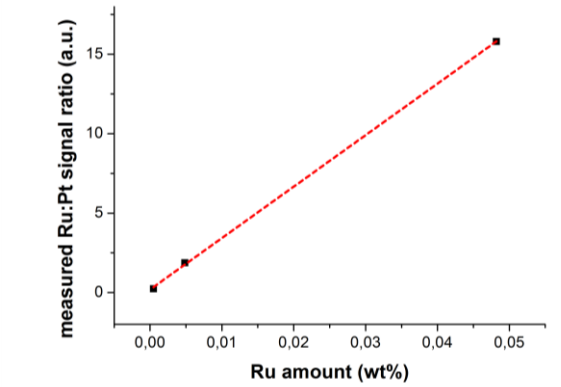

Figure 21: XRF calibration data for Ru standards containing 1.5 wt% Pt.

The data can be fitted by following linear regression:

$$I_{XRF} = 0.18844 + 324.10503 \cdot c_{Ru}$$

In Figure 22 the calibration data for ruthenium standards containing 15 wt% platinum is shwon.

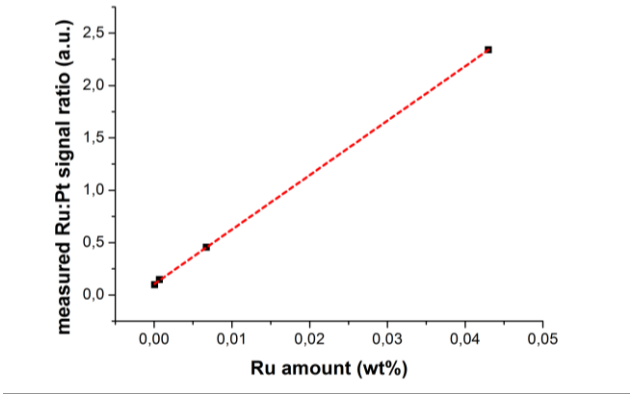

Figure 22: XRF calibration data for Ru standards containing 15 wt% Pt.

The corresponding linear regression is:

$$I_{XRF} = 0.1038 + 52.01521 \cdot c_{Ru}$$

Regardless of the amount of platinum present in the samples a linear dependency of Ru amount and fluorescence signal measured by XRF could be found. This shows that no nonlinear effects are present for XRF measurements of ruthenium samples which contain 0 – 15 wt% platinum as well.

The pure cathode catalyst contains 72 wt% platinum. Besides the actual catalyst, the scratched off samples from the MEAs cathode contained also Nafion®. Furthermore cellulose was added as binder to prepare the pellets for the XRF measurements. The final amount of platinum in the pellet samples amounted to approximately 15 wt% platinum. Using the equation from page 33 the ruthenium concentration c_{Ru} can thus be calculated from the XRF fits by:

$$c_{Ru} = 0.019225 \cdot \frac{A^{Ru\ K\alpha}}{A^{Pt\ L_1} + A^{Pt\ L_2} + A^{Pt\ L_3}} - 0.001996$$

This equation is only valid, as long as the prerequisite, that the platinum content of the cathode catalyst does not change, is met. Because all ruthenium fitted areas are normalized by the summed fluorescence of platinum from the sample, this is very crucial. The only ways the relative amount of platinum on the cathode side could change is by loss of platinum on the cathode itself or deposition of platinum dissolved at the anode. As has been shown by Ettingshausen et al. [80], [81], for PEMFCs the dissolution of platinum is strongly correlated with high cell potentials and repetitive potential cycling. The potential needed to dissolve significant amounts of platinum electrochemically is above 900 mV [53]. Such high potentials are found in a DMFC only during start-up / shut-down process and situations like fuel-, oxygen- or water-starvation [17]. The fuel cells investigated in this work were always sufficiently fed with methanol, oxygen and water. As all MEAs were only subjected to one steady state condition, there was only one start-up and shut-down event and no potential cycling occurring. Under these conditions one can assume, that there will be no significant change in platinum content of the cathode catalyst.

To estimate the minimum detection limit (MDL) of the XRF setup for measurements of ruthenium a samples without any Ru was analyzed. A pellet was prepared from HiSpec 13100 catalyst mixed with cellulose, containing about 15 wt% Pt. Fitting of the data with the same parameters as were used for the other samples analyzed in this work resulted in an apparent ruthenium content of ca. 0.012 wt%. This value is a sum of different data correction and fitting errors and has to be considered in the further analyses.

Further ICP-MS measurements of the as-received platinum catalysts actually revealed, that the as-received platinum catalyst contains traces of ruthenium (see chapter 4.6), although only about 0.001 wt%.

3.5.2. X-ray absorption spectroscopy

X-ray absorption spectroscopy is an element sensitive technique to analyze materials in respect to their local structure and composition without the need for a long distance ordering (in contrast to XRD). Its capability to analyze materials lacking a long range order, i.e. amorphous materials, liquids etc., makes it suitable for virtually all materials. Another advantage of XAS is the lack of requirements on the sample environment, like an ultra-high vacuum, which is needed for XPS measurements. This makes it ideal for in-situ measurements. The information gained by XAS includes number and type of the next neighbors of the probed atom species and interatomic distances. This is averaged over all probed atoms in the sample volume, thus making XAS a bulk method. A good introduction to XAS can be found in [82].

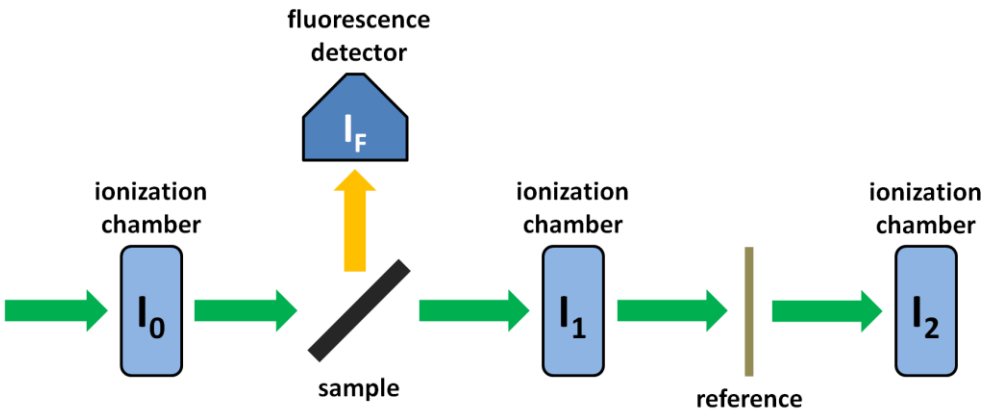

Figure 23: Schematic of a XAS experimental setup for transmission and fluorescence measurements, the monochromated x-ray beam is shown in green, while the fluorescence photons from the sample are depicted in orange.

In Figure 23 a schematic overview of an XAS experiment is depicted. A monochromated x-ray beam (depicted as green arrows) coming from a synchrotron source passes through an ionization chamber, which measures its intensity I_0. A fraction of the beam is absorbed in the sample to be measured, this results in a lower beam intensity I_1 detected by the second ionization chamber. In a similar manner a third ionization chamber determines the intensity I_2 after the beam passes a reference. This reference is used to calibrate the energy of the x-ray beam. Part of the absorbed x-ray energy in the sample is reemitted as fluorescence photons. These photons can be detected using a fluorescence detector, usually a photodiode or an energy dispersive x-ray detector. By varying the energy of the x-ray beam while recording the different intensities an absorption spectrum can be recorded. These spectra can be used to calculate the absorption coefficients of sample and reference by applying Lambert-Beer's law:

$$\mu_{\text{sample}}(E) = \ln\left(\frac{I_1}{I_0}\right)$$

or

$$\mu_{\text{sample}}(E) = -\ln\left(\frac{I_F}{I_0}\right)$$

$$\mu_{\text{reference}}(E) = \ln\left(\frac{I_2}{I_1}\right)$$

As an example the intensities I_0, I_1, I_2 and I_F of a platinum L_3 edge (11564 eV) EXAFS scan of a HiSpec 13100 carbon supported platinum catalyst sample are presented in Figure 24.

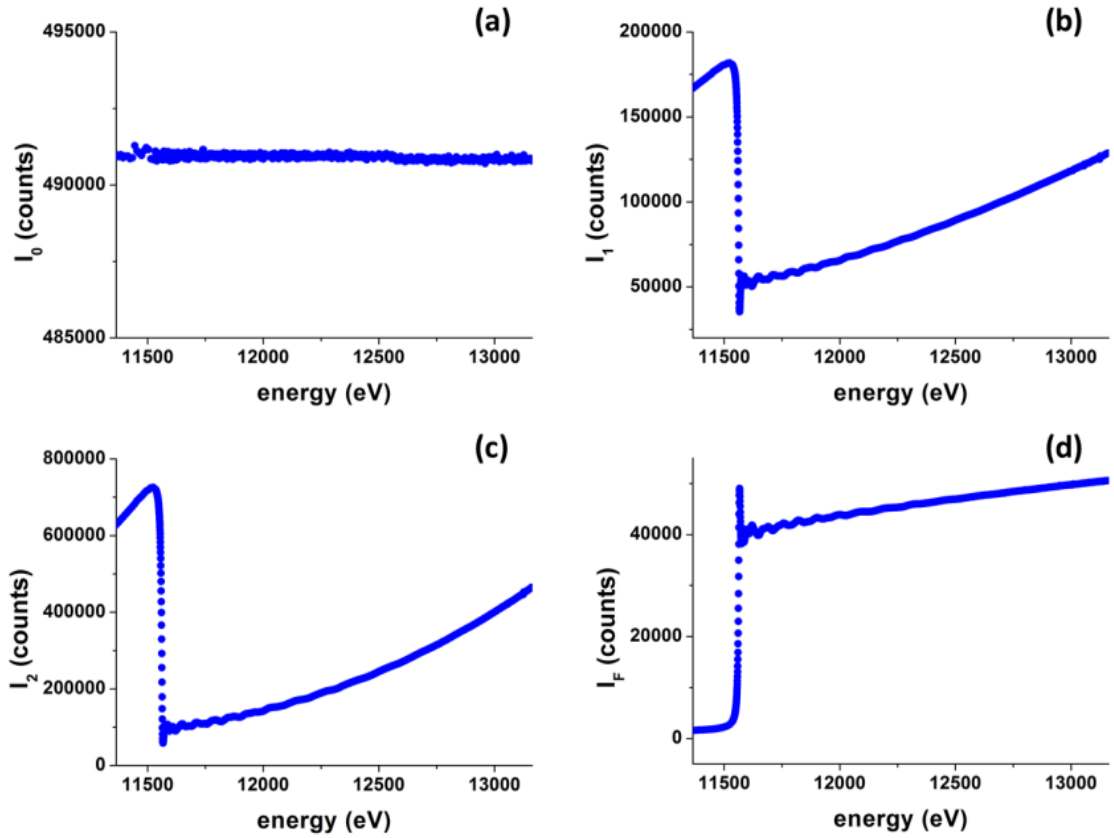

Figure 24: Raw data plots of the intensities measured by the first (a), second (b) and third (c) ionization chamber and the intensities measured by the fluorescence detector (d) versus energy.

Clearly the drop in transmitted x-ray beam intensity around the absorption edge at 11564 eV is visible. At this energy the x-ray photons can ionize an electron from the L_3 shell. All photons doing so transfer their energy to the electron and cease to exist, thus the intensity after the sample is lowered. The place of the missing electron in the L_3 shell is consecutively filled by an electron from an outer shell (M or N shell in case of platinum). This process generates a fluorescence photon or an Auger electron to compensate for the energy difference of the two shells. For low x-ray energies and low Z samples the Auger electron process dominates, for high x-ray energies and high Z material the emission of a fluorescence photon has a higher probability. Platinum falls in the latter category. The fluorescence signal from the sample was recorded by a photodiode detector and is shown in Figure 24 (d).

The intensity of the fluorescence signal increases at the absorption edge, because fluorescence photons can only be generated when an incoming x-ray photon was absorbed. Therefore, the transmission and fluorescence signals show inverse behavior. The signal of the last ionization chamber, situated behind the platinum reference, is shown in Figure 24 (c). Here the transmitted signal is again diminished by the absorption of x-ray photons inside the reference sample (in this case a Pt metal foil). To calculate the absorption coefficients of the intensity data the equations described above are used. The data reduction and analysis was done using the IFEFFIT software

package [83], especially the Demeter (Athena) program [84]. Applying Lambert-Beer's law (see equations above) a plot of the absorption coefficient can be generated as shown in Figure 25.

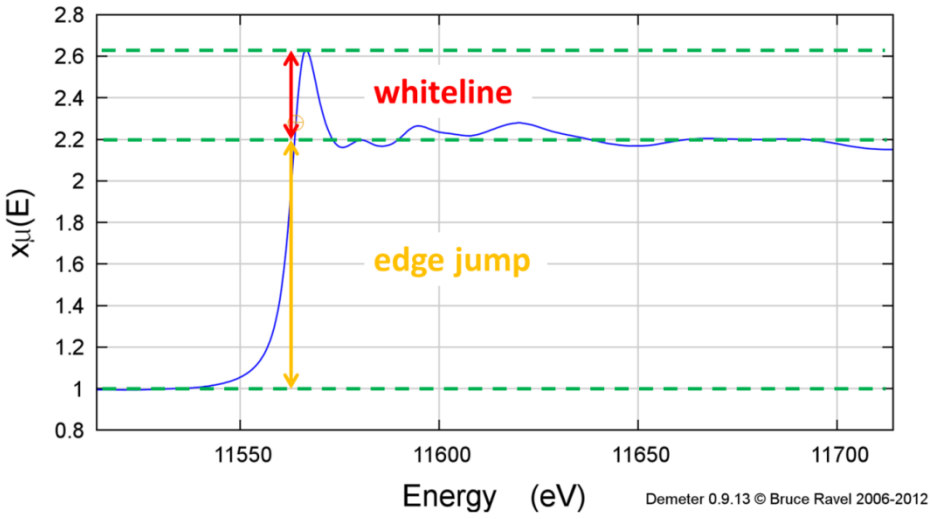

Figure 25: Plot of the absorption coefficient x_μ versus energy. The edge jump (orange) is defined as the difference between the baselines before and after the edge, while the whiteline (red) denotes the height of the edge above the after edge baseline.

The graph also visualizes the definitions of the edge jump (orange) and the whiteline (red). The edge jump height is used to normalize the absorption data. By normalizing the signal intensity it becomes possible to compare the data of different samples. The normalized spectrum of the data is shown in Figure 26.

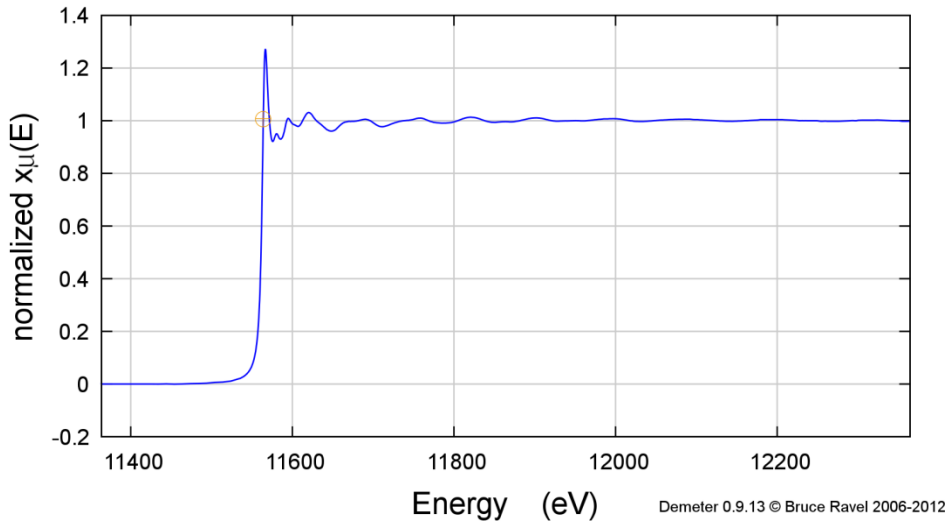

Figure 26: Plot of the normalized absorption coefficient derived from the data of the second ionization chamber (see Figure 24).

In this graph the shape of the absorption edge as well as the oscillations of the signal after the edge are clearly visible. From analysis of the oscillations details about the nearest neighbors of the probed atoms can be extracted. This process is described in detail e.g. in [82], [83]. Within this work the detailed analysis of the oscillations was not possible due to the low ruthenium concentrations found in the cathode samples (see chapter 4.1.2). But from the position and the height of the whiteline information about the oxidation state of the probed element can be drawn. As an example the spectra of a ruthenium metal and ruthenium dioxide powder are shown in Figure 27. The data is again normalized in respect to the height of the edge jump and plotted versus the energy of the x-rays.

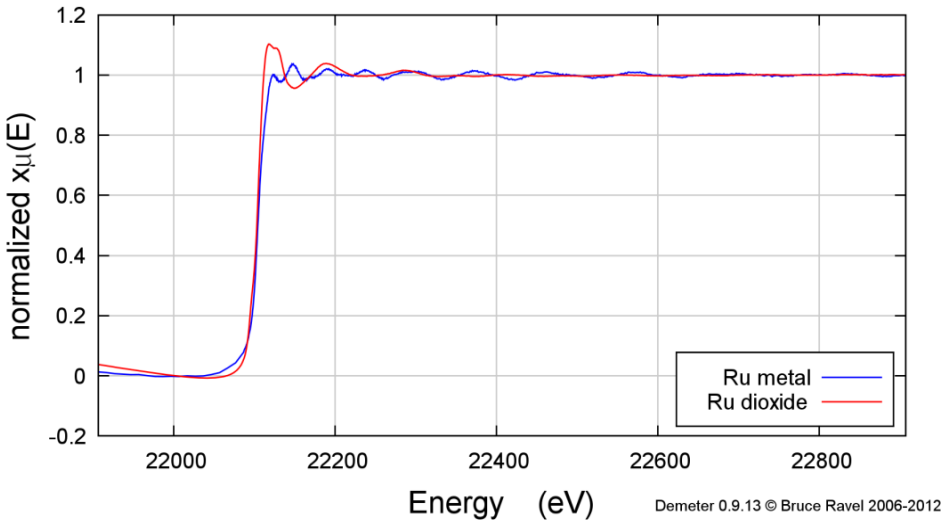

Figure 27: Ru K-edge XAS spectra of ruthenium (blue) and ruthenium oxide (red) demonstrating the sensitivity of the whiteline for the electronic state of the probed element.

As can be seen, the shape of the whiteline is very sensitive on the oxidation state of the probed element. Usually for metals a small whiteline corresponds to a low oxidation state, while a high and pronounced whiteline indicates a high oxidation state. With this fingerprinting technique a quick qualitative analysis of XAS spectra is possible.

All XAS experiments were conducted at the X1 (DORIS) beamline at the DESY synchrotron in Hamburg, Germany. A double crystal monochromator (Si 311) provides the tunable energy x-ray beam. The beam size was set to a width of 8 mm and a height of 2 mm. Three ion chambers record the beam intensity in transmission mode, while a passivated planar implanted silicon (PIPS) diode with 10 cm diameter was used to measure the fluorescence photons[3]. Between the

[3] In contrast to the SSD detector used for XRF a PIPS diode is not energy dispersive. Therefore it is not possible to record spectra of the incoming x-ray photons. On the other hand photodiodes can have a large detector area and are highly sensitive. They can detect single photon events, thus making them very suitable for detecting fluorescence photons for trace element analysis.

second and third ionization chamber a reference foil was mounted for energy calibration and verification. An automated sample changer was realized by utilizing the XY-goniometer and mounting the sample pellets on a ladder-like holder (see Figure 28).

Figure 28: Sample holder used for XAS measurements of pellets.

The beamline is operated via the proprietary control software 'Online'. A standard extended x-ray absorption fine structure (EXAFS) scan configured by the 'Online' software follows the scheme shown in Table 6.

Table 6: Overview of scan regions for EXAFS scans.

region	**energy range**	**step size**
pre-edge	250 eV before edge – 30 eV before edge	10 eV
XANES	30 eV before edge – 40 eV after edge	0.5 eV
EXAFS	40 eV after edge – 1000 eV after edge	0.02 k-space steps

For analysis of DMFC catalysts the elements platinum (K edge at 78399 eV, L_3 edge at 11564 eV) and ruthenium (K edge at 22117 eV) are of interest. These x-ray energies are high enough to penetrate a MEA as well as 1 mm liquid and several millimeters of light materials, such as graphite, polymers etc., thus a complete DMFC single cell. So in-situ measurements of fuel cells under operando conditions are possible.

3.5.3. Inductively coupled plasma mass spectrometry

A very sensitive method for detecting and quantifying elements in a liquid sample is inductively coupled plasma mass spectrometry [85]. Depending on the sample the detection limit can be as low as parts per trillion [86]. A small drop of the liquid sample (or dissolved sample) is sprayed into an argon plasma torch. The high temperature of the plasma (5,000 – 10,000 °K) evaporates the sample and ionizes the atoms. By means of an electric field the ions are directed into a mass spectrometer. Within the spectrometer a combination of electric and magnetic fields separates the ions according to their mass to charge (m/z) ratio. Using standards of known composition and concentration a quantitative measurement is possible.

The advantage of analytical methods like XRF or XAS is that they are non-destructive. On the other hand they are time consuming and complex due to the need for synchrotron radiation. Here ICP-MS can provide easier access to data on trace amounts of elements, at the cost of a destructive sample preparation.

To complement and verify the results of the XRF measurements ICP-MS analyses of some of the cathode samples were carried out. The samples chosen for analysis were the decal cathode samples, because they provide a time and potential series of DMFC operation, as well as the as-received HiSpec 13100 catalyst. About 5 mg of sample material were decomposed in a microwave autoclave at 150 °C using nitrohydrochloric acid and afterwards analyzed through an Element 2 ShieldTorch system from Thermo-Fischer Scientific as described below.

Considering the dissolution and migration of ruthenium, the questions arise which Ru species gets dissolved from the anode and in which form the migration through the membrane takes place. As mentioned in chapter 2.2, there are several possible sources of migrating Ru species present in the anode catalyst: 1) the platinum-ruthenium alloy, 2) separate ruthenium particles or islands on platinum particles, 3) ruthenium oxide and hydroxide species. The dissolution process itself could take place in different ways: 1) water or methanol soluble ruthenium species (e.g. hydroxides) are dissolved by the anode fuel feed, 2) ruthenium is electrochemically dissolved, 3) a chemical dissolution by other substances inside the DMFC. These other substances in the DMFC can be impurities like chlorine, as has been shown by the FZ Jülich [12]. When chlorine was added deliberately to the anode fuel feed an increase in the dissolved ruthenium in the anode exhaust feed of the fuel cell stack could be detected by ICP-MS. But not only impurities can lead to enhanced ruthenium dissolution. Formic acid as product of incomplete methanol oxidation, as shown by Totsuka et al. [46], [47], is also a possible corrosive agent. The formation rate of formic acid found was in the range of µM/min, but the corrosive effects on the catalyst might still be relevant.

To determine the non-electrochemical dissolution effects, portions of 30 mg of HiSpec 12100 platinum-ruthenium catalyst were added to 30 ml of water, 30 ml 1 M methanol and 30 ml 1 M formic acid, respectively. These suspensions were stirred for 1 h at room temperature. After

resting for 15 min the supernatants were filtered using a 0.2 µm syringe filter and the filtrates centrifuged for 15 min at 13000 min^{-1}. Now about half of the supernatants were carefully transferred to a clean vial and 3 ml of concentrated nitric acid were added for stabilization of any ions. The rest of the supernatant was removed and the solid residues were dried and analyzed with x-ray photoelectron spectroscopy (chapter 4.2). In Figure 29 an overview of the use of the samples from the leaching experiment is depicted.

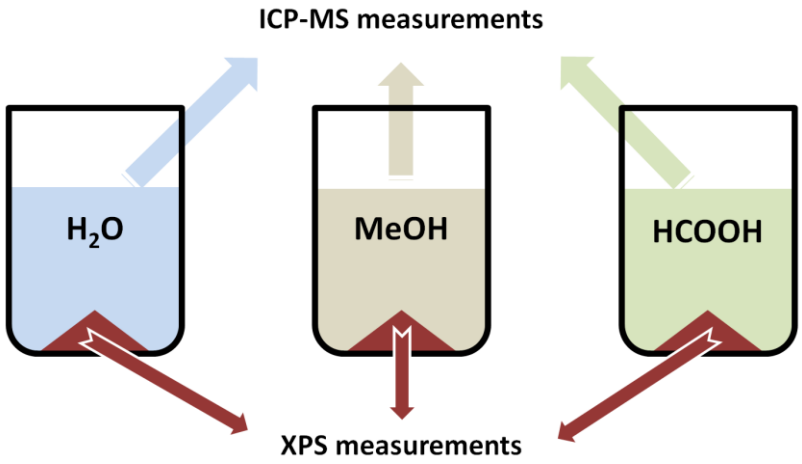

Figure 29: Illustration showing the samples derived from the leaching experiments of HiSpec 12100 anode catalyst in different solvents. The supernatants were analyzed by ICP-MS, while the dried solid residues were measured using XPS.

The solutions were stabilized by nitric acid and analyzed using inductively coupled plasma mass spectrometry. Before measurement the samples were decomposed in a microwave autoclave at 210 °C using nitric acid and afterwards analyzed through an Element 2 ShieldTorch system from Thermo-Fischer Scientific in peak-hopping mode. The parameters of operation can be found in the following table:

Table 7: ICP-MS operation parameters.

spacing	0.01 atomic mass units	auxiliary flow	0.9 l/min
points per peak	3	blend gas flow	0.1 l/min
scans per replicate	3	RF power	1.3 kW
integration time per point	300 ms	crossflow nebulizer flow rate	1.02 l/min
plasma flow	15 l/min		

All ICP-MS measurements were provided by Frank Kuppler at the biochemistry department of the Freie Universität Berlin, Germany.

3.5.4. X-ray photoelectron spectroscopy

Similar to XRF x-ray photoelectron spectroscopy also exploits the photoelectric effect, but in contrast to XRF spectra of the photoelectrons are taken. Because the mean free path for an electron in matter is very short, XPS is a surface sensitive method with a probing depth of about 1-3 nm.

When an incoming x-ray photon is absorbed by an electron, part of its energy is used to overcome the binding energy (BE) of the electron, while the remaining energy is converted to kinetic energy of the expelled electron (see Figure 30).

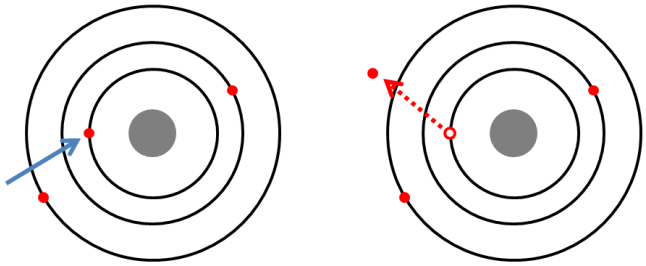

Figure 30: Principle of photoelectron generation.
(on the left) an x-ray photon (blue arrow) interacts with an inner shell electron, (in the right) the electron is ejected as an photoelectron.

Using a monochromated source of known wavelength, thus energy of the x-ray photons ($\nu_{phtoton}$), the binding energy of the electron can be calculated:

$$\mathrm{BE} = \nu_{photon} - (\nu_{electron,kinetic} + \phi)$$

where $\nu_{electron,kinetic}$ is the measured kinetic energy of the photoelectron and ϕ is the work function of the spectrometer. The binding energy is specific for each element and the orbital the electron is ejected from. Furthermore, the spin-orbit-coupling of atomic nucleus and its electrons leads to a splitting of the observed binding energies (p, d and f orbitals). Another influence on the BE is the chemical state of the atom. Different oxidation states implicate

variances in the energies of the orbitals and thus in binding energies. Careful analysis of the spectra and combined fitting of each element constituting a compound (e.g. spectra of metal and oxygen for a metal oxide) can provide precise chemical information. A good overview of the principles of XPS and the application of XPS to fuel cell research can be found in the review by Wieckowski et al. [87].

While it is possible to determine the general chemical state of the probed atomic species with XAS by fingerprinting (see chapter 4.1), usually the better approach is to analyze the shift in binding energy with x-ray photoelectron spectroscopy. Unfortunately XPS needs an elemental concentration in the range of atomic% and therefore is not suitable to measure the low Ru amounts found in the cathode catalyst samples. For the cathode catalyst samples the XAS fingerprinting technique was used to estimate the chemical state of the ruthenium (see chapter 4.1.2). Besides the anode catalyst samples also the residues from the leaching experiments (see chapter 3.5.3) were analyzed by XPS.

The measurements were conducted by Michael Bruns at the Karlsruhe Nano Micro Facility (KNMF), Germany. A Thermo Fisher Scientific K-Alpha XPS spectrometer was used with a microfocused, monochromated Al Kα x-ray source (400 µm spot size). To prevent any charge build-up, 8 eV electrons and low-energy argon ions of the K-Alpha charge compensation system were used. Acquiring and processing the data was done using the Thermo Avantage software (see [88]). One or more Voigt profiles were used to fit the spectra, while for quantification the analyzer function, Scofield sensitivity factors [89] and effective attenuation lengths (calculated using the standard TPP-2M formalism [90]) for photoelectrons were applied. All spectra were referenced to the C1s peak of hydrocarbon at 285.0 eV binding energy controlled by means of the well-known photoelectron peaks of metallic Cu, Ag, and Au, respectively.

3.5.5. X-ray powder diffraction

X-ray photons can be diffracted by the ordered atomic structure of a crystalline material [91]. The relation of the angle of the incoming photon ϑ, the wavelengths of the x-rays λ, the distance between the lattice planes d and the number of the observed diffraction maximum n is given by the Bragg equation [92]:

$$n \cdot \lambda = 2 \cdot d \cdot \sin(\vartheta)$$

Using a monochromated x-ray beam, it is possible to calculate the interatomic distance d. The diffraction pattern of a material would ideally consist of a series of infinitesimal sharp reflections (see Figure 31), where the intensity of the reflections correlates to the ratios of the atomic distances found in the sample.

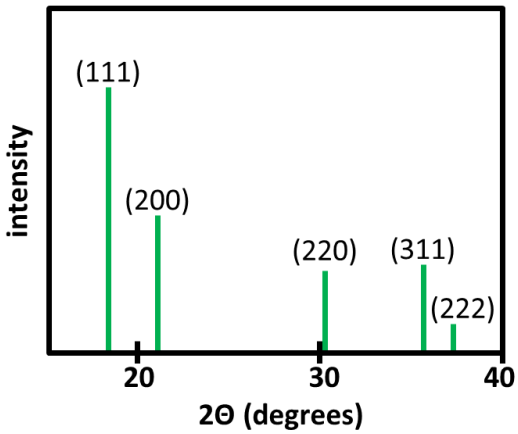

Figure 31: Theoretical diffractogram of platinum.

In the measurement of a real sample several deviations from this ideal case occur (see Figure 32). The width of the reflections becomes broadened by thermal movement of the atoms, defects and stress in the material, the finite size (or size distribution) of the crystallites and instrumental broadening. The position and intensity of the reflections on the other hand are influenced by factors like preferred orientation of the crystals, defects in the crystal structure, misalignment of sample and / or detector and others [93].

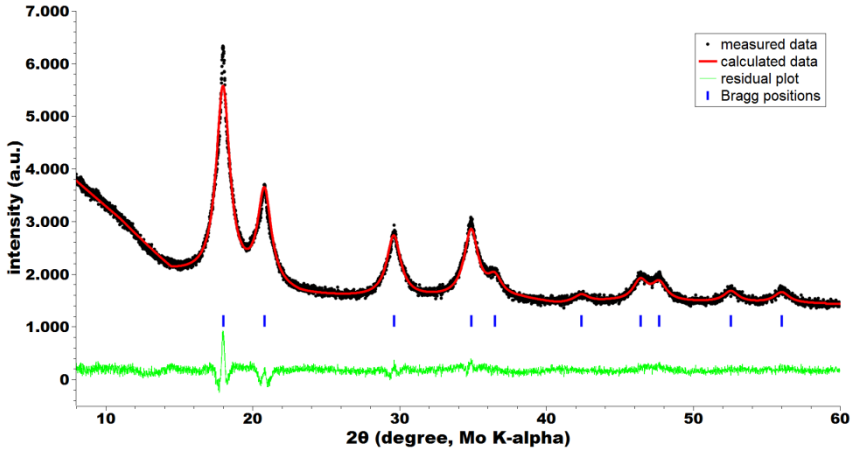

Figure 32: X-ray diffraction pattern and Rietveld refinement of a carbon supported platinum catalyst. Measured data points are black, fitted data is red, residual plot is green and Pt (fcc) Bragg positions are depicted in blue.

The effect of peak broadening due to finite crystallite size can be exploited to calculate the mean size of the crystallites. The relation of peak width B and crystallite size L is given by the Scherrer equation [94]:

$$\mathrm{B}(2\vartheta) = \frac{\mathrm{K} \cdot \lambda}{\mathrm{L} \cdot \cos(\vartheta)}$$

where K is the Scherrer constant. Using the full width half maximum (FWHM) to determine the peak width B and assuming spherical crystallites with cubic symmetry the literature value for K is 0.94 [95]. A more detailed look into the topic of size determination from XRD data can be found in [93].

All XRD measurements within this work were carried out using a STOE Stadi P diffractometer in transmission geometry. The instrument was equipped with a molybdenum x-ray source and a one-dimensional position sensitive detector (PSD). Calibration and determination of machine parameters were done by measurements of lanthanum hexaboride and silicon standards. Data conversion from the proprietary STOE raw format was conducted using the supplied STOE software, while all further data reduction and analysis was carried out using FullProf [96], [97] and WinPLOTR [98], [99].

Scratched off samples from MEA electrodes were used for XRD without any further processing like grinding. A small quantity of the powder sample was placed on a cellulose acetate foil inside the XRD sample holder. A drop of a 9:1 mix of amyl acetate and collodion was used to form a slurry, which then could be easily distributed over the middle part of the foil. While the sample was still wet a second cellulose acetate foil was placed on top of the slurry and the foils with the sandwiched sample were fastened inside the XRD sample holder by a metal ring with screws. Now the sample thickness was checked against a bright light source and adjusted if needed. Before measurement the samples were left to dry for at least 30 minutes. Diffractograms were recorded in a 2Θ range of 10 to 60 degrees with a step size of 0.01 degrees.

3.5.6. Cyclic voltammetry

Cyclic voltammetry is usually conducted in an electrochemical cell with a three electrode setup (see Figure 33).

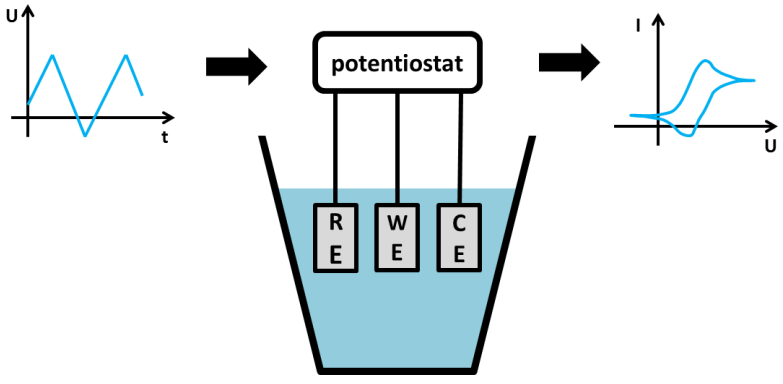

Figure 33: Illustration of a cyclic voltammetry experiment composed of electrochemical cell, reference electrode (RE), working electrode (WE), counter electrode (CE) and potentiostat.

The cell is filled with an electrolyte, in which the working (WE), counter (CE) and reference electrode (RE) are placed in close proximity. The working electrode is the actual sample to be measured, either as is (e.g. for a solid metal sample) or applied to a glassy carbon electrode (e.g. for powder samples). The glassy carbon itself is not participating in the electrochemical reactions[4]. The counter electrode, often a platinum mesh, should also be chemically stable and inert and provide a high surface area. The function of the counter electrode is to provide as many charge carriers as are needed for the reaction(s) taking place at the working electrode. The reference electrode is used to measure the actual potential of the WE. For cyclic voltammetry a potentiostat applies a varying current between WE and CE, in such a way that the potential between WE and RE follows a saw tooth shape (see Figure 34). Plotting the current between WE and CE versus the potential of the WE in respect to the RE gives the voltammogram. Details on the analysis of voltammograms can be found in [100], [101].

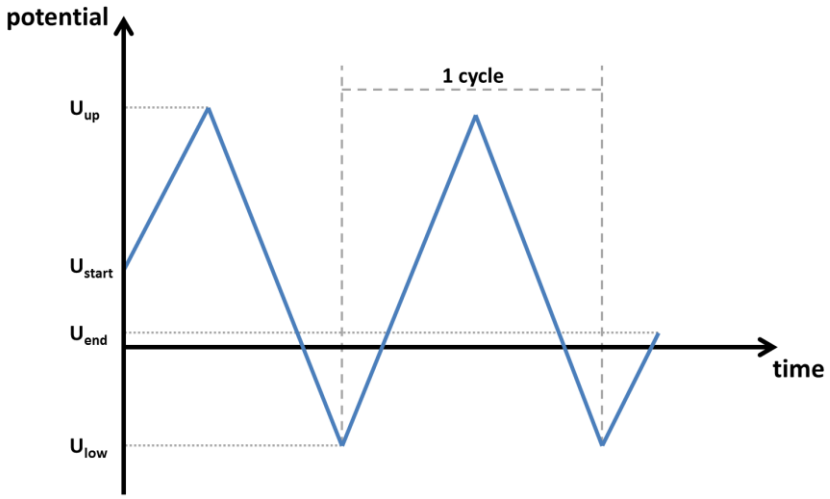

Figure 34: Change of potential over time for a cyclic voltammetry experiment.

Important parameters of a CV measurement are the lower and upper potential (u_{low}, u_{up}) limit as well as the sweep rate and number of cycles. Also the potential at start and end of the measurement can be chosen according to the experimental needs. The potential limits are dictated by the reaction to be analyzed as well as the stability of the electrodes and the electrolyte.

For cyclic voltammetry measurements a 5-port glass electrochemical cell with a total volume of 75 ml was used. Samples were prepared on a 0.5 cm² glassy carbon electrode. Besides this working electrode a 1 cm² platinum sheet as counter electrode and a gaskatel HydroFlex®

[4] For many reactions glassy carbon is chemically stable and inert, but not for all. For example the redox reactions involving vanadyl sulfate are actually catalyzed on carbon. Also at potentials above ca. 1.5 V vs. RHE carbon is electrochemically oxidized to CO_2.

normal hydrogen reference (NHE) electrode were connected to a Gamry Reference 600® potentiostat. The electrolyte was deaerated with pure nitrogen for at least 30 min prior to any measurement. Only during measurements the nitrogen flow was stopped to avoid disturbances, still a nitrogen atmosphere above the electrolyte was maintained at all times.

Prior to measurement, the glass cell was cleansed by repetitive rinsing with boiling 35% sulphuric acid and ultrapure water. Electrolyte solutions were produced from 'Milli-Q' purified water, Merck Ultrapur® perchloric acid and Merck LC-MS grade methanol. For all CV experiments described in this work either 0.1 M perchloric acid or an aqueous solution containing 1 M methanol and 0.1 M perchloric acid were used as electrolyte. Samples were prepared by mixing 5 mg scratched catalyst powder (or the as-received commercial HiSpec® catalysts) with 5 ml of 5% Nafion solution and transferring 15 µl of this suspension onto the glassy carbon electrode. Afterwards the electrodes were dried at 60 °C for at least 2 h.

All measurements were done within the potential range of 0.05 to 0.7 mV versus NHE. A higher upper limit would have been beneficial to analyze the methanol oxidation, but at the risk of electrochemical ruthenium dissolution [64], [102]. All samples were characterized by 5 scans between 0.05 and 0.7 mV vs. NHE at a sweep rate of 50 mV/s.

Data acquisition and analysis were done using the Gamry Framework® and Gamry EChem Analyst® software packages, respectively. Whenever normalized data is presented within this work the normalization was following the established procedure used for platinum electrodes [103]. Under the assumption that on each surface atom of platinum a hydrogen atom adsorbs, it is possible to calculate the surface area of the Pt electrode by determining the saturated hydrogen coverage charge $Q_{hydrogen}$ and dividing it by the 210 µC/cm² for a polycrystalline Pt surface. To determine $Q_{hydrogen}$ a baseline from the linear part of the voltammogram was defined. Using this baseline the area under the hydrogen desorption peak was determined. This area equals to the total charge transferred during hydrogen desorption. The equivalent Pt surface area was calculated from that charge by dividing it by the average charge per square centimeter of a polycrystalline platinum surface. The resulting equivalent Pt surface area was then used to convert the measured current values to current densities, thus normalizing the data to the area of the electrode/catalyst. This procedure is only valid for polycrystalline Pt electrode surfaces. Calculating surface areas e.g. for platinum-ruthenium electrodes in this way will give wrong values. To compare samples of the same composition to each other the derived current densities still can be applied. In this work only the relative change between samples of the same composition is of interest, not the absolute value of the surface areas.

4. Results

4.1. X-ray absorption spectroscopy

There are a number of publications [17], [104]–[107] demonstrating the advantages and limitations of in-situ XAS fuel cell experiments. Problems arise when the element to be analyzed is present on both sides of the MEA, because in standard XAS transmission setups the whole probed sample volume adds to the signals observed. Especially the small contribution of low amounts of Ru migrated to the cathode side would be completely covered by the strong signal from the anode catalyst. A deconvolution of the two spectra would not be possible. Also the platinum signals from anode and cathode cannot be fully separated.

To circumvent this problem of superposition of anode and cathode spectra, a cathode catalyst was chosen, which contained neither ruthenium nor platinum. Besides platinum, pure palladium or binary palladium alloys are good catalysts for the reduction of oxygen [108]. An advantage of palladium is its K edge energy of 24350 eV, which puts it close to the ruthenium K edge at 22117 eV. This made it possible to cover both absorption edges in a single (long) EXAFS scan, therefore acquiring information from anode (Ru) and cathode (Pd) almost simultaneously. By choosing a palladium-cobalt alloy as cathode catalyst this principle can also be applied to cobalt and platinum. Scanning the Co K edge at 7709 eV and platinum L_3 edge at 11546 eV in one scan provides data from cathode and anode catalysts, respectively. The advantage of this approach is, that while acquiring information e.g. on the ruthenium deposition onto the cathode by observing changes in the PdCo cathode catalyst complementary data on the changes of the anode catalyst (loss of Ru) is recorded simultaneously.

The preparation of the 20 wt% PdCo (2:1) on carbon cathode catalyst followed a modified recipe originally by Li et al. [109]. 25 mg NH_4Cl and 125 mg H_3BO_3 were added to 10 ml Milli-Q water as complexing agent and buffer, respectively. Then 5.6 ml of 25 mM $Pd(NO_3)_2$, 5.6 ml of 12.5 mM $Co(NO_3)_2$ and 78.56 mg Vulcan XC-72 were added and the pH of the dispersion was adjusted to pH 8.5 by adding ammonia. While the dispersion was mixed by an ultrasonic disintegrator 20 drops of 0.1 M $NaBH_4$ solution were used to reduce the metal precursors over a course of 5 min. The dispersion was mixed for another 15 min before it was filtered through a 0.1 µm polycarbonate filter. After rinsing it twice with Milli-Q water the catalyst was dried for 10 min at 80 °C. As anode catalyst the commercial JM HiSpec 12100 was used. The fabrication using the wet spraying airbrush technique was the same as described in chapter 3.1.1.

4.1.1. In-situ DMFC double edge XAS

The following data was measured using a three window DMFC described by Dixon et al. [17]. The cell is shown in Figure 35. The three window design was developed for spatially resolved analyses of the catalysts. In the experiments conducted in this work only the middle beam window was used.

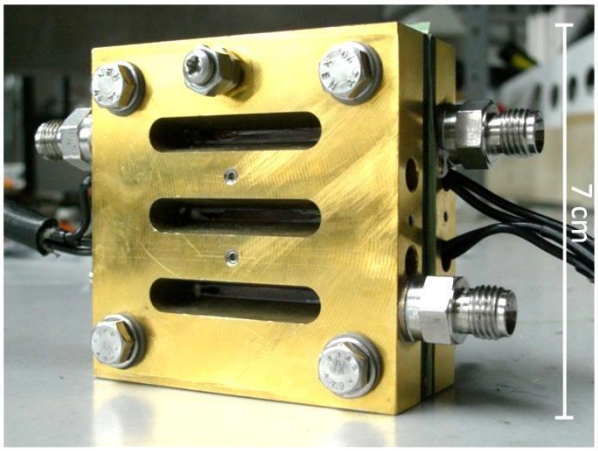

Figure 35: Photograph of the three window DMFC cell used for in-situ XAS experiments.

With the PdCo / PtRu MEA mounted inside the cell an EXAFS scan of the palladium and ruthenium edges was performed. This was done as a reference for the in-situ experiments as well as to test the feasibility of scanning the two edges at once. In Figure 36 the spectrum of the two absorption edges is shown.

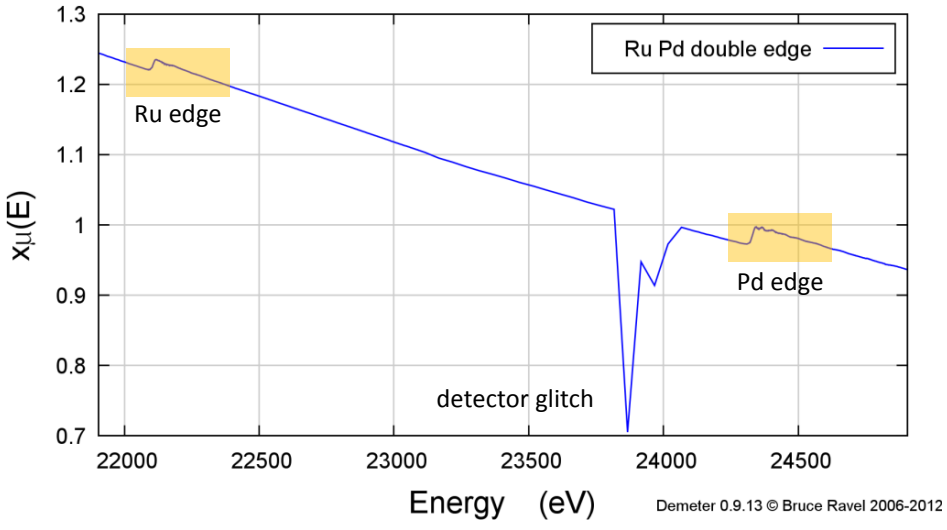

Figure 36: In-situ XAS scan of a PtRu-PdCo MEA showing absorption edges for ruthenium (at 22117 eV) and palladium (at 24350 eV).

The beamline control software was programmed with a standard EXAFS scan of the Ru and Pd edge and a rapid (1 data point every 50 eV) scan in between. This rapid scan is close to the maximum speed the monochromator at the X1 beamline at Hasylab could achieve. Therefore, the data taken between 23117 and 24100 eV is not reliable and contains glitches. But the data quality taken at the Ru and Pd absorption edge energies is good. Truncating the data produces two separate datasets for Ru and Pd. These separated spectra are shown in Figure 37. As has been described in chapter 3.5.2, the whiteline shape can be used as fingerprint for the electronic state of the probed element. The ruthenium spectrum points to mostly oxidized Ru, while the palladium seems to be mostly metallic.

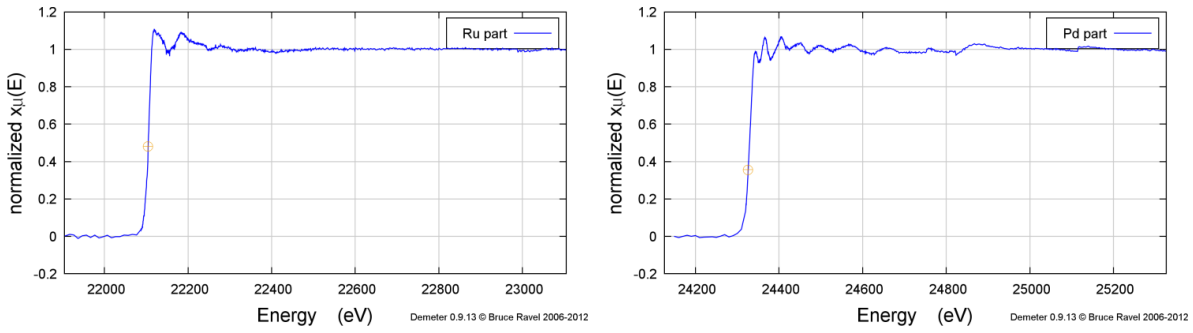

Figure 37: Normalized data sets for Ru (22117 eV) and Pd (24350 eV) edges taken from the in-situ double edge spectrum. The orange crosshairs denote the edge energies of 22.117 keV and 24.350 keV respectively.

In a similar way in Figure 38 the spectrum of the cobalt and platinum edge from this PdCo-PtRu MEA is depicted.

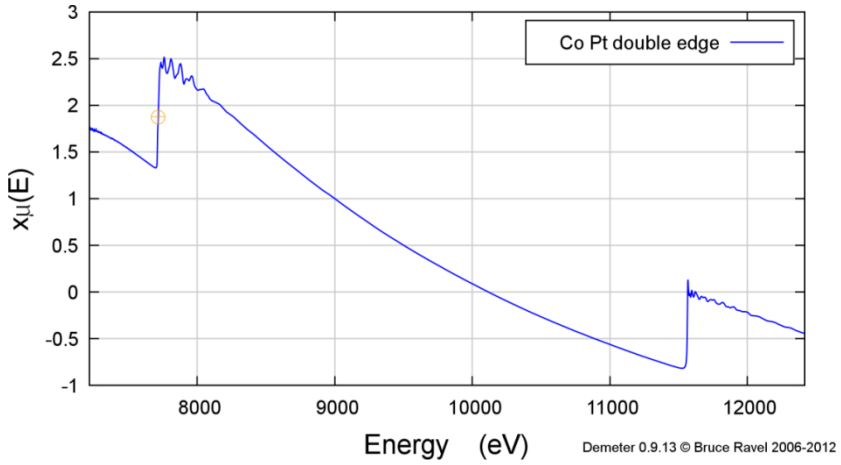

Figure 38: In-situ XAS scan of a PtRu-PdCo MEA showing absorption edges for cobalt (at 7709 eV) and platinum (at 11564 eV).

Again, the spectrum can be transformed into two separate spectra of the cobalt and platinum edges respectively (see Figure 39). The whiteline of the cobalt points to mostly metallic cobalt, while the platinum is mostly oxidized.

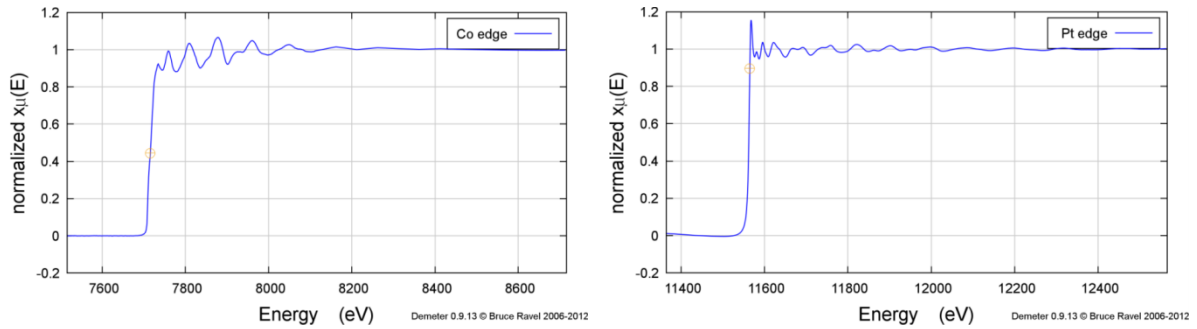

Figure 39: Normalized data sets for Co and Pt edges taken from the in-situ double edge spectrum. The orange crosshairs denote the edge energies of 7.709 keV and 11.564 keV respectively.

After this initial scan further scans of the catalysts under different operation conditions were taken in-operando. Analyzing the spectra recorded at different potentials during DMFC operation of the PdCo-PtRu MEA did not provide any evidence of Ru migration or any associated change in the catalysts. No additional Pd-Ru scattering path was found in the Pd spectral data from the cathode side during operation. The most reasonable explanation is that the amount of transferred ruthenium during the XAS experiment is too low to be detected.

4.1.2. Ex-situ XAS on pellet samples

XAS measurements were carried out on all cathode sample pellets. This includes the samples from MEAs prepared by Airbrush® spraying as well as by the decal transfer method. The samples can be categorized in two groups: 1) samples from MEAs being subjected to DMFC conditions and 2) samples taken from MEAs directly after fabrication. Samples within each group are very similar, thus only one spectrum of each group is shown exemplarily.

To estimate the actual amount of ruthenium transferred to the cathode side during operation at different potentials and for different times, ex-situ pellet samples were prepared (see chapter 3.4). As the catalyst was originally spread over an area of 25 cm^2 on the MEA the relative concentration per cm^2 was increased ca. 19 times by pressing 1.3 cm^2 pellets from the same catalyst. So compared with the in-situ experiments these measurements had a ca. 20-fold increase in sensitivity.

XAS Ru K edge scans of the pellets provide a first evidence of ruthenium deposited onto the cathode catalyst. As an example the Ru K edge spectrum of a cathode catalyst sample operated for 30 min in a DMFC at open circuit voltage condition is given in Figure 40.

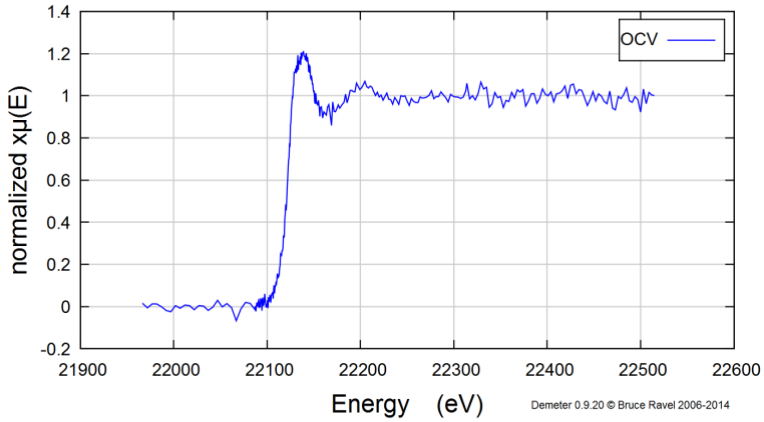

Figure 40: XAS Ru K-edge (22117 eV) raw data spectrum of a sprayed MEA cathode catalyst operated for 0.5 h at OCV in a DMFC.

The edge jump height of the absorption data shown in Figure 40 is about 0.025. This is about 50 times less than the edge jump observed for the platinum edge of the cathode catalyst (see Figure 25). This small edge jump and the signal-to-noise ratio of this spectrum imply that the ruthenium content of the sample is very low. Besides the catalyst from the actual 25 cm² area of the sprayed MEAs also the catalysts from the smaller (5 cm²) test areas were used to fabricate pellets (see chapter 3.1.1 Figure 14). This part of the MEA was never assembled in a DMFC and was thought to be used as reference of the catalysts state prior to DMFC operation. Remarkably the XAS scans of these pellets show a ruthenium absorption edge as well (see Figure 41), even if the edge jump is only about 0.002.

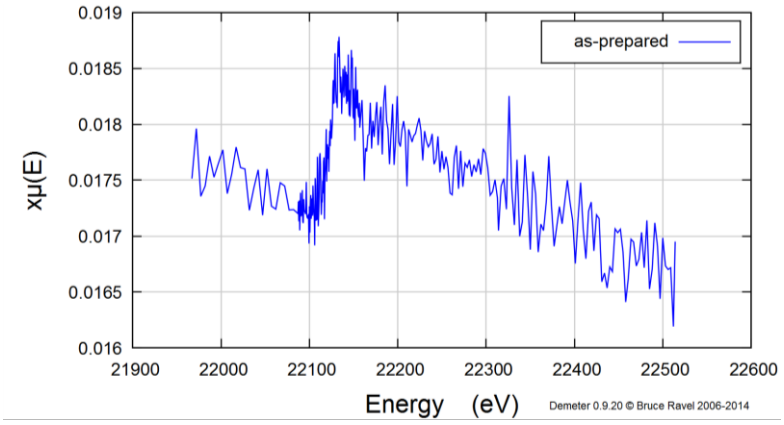

Figure 41: XAS Ru K-edge (22117 eV) raw data spectrum of a sprayed MEA cathode catalyst directly after fabrication.

These catalyst samples were processed to pellets directly after the sprayed MEA had dried. This implies that already during MEA preparation a significant amount of ruthenium was transferred through the membrane onto the cathode catalyst. Comparing the edge jumps of the spectra depicted in Figure 40 and Figure 41, the jump height is about 30 times less for the test area pellet. Taking into account that the catalyst amount from the MEA is about five times higher than that from the test field, this would indicate that ca. 15% of the Ru in the sample run under DMFC conditions was already transferred during preparation. This is a very simple approximation of the relative Ru contents of the two samples and these XAS measurements do not provide any quantitative information. A quantification of the amounts of Ru in the samples was done by XRF and is presented in chapter 4.4.

As was discussed in chapter 2.2 the PtRu alloy catalyst contains several ruthenium species, like hydrous and anhydrous oxides. Some of these are soluble in water and / or alcohols. When preparing the ink for MEA spraying these species are dissolved. Ruthenium ions might travel together with the liquid phase of the ink onto the cathode side before the heating fixture can evaporate the solvents. This is the main reason why a second MEA fabrication technique was included in the experiments for this work. With the decal transfer method, as described in chapter 3.1.2, the two electrodes are hot-pressed onto the membrane after drying.

The XAS data quality of the samples is not good enough for a full EXAFS analysis. However, the shape of the whiteline can provide information about the chemical state of the probed element as was shown in chapter 3.5.2. In Figure 42 the two XAS spectra from chapter 3.5.2 are shown again. The metallic Ru is characterized by a very small whiteline, whereas a ruthenium-(II)-oxide sample produces XAS spectra with a pronounced whiteline.

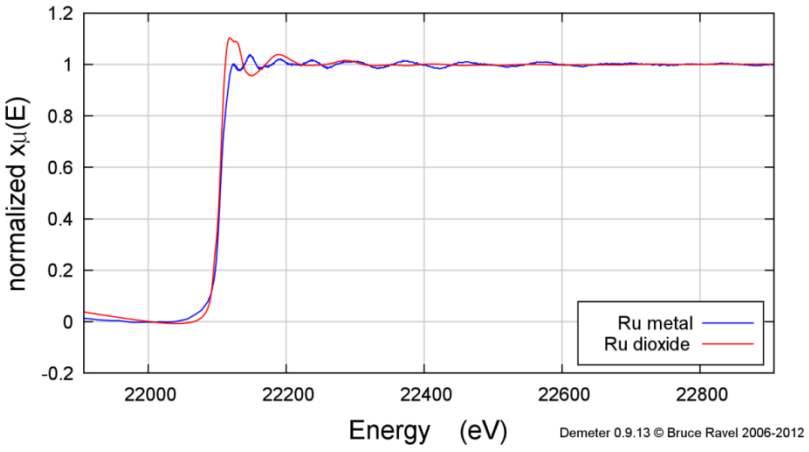

Figure 42: Normalized XAS Ru K edge spectra of ruthenium metal (blue) and ruthenium dioxide (red).

This can be exploited as a fingerprinting method to estimate the chemical state of Ru, though only the differentiation between mostly metallic or mostly oxidic Ru is possible. Neither it is

possible to distinguish different oxidation states nor to differentiate between e.g. Ru^{2+} and a mixture of metallic ruthenium and Ru^{4+}. Nonetheless this becomes important when the ruthenium concentration is too low to analyze the electronic state by other means like XPS (see following chapter). Using this fingerprinting technique the Ru species in the sprayed MEA cathode samples can be identified as mostly oxidic as can be seen by the pronounced whiteline (see Figure 40). As any ruthenium ions migrating onto the cathode during DMFC operation encounter a pure oxygen atmosphere at the cathode, this is to be expected. The XAS spectrum in Figure 41 is extremely noisy, so it is not possible to say whether the Ru on the cathode side of a pristine, sprayed MEA is oxidic or metallic.

The XAS Ru K edge spectra of the anode samples also are very similar to each other. Again only one representative spectrum is shown in Figure 43. The whiteline is not as pronounced as for a fully oxidized ruthenium sample (see Figure 42). This implies, that at the anodes only a fraction of the ruthenium is oxidized, while a significant part is metallic.

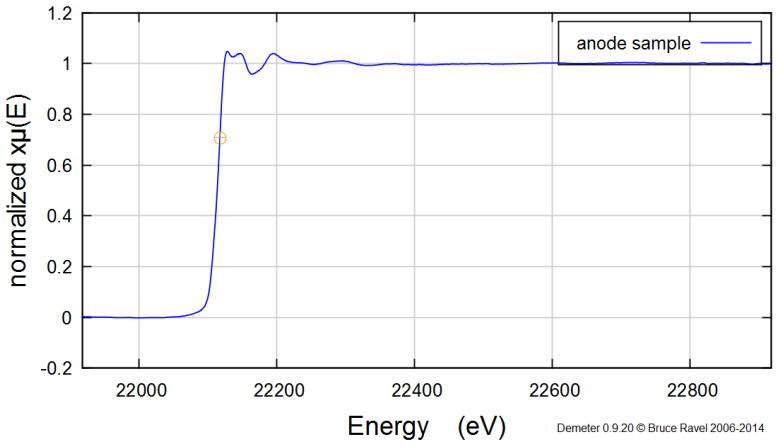

Figure 43: Normalized XAS Ru K edge spectra of a typical anode catalyst sample pellet.

4.2. X-ray photoelectron spectroscopy

X-ray photoelectron spectroscopy utilizes the fact, that the binding energy of the outer electrons of an atom is very sensitive to the electronic state of the atom. By fitting of the spectroscopic data and comparison with tabulated binding energies for different compounds, a detailed analysis of the sample composition can be obtained.

The samples of interest to this work had two major shortcomings in terms of XPS analysis. First of all, the Ru signals of the 3d electron orbital are very close to the carbon 1s signal. Second, a concentration of at least some atom% is needed to acquire reasonable XPS spectra.

This makes it impossible to use (laboratory) XPS for analysis of the cathode catalyst samples, as their Ru content is in the ppm range (see chapter 4.4). To assess the chemical state of Ru in the cathode catalyst samples XAS fingerprinting was used instead (see previous chapter). However, analyses of the anode material were possible and have been done on all samples.

The ruthenium content of the anode catalyst samples was ca. 25 wt% and therefore high enough to be analyzed by XPS. Acquiring data on the composition of the anode catalyst before and after operation provides information on the Ru species, which were preferably dissolved. But also XPS analysis of the anode catalyst samples proved to be challenging. Because the Ru 3d and C 1s signals overlap, fitting and deconvolution is associated with uncertainties. Recording spectra of the Ru 3p signal omits this problem, but the 3p signal is much weaker than the 3d. Therefore the signal-to-noise ratios of Ru 3p spectra are much lower. To illustrate these challenges the spectra and corresponding fits of an anode catalyst sample XPS measurement are shown in Figure 44. The ruthenium spectra was fitted using two fits, one for metallic ruthenium (fit A, Ru $3d_{5/2}$ at ca. 280 eV) and one for ruthenium oxide (fit B, Ru $3d_{5/2}$ at ca. 281.4 eV). These values are in good agreement with other published measurements [110].

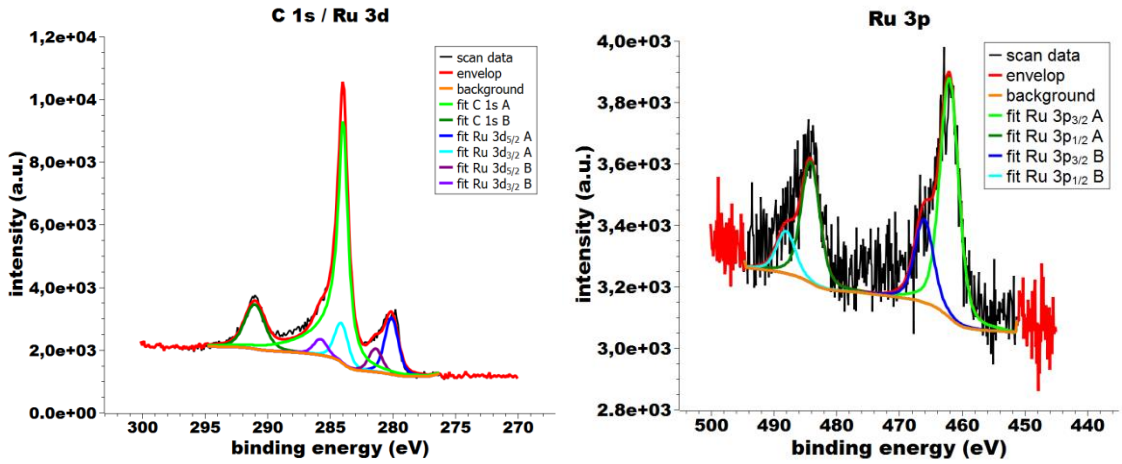

Figure 44: XPS spectra of an anode catalyst sample: (on left) carbon 1s and ruthenium 3d spectrum, (on right) ruthenium 3p spectrum

Ruthenium 3d and 3p XPS spectra of the decal MEA anode catalysts are shown in Figure 45 and Figure 46, respectively. The relation between sample name and the sample history is listed in Table 8 below:

Table 8: Description of the decal MEA samples.

Sample name	History
CCM-1	as-prepared sample
CCM-2	as-prepared sample
CCM-3	30 min at OCV + 60 min at 600 mV
CCM-4	30 min at OCV + 60 min at 400 mV
CCM-5	6030 min at OCV
CCM-6	30 min at OCV
CCM-7	630 min at OCV
CCM-8	30 min at OCV + 60 min at 200 mV

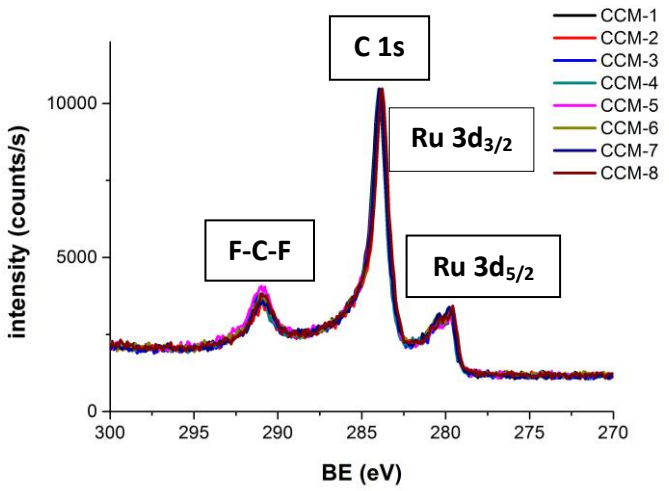

Figure 45: XPS spectra of all decal anode catalyst samples before and after operation in different DMFC conditions showing the C1s and Ru3d peaks.

As mentioned before the carbon 1s peak around 284 eV and the ruthenium 3d peak around 280 eV slightly overlap [111]. The second carbon peak shown in the spectrum at 291 eV is attributed to carbon bonded to two fluorine atoms. The source for this peak is the Teflon® backbone of the Nafion® ionomer. All decal MEA samples show similar Ru 3d XPS spectra.

The Ru 3p peaks are not obscured by any other signals. But due to a lower cross section the signal is much weaker. The 3p peak is split into two separate peaks because of the spin-orbit coupling as described in chapter 3.5.4.

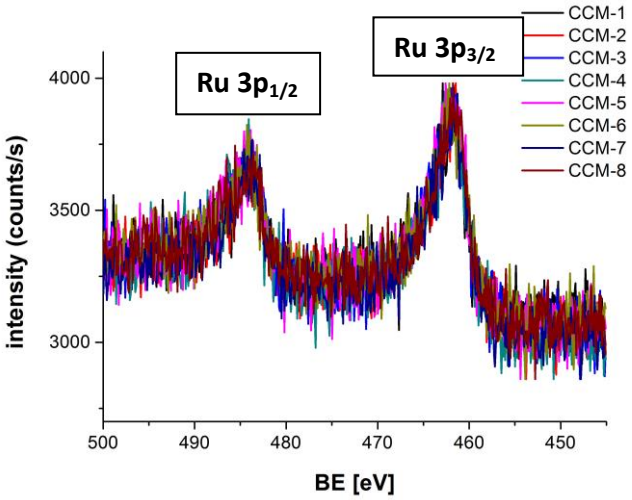

Figure 46: XPS spectra of all decal anode catalyst samples before and after operation in different DMFC conditions showing the Ru3p peaks.

There are no visible differences between the XPS spectra of the different decal anode samples. Also detailed fitting and analysis did not provide any evidence of significant changes. There might be two explanations for the observed results:

1) the changes to the catalysts might be too small to be detected by XPS,
2) the catalysts surface composition returned to the same stable composition of PtRu alloy phase and ruthenium oxide species when the wet MEA was removed from the DMFC and dried under air.

XPS was also used to analyze the dried residues from the dissolution / leaching experiments (see chapter 3.5.3). After three samples of HiSpec 12100 platinum-ruthenium anode catalyst were subjected to a dissolution treatment in water, methanol and formic acid, respectively, the solid residues were dried. The supernatants were filtered, centrifuged and analyzed by ICP-MS (see chapter 4.6). XPS measurements of the powder samples did not provide any insight which ruthenium species was dissolved. Even though the treatment with formic acid led to significant Ru dissolution, the composition of the residues was nearly identical. Again the aforementioned difficulties and low amounts of dissolved Ru species did not lead to any significant changes of the XPS spectra.

The spectra of the three anode catalyst samples subjected to the described leaching experiment are shown in Figure 47. There are no significant differences between the spectra. In comparison to Figure 45 the carbon peak around 291 eV is missing, because these samples did not contain any Nafion® and therefore no carbon atoms bonded to two fluorine atoms.

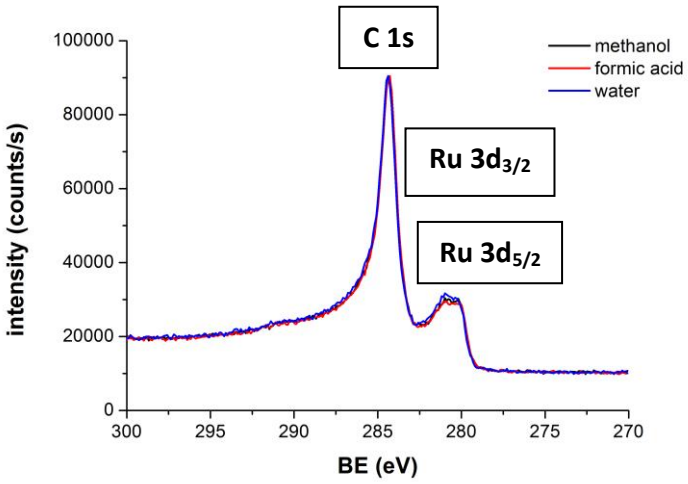

Figure 47: XPS C1s and Ru3d spectra of the three anode catalyst samples after the leaching experiments in methanol, formic acid and water respectively.

Also the spectra of the ruthenium 3p peaks do not show any differences between the samples, as can be seen in Figure 48.

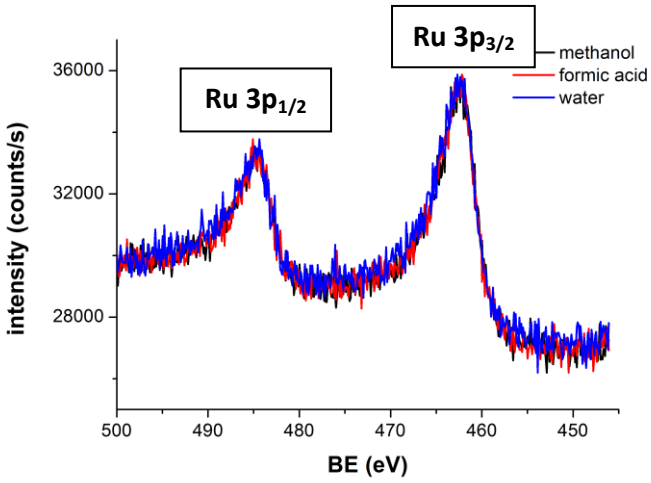

Figure 48: XPS Ru3p spectra of the three anode catalyst samples after the leaching experiments in methanol, formic acid and water respectively.

4.3. X-ray powder diffraction

XRD was carried out on all anode and cathode decal MEA samples as well as on the as-received commercial catalysts. X-ray diffraction only probes the crystalline fraction of the sample. Non-crystalline components, e.g. amorphous oxides or hydroxides, will not appear in the diffractograms. In Figure 49 two x-ray diffraction patterns of the Johnson Matthey carbon supported platinum-ruthenium and pure platinum catalysts are shown.

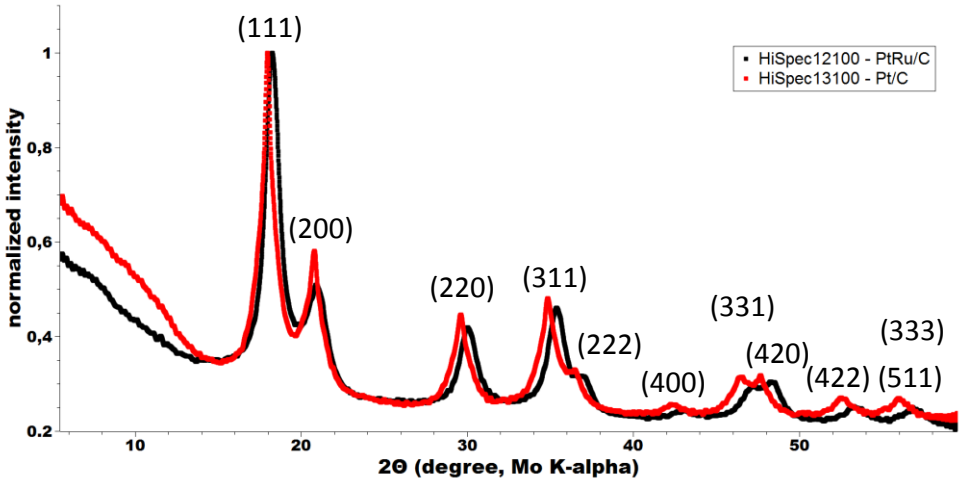

Figure 49: Normalized XRD diffractograms of anode (HiSpec 12100) in black and cathode (HiSpec 13100) catalysts in red; for the reflections of the PtRu catalyst the shift towards higher 2Θ values is clearly visible.

Both catalysts, the pure platinum HiSpec 13100 as well as the platinum-ruthenium alloy HiSpec 12100, only show reflections from a face centered cubic (fcc) structure. Antolini [112] and Arico [113] have shown, that up to 60 atomic percent of ruthenium, a platinum-ruthenium alloy stays in the platinum fcc structure. Only at higher Ru contents a change to the ruthenium hexagonal close-packed (hcp) structure will occur. For Ru concentrations below 60 atom% only a shift of the fcc reflections towards higher 2theta values is observed, corresponding to a lowering of the interatomic distances in the lattice. This is similar to Vegard's law, which describes the change in crystal lattice parameter for alloys formed by two metals of the same crystal structure. From the change in lattice parameter of a sample between the values for pure platinum and pure ruthenium the content of ruthenium can actually be estimated.

Even though no other crystalline phase is visible in the diffractograms, a ruthenium dioxide samples was measured as well. The normalized diffractogram is shown in Figure 50.

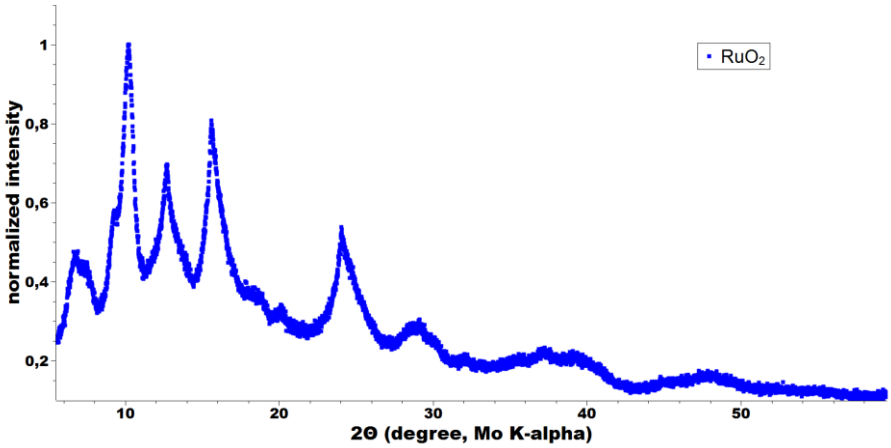

Figure 50: Normalized XRD diffractogram of a Ru oxide sample.

Ruthenium dioxide shows several prominent reflections below 2Θ values of 17 degrees and another one around 24 degrees. None of these reflections is visible in the diffractograms of the catalysts shown in Figure 49. Also none of the samples measured in this work showed any sign of a separate ruthenium dioxide phase. Therefore, all Rietveld refinements have been carried out using only a single platinum fcc phase.

A typical Rietveld refinement using FullProf® of the anode catalyst (HiSpec 12100) is shown in Figure 51. The difference between the data (red) and the calculated fit (black) is shown by the residual plot in blue.

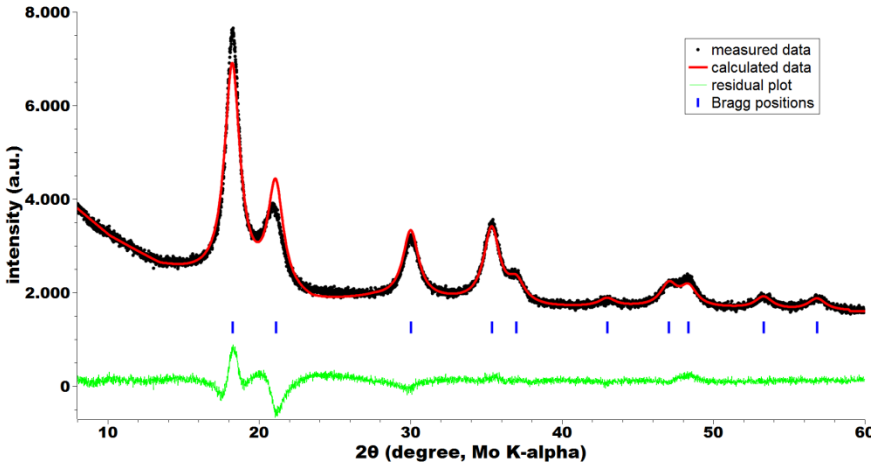

Figure 51: X-ray diffraction pattern and Rietveld refinement of HiSpec12100 anode catalyst. Measured data points are black, fitted data is red, residual plot is green and Pt (fcc) Bragg positions are depicted in blue.

The deviation of the measured data from the theoretical diffraction pattern is due to defects and strain in the nanoparticles. This is especially pronounced for the anode catalyst samples, because of the additional strain introduced by the incorporation of Ru into the Pt lattice. Similar observations have been made by Paterson [114] and Ustinov et al. [115]. In their work a correlation between the number of stacking faults in an fcc crystalline material and the shift and broadening of the XRD reflections was shown. A detailed study on the correlation of crystal imperfections and resulting changes in the diffractograms of a nanocrystalline catalyst was conducted by Kandemir et al. [116].

The diffractograms of the decal MEA cathode samples all looked very similar to one another (cf. Figure 32) and Rietveld refinement of the data backed this observation. In Table 9 the lattice parameters and mean crystallite sizes of the cathode catalyst samples are listed.

Table 9: List of parameters obtained from Rietveld refinement of XRD data from decal MEA cathode samples.

sample	description	$g_{cathode}$ [Å]	$d_{cathode}$ [Å]
CCM-1	as prepared	3,916	33,28
CCM-2	as prepared	3,916	34,57
CCM-6	0.5 h OCV	3,918	35,29
CCM-7	10.5h OCV	3,914	33,94
CCM-5	100.5h OCV	3,917	36,90
CCM-3	0.5 h OCV + 1h 600 mV	3,917	33,79
CCM-4	0.5 h OCV + 1h 400 mV	3,917	35,83
CCM-8	0.5 h OCV + 1h 200 mV	3,916	33,40

With two decal MEAs being analyzed as prepared (CCM-1 and CCM-2), an estimate of the spread of values from Rietveld refinement is possible. The mean platinum lattice parameter found in the cathode catalyst samples is 3.916 Å, which is in good agreement with the literature value of 3.92 Å and the expected slightly smaller value for nanometer sized particles [117]. None of the samples shows a significant change in lattice parameter or mean particle size. The only exception is the mean crystallite size of the CCM-5 cathode sample. This sample was run under OCV conditions for 100.5 h. The increased size could be due to Ostwald ripening of the catalyst particles over time [35], [118]. But taking into account the other two samples of the time series, no consistent trend of particle growth with time is visible. Even though growth of the catalyst particles during operation is a known phenomenon in this case it is assumed that there is no real growth. The spread of the size distribution is just larger than estimated by the two as-prepared samples.

The picture is basically the same for the decal MEA anode catalyst samples. In Table 10 the fitted values from Rietveld refinement of the anode catalysts data are listed.

Table 10: List of parameters obtained from Rietveld refinement of XRD data from decal MEA anode samples.

sample	description	g_{anode} [Å]	d_{anode} [Å]
CCM-1	as prepared	3,859	16,75
CCM-2	as prepared	3,866	15,94
CCM-6	0.5 h OCV	3,870	17,57
CCM-7	10.5h OCV	3,856	16,85
CCM-5	100.5h OCV	3,873	17,82
CCM-3	0.5 h OCV + 1h 600 mV	3,865	16,68
CCM-4	0.5 h OCV + 1h 400 mV	3,869	17,49
CCM-8	0.5 h OCV + 1h 200 mV	3,867	16,79

As has been explained above, the lattice parameter for the PtRu alloy particles is smaller than that for pure platinum. Based on the findings of Aricò et al. [113] the mean lattice parameter of the anode catalyst crystallites of 3.866 Å corresponds to approximately 50 atom% of ruthenium, which is in good agreement with the manufacturers analyses (see Table 2).

Neither the lattice parameter nor the mean crystallite size show any significant change or any correlation with the history of the sample. The crystalline structure of the cathode and anode catalysts crystallites did not change within the timescale / potential range, which has been investigated. Obviously, the crystalline fraction of the PtRu anode catalyst is not the part, which is susceptible to ruthenium dissolution. And the amount of Ru deposited on the cathode side is either too small to be detected or not crystalline.

4.4. X-ray fluorescence spectroscopy

X-ray fluorescence spectroscopy was applied in order to quantify the amounts of ruthenium present in the cathode catalyst samples. All cathodes were prepared from the same batch of HiSpec 13100 carbon supported platinum catalyst. As has been shown in chapter 3.5.1 the XRF measurement results suffer from a 0.012 wt% baseline, which has to be considered.

4.4.1. Comparison of preparation techniques

In chapter 4.1.2 it was shown that already during preparation a transfer of ruthenium onto the cathode takes place. The samples analyzed were prepared by the Airbrush® technique (see 3.1.1), where liquid catalyst inks are sprayed onto the Nafion® membrane. Zelenay et al. [11] observed a transfer of ruthenium in their DMFC setup as soon as the MEA was humidified. So the wet conditions during the MEA fabrication could be responsible for the Ru migration. To test this assumption a second MEA fabrication technique was used. With the decal transfer method (see 3.1.2) the catalyst layers are also prepared from a wet catalyst ink, but on separate transfer mediums and dried before being hotpressed onto the membrane. Therefor the catalyst layers (and the membrane) do not come into contact while they are humidified. In Table 11 the ruthenium concentrations found in the as-prepared Airbrush® and decal cathode samples using XRF are listed.

Table 11: XRF data on the as-prepared MEA cathode samples.

sample name	description	Ru concentration (wt%)
CCM-1	as-prepared decal MEA	0.023
CCM-2	as-prepared decal MEA	0.026
MEA_1908	as-prepared sprayed MEA test area	0.023
MEA_1910	as-prepared sprayed MEA test area	0.03
MEA_2510	as-prepared sprayed MEA test area	0.016
MEA_2610	as-prepared sprayed MEA test area	0.018
MEA_2710	as-prepared sprayed MEA test area	0.022

Also for the MEAs prepared by the dry decal technique, ruthenium transfer to the cathode side is observed. The concentrations determined for the two decal MEAs are about twice as much as the XRF baseline value of 0.012 wt% (see chapter 3.5.1), on average 0.024 wt%. Substracting the baseline indicates, that during the decal process ca. 0.012 wt% ruthenium were added to the cathode. The amounts of Ru in the sprayed MEA cathode samples show a wider spread of values between 0.016 wt% and 0.03 wt%. On average the as-prepared Airbrush® cathode samples contained 0.022 wt% Ru. Subtracting the 0.012 wt% rbaseline, the wet spraying process added ca. 0.01 wt% Ru to the cathode. This is slightly less than the transfer found during the dry decal process. In contrast to the observations of Zelenay et a. [11] the wet conditions during preparation did not enforce the migration of Ru.

Interestingly, the cathode samples after DMFC operation show much higher ruthenium concentrations for the sprayed than for the decal MEAs. The following table lists the amounts of Ru found in the samples run for 30 min under OCV conditions as well as the mean value from the potential series for both preparation techniques.

Table 12: Comparison of amounts of migrated ruthenium in decal and sprayed MEA cathode samples.

sample	Ru concentration (wt%)		difference in Ru concentration (wt%)
	decal MEA	sprayed MEA	
0.5 h at OCV	0.137	0.278	0.141
mean of potential series	0.223	0.445	0.222

The first set of samples was subjected to DMFC open circuit conditions for 30 min. The difference between the two preparation methods is about 0.141 wt%. The second set of values is the arithmetic mean of 3 decal or 2 sprayed samples run for 30 min under OCV conditions and thereafter subjected for 1 h to a cell potential of 600, 400 and 200 mV in case of the decal samples or 500 and 400 mV in case of the sprayed samples (see chapter 4.4.2). The difference here is about 0.222 wt%. Even considering the value of 0.023 wt% migrated ruthenium after the decal fabrication, the transfer of Ru during DMFC operation is about two times as high using a sprayed MEA compared to the decal MEAs.

Taking everything into account the findings can be summarized as follows: During the preparation process of the MEA a ruthenium transfer from anode to cathode catalyst occurred. Ru was transferred during the wet spraying preparation as well as during the dry decal fabrication as was confirmed by XAS and quantified by XRF measurements. That a transfer also occurs with the 'dry' decal methods was unexpected. Since no aqueous phase was present when cathode and anode where joined with the membrane during hotpressing a different migration process was obviously in effect then the one proposed by Zelenay. A conclusive explanation cannot be drawn without further studies of possible migration mechanisms in dry Nafion® membranes.

The large differences in migrating Ru under DMFC conditions for sprayed and decal MEAs may be related to the heated fixture used for spraying. In the ink dissolved Ru species are present. When the ink is sprayed onto the heated membrane the migration starts but is not fast enough to fully reach the cathode before the solvents are evaporated. The soluble ruthenium species are deposited therefor inside the membrane and close to the electrode-membrane interface. When the DMFC is assembled and humidified these soluble ruthenium deposits get dissolved again and finish their migration onto the cathode leading to a larger transfer of ruthenium during early operation. Another possibility is that during the decal MEAs fabrication the composition of the anode catalyst changes. Because of the elevated temperatures during hot-pressing ruthenium hydroxides might be transformed to more resilient ruthenium oxides. Because hydroxide species are generally considered to be more prone to dissolution [45] than oxides this would lead to different dissolution behaviors. A final conclusion cannot be drawn from the data available and this question would need to be addressed in future experiments.

4.4.2. Potential series

Different studies [17], [43], [80], [119] have shown, that during fuel cell operation the catalyst is subject of changes, including oxidation / reduction and reordering. All of these changes were linked to the applied potential. It was expected, that the most pronounced correlation of Ru dissolution would be with cell potential [120]. The Ru concentration versus the cell potential for MEAs prepared by the decal (black) and Airbrush® methods (red) are shown in Figure 52.

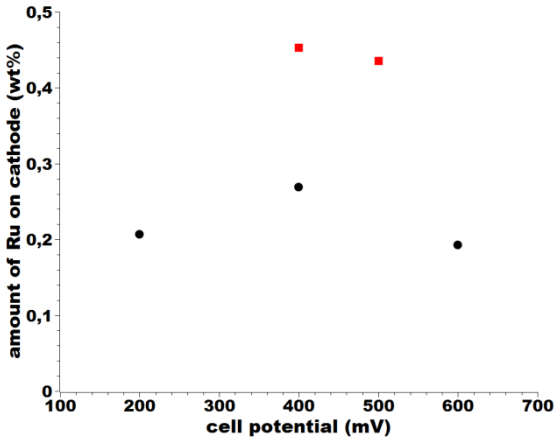

Figure 52: Ru concentrations in cathode catalyst samples (decal in black, sprayed in red) subjected to different potentials for 1 h.

Remarkably, there are very little differences in Ru amount in the cathode samples operated at different cell potentials. Overall, the sprayed MEA cathode samples show a higher Ru content as the decal MEA cathode samples. This offset is discussed in chapter 4.4.1.

The following table lists the samples of the potential series and the corresponding ruthenium amounts found on the cathode catalysts.

Table 13: Ruthenium concentrations of cathode samples subjected to different cell potentials for 1 h.

sample	preparation technique	description	Ru amount (wt%)
CCM-3	decal	0.5 h OCV + 1h 600 mV	0.193
CCM-4	decal	0.5 h OCV + 1h 400 mV	0.269
CCM-8	decal	0.5 h OCV + 1h 200 mV	0.207
MEA_2610	spraying	0.5 h OCV + 1h 500 mV	0.436
MEA_2710	spraying	0.5 h OCV + 1h 400 mV	0.453

The arithmetic mean of migrated Ru of the decal cathode catalysts from the potential series is 0.223 wt% with a standard deviation of 0.041. The arithmetic mean of migrated Ru of the sprayed cathode catalysts is 0.445 wt% with a standard deviation of 0.012 wt%. Obviously the steady state cell potential during the first 90 min of operation does not influence the amount of migrated ruthenium considerably. In contrast, the influence of operation time is much more significant as will be shown in the following section.

4.4.3. Time series

The influence of time at certain conditions on the dissolution behavior has not been studied in detail yet. In this work in particular the time directly after fuel cell start and shortly thereafter is of interest. Evaluating the data taken from the samples operated at OCV for 0.5, 10.5 and 100.5 hours immediately a strong correlation of ruthenium transfer and operation time becomes obvious. In Table 14 the sample names, their DMFC history and the amount of ruthenium found on the cathode catalysts are listed. As has been shown above the cell potential did significantly not influence the amount of ruthenium transferred. Therefore the arithmetic mean of the potential series was added as another data point at 1.5 h to the table. This new data point fits well with the trend apparent from the OCV time series data even though these samples were operated for 1 h at potentials of 200 mV, 400 mV or 600 mV, respectively. This emphasizes the conclusion, made in the previous paragraph, that during early operation the cell potential does not affect the Ru migration.

Table 14: Ruthenium concentrations of decal MEA cathode samples run under OCV conditions for different operation times as determined by XRF.

sample	**preparation technique**	**description**	**Ru amount (wt%)**
CCM-6	decal	0.5 h OCV	0.137
CCM-7	decal	10.5 h OCV	0.389
CCM-5	decal	100.5 h OCV	0.534
mean of potential series	decal	0.5 h OCV + 1 h at different potentials	0.223

In Figure 53 an overview of the data plotted as graph is given. The black squares are data points of the time series samples. The red circle illustrates the arithmetic mean of the Ru concentrations of the potential series decal MEA samples.

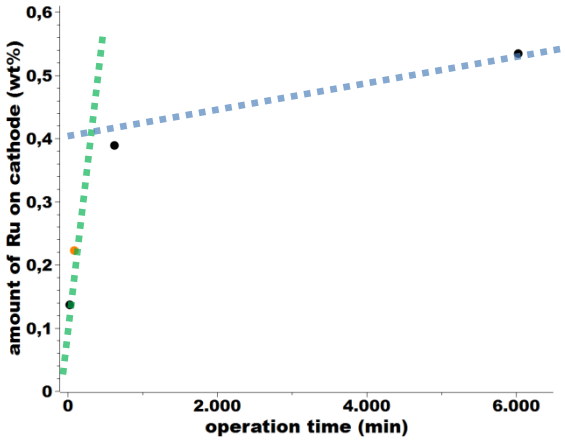

Figure 53: Ru concentrations in decal cathode catalyst samples (black) plotted against operation time at OCV. Additionally the mean amount of migrated Ru from the potential series is shown in orange. The two dotted lines illustrate the proposed fast (green) and slow (blue) dissolution processes.

The trend of ruthenium dissolution with time, as shown in Figure 53, can be explained in two ways: (1) as a saturation process where the amount of migrated Ru tends to a certain limit. This limit in turn could be defined either by the depletion of the source of soluble ruthenium or the maximum capacity for ruthenium of the cathode or the Nafion®, in which the migration takes place. (2) as a superposition of two independent dissolution processes with different rates and timescales. The first steep increase of migrated ruthenium within the first two hours of operation can be attributed to a fast dissolution process. Highly soluble ruthenium species are washed out of the anode catalyst and carried onto the cathode along with water and methanol permeation through the membrane. When this source of Ru is depleted, the second slower process becomes more evident. For this process, the Ru sources are harder to dissolve ruthenium species, probably even the platinum-ruthenium alloy phase.

4.4.4. Comparison of different anode feeds

The last parameter of cell operation tested within this work was the influence of different anode fuel feeds. Because methanol shows a higher permeation rate through Nafion® then e.g. ethanol a comparison of these two fuels seems interesting. Changing the ‘fuel’ might provide insight into the mechanisms involved in the dissolution and transport of ruthenium. Are the soluble ruthenium species at the anode especially susceptible to a specific solvent? Is the transport of Ru onto the cathode driven by diffusion or electromigration?

In Figure 54 an overview on the amount of transferred Ru during operation under OCV conditions for 0.5 hours for an anode feed of pure water, 1 M methanol and 1 M ethanol is shown.

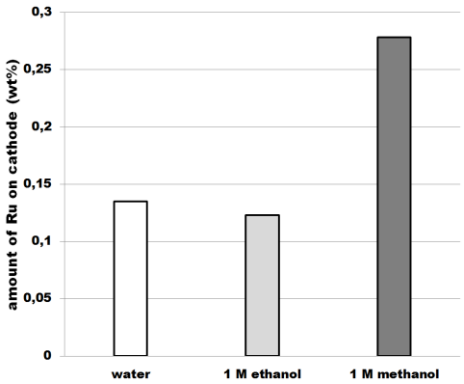

Figure 54: Ru concentrations of sprayed MEA cathode catalyst samples operated for 30 min at OCV using various anode fuel feeds.

While water and 1 M ethanol feeds show similar amounts of ruthenium transferred to the cathode catalyst, a 1 M methanol fed cell exhibits twice the Ru migration despite almost similar OCV values like the ethanol fed cell. The exact values of transferred Ru amounts are listed in Table 15.

Table 15: Ruthenium concentrations of sprayed MEA cathode samples run under OCV conditions with different anode fuel feeds.

sample	**description**	**Ru amount (wt%)**
MEA_1908	0.5 h OCV (78 mV), H_2O	0.135
MEA_1910	0.5 h OCV (750 mV), 1 M EtOH	0.123
MEA_2510	0.5 h OCV (770 mV), 1 M MeOH	0.278

There are a number of possible explanations:

- The involved Ru species dissolve better in 1 M methanol than in pure water or 1 M ethanol
- The ruthenium ions are transported through the membrane by water / methanol / ethanol crossover and methanol crossover is more pronounced than the other two

- One of the intermediates of oxidation or products of incomplete oxidation of methanol [46] are involved in the dissolution process[5]
- A combination of any of the aforementioned explanations

It would be of great benefit, if the species being dissolved during the fast dissolution process could be identified and monitored. The extremely low amounts of Ru in the ppm range make an identification of the exact ruthenium species in solution a challenge though.

Meanwhile the ICP-MS measurements presented in chapter 4.6 did not show any difference in the amount of ruthenium dissolved in pure water or 1 M methanol. However this ICP-MS leaching experiment was not done in a DMFC, so there might be a different process taking place. If the process would be the same though, the first explanation could be ruled out. The second explanation would have to be addressed in a repetition of the fuel experiment facilitating MEAs with a different membrane. If a membrane with a lower permeability for methanol was used the results could be compared with the findings for Nafion®. As has been mentioned before a side reaction of methanol oxidation can lead to the formation of formic acid. The ICP-MS measurement showed that 1 M formic acid is capable of dissolving large amounts of ruthenium. Totsuka [47] showed that under OCV conditions about $0.2 \cdot 10^{-9}$ mol/l could be found in the anode effluent. This is a very low concentration, but the formic acid still might be responsible for the two times higher amount of ruthenium on the cathode run with a methanol feed compared to water or ethanol. A future experiment could probe if an addition of formic acid to the water or 1 M ethanol fuel feed can dissolve the same quantities of Ru.

The second question presented at the beginning of this section concerned the driving force of the migration. Since the cell reached about the same open cell potential fed with 1 M ethanol as with 1 M methanol (see Table 15) electromigration as main driving force does not seem plausible. Instead the differences in permeability of Nafion® for methanol and ethanol or water should be further investigated in regard to ruthenium migration.

4.5. Cyclic voltammetry

As has been pointed out, cyclic voltammetry is a highly sensitive electrochemical technique, which has been used by several researchers to detect changes in the DMFC cathode catalysts [11], [19], [20], [66], [121]. Even though complementary analyses are needed [22] to link the observed changes to ruthenium crossover, CV is a versatile tool for qualitative measurements.

The catalyst powders had to be scratched from the membrane and re-applied to a glassy carbon electrode for measurements in a 3-electrode set-up in aqueous electrolyte. Only 4 of 8 anode and 5 of 8 cathode samples could be measured successfully, while all other samples could not

[5] Even under OCV conditions some methanol oxidation or other reactions can occur.

form an interface with the electrolyte but stayed insulated by a thin air layer. This was probably due to the high hydrophobicity of the decal cathode catalyst samples. Although the addition of Teflon® (as part of the recipes of the inks used for MEA fabrication) explains this hydrophobic behavior, such an extreme hydrophobicity was not experienced with samples used in other experiments.

The voltammograms for the HiSpec 13100 pure Pt catalyst in 0.1 M perchloric acid (blue curve) and in 0.1 M perchloric acid with 1 M methanol added (red curve) as electrolytes are shown in Figure 55. This catalyst was measured as a reference sample to obtain a reliable picture of a pure platinum catalyst for the electrooxidation of methanol.

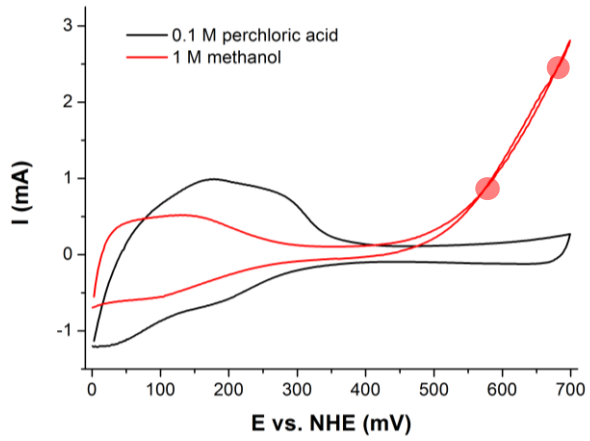

Figure 55: Cyclic voltammograms (not normalized) of the HiSpec 13100 pure platinum on carbon catalyst in 0.1 M perchloric acid and in 1 M methanol. The highlights mark the intersects in the voltammogram in 1 M methanol.

As has been described in chapter 3.5.6, the upper potential limit was set to 700 mV vs. NHE to avoid electrochemical dissolution of ruthenium [8]. To quantify the catalytic activity for methanol oxidation of a catalyst usually the onset potential of the oxidation peak and the peak height are used. But because of the chosen upper potential limit of 700 mV vs. NHE, the methanol oxidation feature is not completely included in the CVs. Only the first part of the feature, i.e. the onset of the oxidation peak, is visible. There is one other feature though that can be used to qualitatively compare the catalysts, the intersects of the forward and backward sweep. During the anodic sweep the surface is 'clean' till the onset of methanol oxidation, where methanol and the reaction products start to cover the surface. During the cathodic sweep the surface is already covered with intermediates, byproducts and products, most importantly carbon monoxide. This changes the kinetics of the reaction and leads to a different shape of the voltammogram and hence to intersects of the forward and backward curve. The intersects are correlated with the Ru content, as the ruthenium acts as a co-catalyst to oxidize CO (see chapter

2.1). In contrast platinum-ruthenium alloy catalysts show a different behavior. An example for the HiSpec 12100 PtRu anode catalyst is given in Figure 56.

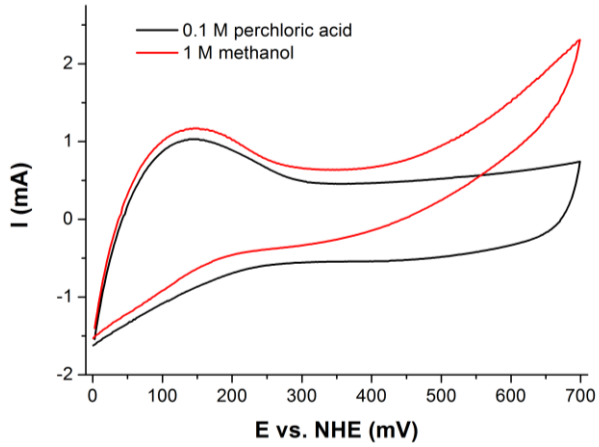

Figure 56: Cyclic voltammograms (not normalized) of the HiSpec 12100 platinum-ruthenium on carbon catalyst in 0.1 M perchloric acid and in 1 M methanol.

Already the voltammogram in 0.1 M perchloric acid is different from the pure platinum catalyst. The double-layer capacity is very pronounced. This can be attributed to the presence of ruthenium oxide in the PtRu catalyst [122]. Conway et al. [123], [124] have described the mechanisms behind this redox pseudocapacity in more detail. Compared to the platinum catalyst the voltammogram of the PtRu catalyst in 1 M methanol does not show any intersects. This is to be explained by the presence of ruthenium. As has been described in chapter 2.1, the bifunctional mechanism enabled by the ruthenium cocatalyst helps to oxidize the CO adsorbates on the platinum surface. This in turn changes the ratio of intermediates on the catalyst surface and the electrochemical response of the system.

Of the decal MEA cathode catalyst samples, which could be measured in CV, three with different amounts of migrated ruthenium, as has been quantified by XRF, are shown in Figure 57.

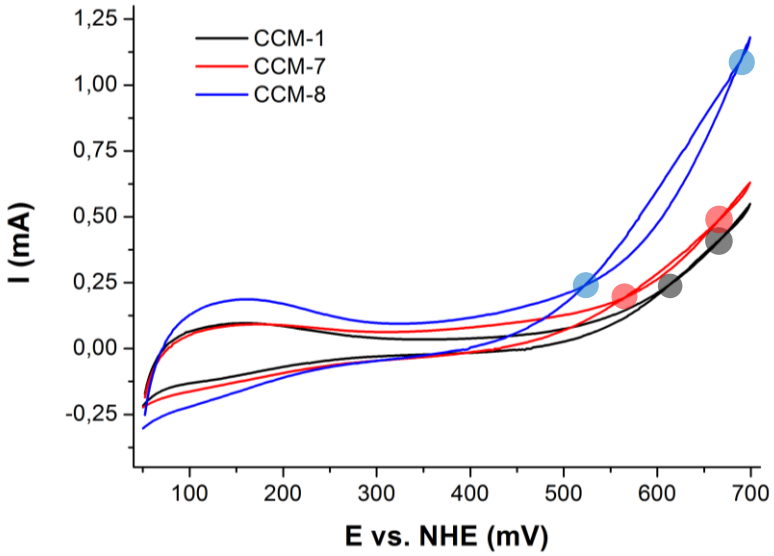

Figure 57: Cyclic voltammograms (not normalized) of different cathode catalysts in 1 M MeOH. The highlights mark the intersects in the voltammograms.

Even the low Ru amounts in the 0.024 – 0.389 wt% range of these samples led to a severe effect on the catalytic behavior, especially for methanol oxidation. The following table lists the intersects, the difference between the intersects and the amount of ruthenium as determined by XRF.

Table 16: Correlation of CV measurements of decal MEA cathode catalyst and their ruthenium content.

sample	**description**	**1. intersect**	**2. intersect**	**intersect difference**	**Ru content**
CCM-1	as-prepared	614 mV	669 mV	55 mV	0.024 wt%
CCM-7	10.5 h OCV	563 mV	664 mV	101 mV	0.389 wt%
CCM-8	0.5 h OCV + 1 h 200 mV	522 mV	689 mV	167 mV	0.207 wt%
HiSpec 13100	Pt catalyst as-received	568 mV	679 mV	111 mV	(0.001 wt%)

Comparing the two samples subjected to DMFC conditions to the as-prepared sample, there seems to be a correlation of crossover difference and Ru content. For both samples run in a DMFC the crossover difference is significantly larger than for the as-prepared sample. However, the relative change in crossover differences does not correspond directly to the ruthenium amount. The sample CCM-7 contains about 0.18 wt% more ruthenium, but shows an almost 70 mV smaller intersect difference.

The pure HiSpec 13100 cathode catalyst also exhibits a comparably large crossover difference, even though its ruthenium content is very low. The fact that the crossover difference is so large compared to the as-prepared decal MEA sample can be explained by the fundamental difference of the samples. The decal MEA samples were scratched off the MEA and contain Nafion® and Teflon®, while only Nafion® was added to the ink for preparing the CV electrode from the HiSpec catalyst. The comparison of cyclic voltammetry results like the ones presented here is only valid for samples of similar composition. And while it is not possible to quantify the Ru content by means of CV, the high sensitivity of CV clearly makes it a good probe for changes in the catalysts composition.

4.6. Inductively coupled plasma mass spectrometry

Since it was not fully clear if the baseline value of 0.012 wt% ruthenium in the XRF measurements (see chapter 3.5.1) is only due to errors in pile-up correction and data fitting, the as-received HiSpec 13100 platinum catalyst was subjected to a thorough analysis by ICP-MS. Two samples of the as-received catalyst powder were independently chemically dissolved and analyzed (see also chapter 3.5.3). Both measurements resulted in a ruthenium content of ca. 0.001 wt% of the HiSpec 13100. So, only 10 % of the XRF baseline value can be caused by actual ruthenium impurities. The rest has to be attributed to the aforementioned errors.

4.6.1. Ruthenium dissolution during DMFC operation

In order to verify the results of the XRF analyses ICP-MS was chosen as complementary technique. Because only the decal MEA samples cover a time and a potential series, only these were measured again by ICP-MS. In Table 17 the results of the ICP-MS analysis as well as the XRF results for comparison are listed.

Table 17: Ruthenium concentrations of decal MEA cathode samples run under OCV conditions for different operation times as determined by XRF and ICP-MS.

sample	description	Ru amount (wt%) determined by	
		XRF	ICP-MS
CCM-1	as-prepared	0.023	0.016
CCM-2	as-prepared	0.026	0.015
CCM-6	0.5 h OCV	0.137	0.072
CCM-7	10.5 h OCV	0.389	0.239
CCM-5	100.5 h OCV	0.534	0.269
CCM-3	0.5 h OCV + 1h 600 mV	0.193	0.118
CCM-4	0.5 h OCV + 1h 400 mV	0.269	0.169
CCM-8	0.5 h OCV + 1h 200 mV	0.207	0.169
mean of potential series	0.5 h OCV + 1 h at different potentials	0.223	0.152

It is obvious, that all values measured by ICP-MS lie below the ones measured by XRF, even if the XRF baseline of 0.012 wt% is considered. The reason for this discrepancy is not clear. Since both techniques suffer from artifacts, it is not clear, which values are the more accurate ones. For the ICP-MS measurements the samples had to be chemically disintegrated. This process could have been incomplete, i.e. either not all ruthenium was dissolved, or the solution was not stable and ruthenium might have precipitated resulting in smaller values. In contrast, the XRF measurement could have overestimated the amount of ruthenium due to uncorrected pile-up artifacts from platinum M-line fluorescence photons.

Anyhow, the correlation of ruthenium dissolution and operation time is visible in both datasets and follows the same trend. In Figure 58 the time series and average of the potential series versus operation time is plotted for both analysis methods.

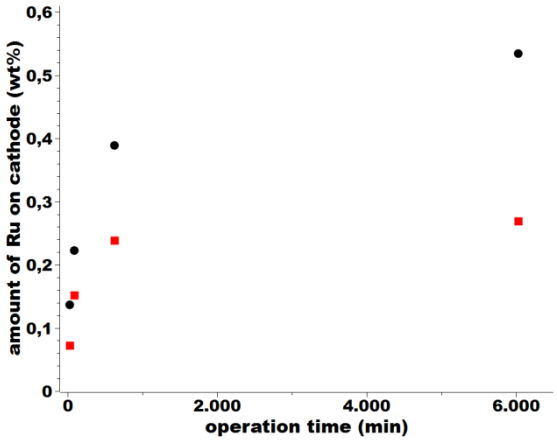

Figure 58: Ru concentrations in decal cathode catalyst samples plotted against operation time at OCV. The black data points represent the measurements done using XRF, the red data points are the results of the ICP-MS analysis.

4.6.2. Influence of solvents

Leaching test of the HiSpec 12100 platinum-ruthenium catalyst in three different media, namely pure water, 1M methanol and 1 M formic acid, were performed to get more insight into the ruthenium dissolution mechanism. Of special interest was the behavior of the catalyst being exposed to the formic acid as one of the possible products of side reactions of the MOR [46], [47]. The results of the ICP-MS measurements are given in Table 18.

Table 18: Results of ICP-MS analyses of the supernatants from leaching experiments of PtRu catalysts in different solvents.

solvent	**platinum in solution**	**ruthenium in solution**
pure water	0.00 ppm	0.01 ppm
1 M methanol	0.00 ppm	0.01 ppm
1 M formic acid	0.23 ppm	0.96 ppm

The detection limits of the ICP-MS for platinum and ruthenium were about 0.1 ppb. While platinum is stable against dissolution in water and 1 M methanol, ruthenium is dissolved, but only very low amounts. In contrast, formic acid is capable of dissolving significant amounts of platinum and ruthenium. Of course the 1 M concentration of formic acid used in this experiment is very high compared to the production inside a DMFC. Data on the amounts of formic acid present in a DMFC during operation are given by Totsuka [46], [47]. He showed, that at OCV about 0.1 µM of formic acid could be found in the anode effluent of a 25 cm^2 direct methanol single cell, operated at 80 °C with feeds of 5 ml/min of 1 M methanol and 260 ml/min oxygen. The formation of formic acid increased with increasing cell current and reached ca. 15 µM/min

at 600 mA/cm², corresponding approximately to a cell voltage of 200 mV. Interestingly, up to 0.35 µM/min formic acid could also be detected in the cathode effluent. This provides evidence that either a formic acid crossover exists or that crossover methanol from the anode is converted to formic acid at the cathode.

The leaching experiments were conducted at room temperature and without any potential. Therefore the results cannot be directly transferred to reactions and mechanisms taking place inside a DMFC. Nonetheless there is evidence that formic acid plays an important role in the dissolution of ruthenium. Probably formic acid is part of the slower ongoing dissolution process found in the XRF measurements (see chapter 4.4.4).

5. Discussion

After presenting the results of this work in the previous chapter according to the measurement techniques used, these will now be discussed with respect to the various processes occurring during operation. At first, the origin of the mobile Ru species will be discussed in the light of the detailed characterization of the different anodes by XRD, XPS and XAS. Then, the transfer mechanism of Ru species through the membrane will be highlighted. Finally, the amount and kind of Ru species deposited on the cathode side depending on the operation conditions will be discussed as followed by the detailed characterization of the different cathodes using mainly XAS, XRF and ICP-MS.

Origin of the mobile Ru species

The pristine and used anodes were analyzed using XRD and XPS. XRD picks up only on the crystalline fraction of the sample and XPS can distinguish the Pt and Ru oxidation states present in the sample. Only a Pt fcc phase shifted to smaller 2 theta values by incorporation of the smaller-sized Ru according to Vegard's law was observed with particle sizes of about 2 nm. The operation conditions neither changed the crystalline sample part, nor the particle size significantly.

XAS and XPS both reveal an oxidic ruthenium phase besides the platinum-ruthenium alloy phase. As this phase does not show up in the powder patterns, it has to be amorphous. It is most likely, that this phase is the source of most of the Ru dissolved and transferred through the membrane onto the cathode side. However, this cannot be shown unambiguously, since the catalyst composition seems to return to a "balanced composition" of metallic and oxidic ruthenium, whenever the catalyst is brought into contact with air atmosphere. Since a vacuum transfer of the sample after operation in the fuel cell directly into the XPS chamber was not feasible, this assumption cannot be verified.

Ru transfer through the membrane

Still, it is not clear, how the less stable Ru species are leached from the anode catalyst and transferred through the membrane to the cathode. During operation, water, methanol and formic acid are present in the anode, where water and methanol are the fuel, whereas formic acid is an intermediate of an unwanted side reaction. It is reported that depending on the exact operation conditions, up to 15 µM formic acid are present in the anode effluent. Furthermore, the anode is subjected to a potential, also possibly driving dissolution.

To distinguish between the different possible mechanisms, at first dissolution tests without any potential were conducted and the amount of dissolved Ru in water, methanol and formic acid detected by ICP-MS. Formic acid appears to be the most harmful, and should therefore be reduced by reasonable DMFC conditions. XPS analysis of the solid residues did not show

differences in composition, most probably because of the same reasons as discussed above. Either the changes were not significant enough to be picked up by XPS, or the sample composition returns to a stable composition upon contact with air atmosphere.

In a subsequent step, two fuel cells, one supplied with methanol, the other with ethanol, were operated at OCV conditions and after operation the cathode catalysts were compared. During operation with ethanol in contrast to methanol fuel cell operation, significantly lower amounts of Ru were found on the cathode. Obviously, also methanol cross-over is stronger than ethanol cross-over and drags Ru species from the anode to the cathode side.

Ru deposition on the cathode

The amount and kind of ruthenium, which is deposited on the plain carbon-supported Pt cathode was observed by XRD and XAS. Both techniques give structural information on various crystalline phases and/or oxidation state of the Ru species deposited. A quantitative result depending on operation conditions, however, cannot be given. For quantification, XRF and ICP-MS were applied and the results compared, also considering the errors and different artifacts characteristic to these techniques (see below).

X-ray diffraction patterns of all cathodes only exhibit the Pt fcc phase and do not show any changes in comparison. Either the ruthenium species on the cathode is crystalline and the amount is too low to be detected by XRD, or the Ru species deposited on the cathode side is amorphous. XAS measurements at the Ru K-edge confirm that a mostly oxidic ruthenium species is present at the cathode catalysts, which could be "fingerprinted" against two reference compounds. I conclude that the nature of the deposited Ru species has to be oxidic and amorphous.

Quantification of the Ru deposition

The quantification of the amount of Ru species transferred within the early operation hours of a single cell DMFC appeared to be rather tricky, since ppm amounts had to be detected, which is demanding for the analysis methods and the thoroughness of the sample preparation. With XRF and ICP-MS both a chemical and a physico-chemical method were applied with the limitations this brings about. While in ICP-MS errors can arise from the chemical dissolution of the sample and the calibration standards, XRF suffers from artefacts, as not only Ru but also a high amount of Pt is present in the samples. However, although the absolute values obtained from XRF and ICP-MS were different, the relative trends of the XRF could be reproduced by ICP-MS and thus verified.

Already the as-received carbon-supported Pt catalyst used at the cathode side contains 0.001 wt% Ru. During MEA fabrication, another 0.023 wt% Ru is transferred regardless of the MEA fabrication procedure. However, during operation the MEAs produced by wet spraying exhibit

different ruthenium crossover amounts than ones produced by the dry decal method. After being operated for 30 min at OCV and consecutively for 60 min at a fixed cell potential, the MEAs prepared by wet spraying show about 0.2 wt% higher amounts of Ru on the cathode than the decal MEAs subjected to the same DMFC conditions. It might be, that during wet spraying the migration of Ru already starts but does not reach the cathode side before the solvents have evaporated. During cell operation this already half-way migrated ruthenium would lead to an increase of transferred Ru during early operation. Also the higher temperatures during the hot-pressing step of decal fabrication could influence the dissolution behavior by partially transforming ruthenium hydroxide species to more resilient oxides.

During early operation, the cell potential seems to exert only a minor influence on the dissolution process, whereas the operation time appears to be more crucial. After 2h under open circuit conditions about 0.25 wt% ruthenium could be observed on the cathode, whereas 0.3 wt% more were added over the course of 100 h. Showing the detected amount of Ru with time (see Figure 58), a peculiar trend can be revealed, which may be explained as follows: (1) as a saturation process where the amount of migrated Ru tends to a certain limit. This limit in turn could be defined either by the depletion of the source of soluble ruthenium or the maximum capacity for ruthenium of the cathode or the Nafion®, in which the migration takes place. (2) as a superposition of two independent dissolution processes with different rates and timescales. The steep increase of migrated ruthenium within the first two hours of operation could be attributed to a fast dissolution process. First, highly soluble ruthenium species are washed out of the anode catalyst and carried onto the cathode along with water and methanol permeation through the membrane. When this source of Ru is depleted, the second slower process becomes more evident. The source of Ru for the slower process might by harder to dissolve (anhydrous) oxides or ruthenium leached out from the platinum-ruthenium alloy phase.
In my opinion the later explanation is more probable. First, the XPS measurements of the anode catalysts do not show any considerable consumption of a ruthenium phase. Second, a similar twofold dissolution mechanism was also proposed by Liu et al. [24], though their experiments on model systems were performed for much longer time periods. They showed a “serious Ru migration” in the first 200 h of operation which was “especially [pronounced] in the period 0-28 h”. In favor of the second explanation is also the presence of several ruthenium phases in the anode [26], [29]–[31] and the observed differences in dissolution behavior [45].

Most published results on ruthenium dissolution show ongoing catalyst degradation and ruthenium migration over the whole DMFC operation time. It has to be mentioned though, that usually dynamic load profiles are applied to the fuel cells. This could lead to further, different dissolution mechanisms than the ones observed in this work under static potential conditions. But again the changes in alloy composition observed by other groups imply, that with longer operation times the anode catalyst is slowly altered, supporting the second explanation as well.

6. Conclusion & Outlook

The phenomenon of ruthenium dissolution in DMFCs seems to be influenced by different mechanisms. Only detailed single cell studies, like in this work, have a chance to distinguish between them. A DMFC stack study has the advantage, that much larger quantities of ruthenium are being dissolved, transferred and redeposited, but at the cost of the microscopic view into the processes involved. Single cell experiments on the other hand need to cope with the trace analysis needed to measure the Ru dissolution on this smaller scale. Many common analytical techniques are not capable of detecting changes in the ppm range, this includes XRD and XPS. The measurement techniques, which are applicable though, are XRF, XAS and CV.

The two most remarkable findings of this work are 1) that ruthenium dissolution already occurs during fabrication of the MEA and that 2) during the early operation time of a DMFC a relatively fast dissolution process transfers a significant amount of Ru onto the cathode catalyst. Therefore, most experiments will not start with a clean cathode to begin with and during break-in of the DMFC the Ru content of the cathode is further increased. This may be an explanation for the commonly observed initial performance drop and consequent stabilization of cell performance during cell break-in. A simplified illustration of ruthenium migration is shown in Figure 59.

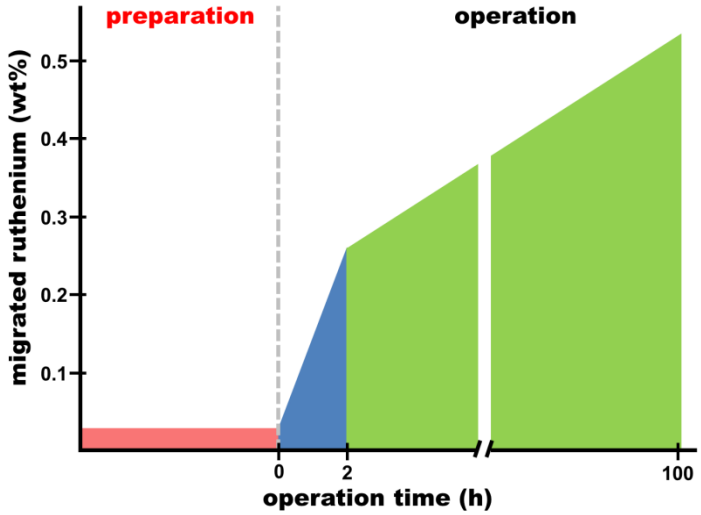

Figure 59: Illustration of the amount of ruthenium found on the cathode of a DMFC vs. time. The colors represent the different processes: transfer during preparation (red), fast dissolution at start-up (blue), slow dissolution during further operation (green).

The fast dissolution process, probably fed by highly soluble Ru species in the anode catalyst, transferred about 0.25 wt% of ruthenium onto the cathode catalyst within the first two hours of operation. A slower dissolution process led to an additional transfer of about 0.3 wt% Ru over

the period of 2 - 100 h of DMFC operation. The evidence of two dissolution processes is in good agreement with the findings of Piela [11] and Liu [24].

XRD analysis did not show any changes in the crystallite structure of the anode catalyst, so the slower process might dissolve amorphous ruthenium oxides. As leaching experiments using formic acid suggest, there could be a relation between the production of formic acid, a product of incomplete methanol oxidation, and Ru dissolution. Totsuka [46], [47] has shown that during all operation modes of a DMFC formic acid is produced and could be detected in the effluents of anode and cathode. Besides ruthenium, also platinum can be attacked and dissolved by formic acid. XAS experiments relying on the assumption that the overall platinum content does not change during the measurements should check with a complementary technique that the influence of Pt dissolution is actually negligible. A design goal for further catalyst development could be to reduce the production of formic acid. But also the already available catalysts can benefit from these findings, as a preleaching of the anode catalyst using formic acid could easily remove soluble Ru species prior to fabrication of the MEA.

Even though the amounts of dissolved Ru are low, it is interesting that no changes whatsoever could be detected in the anode catalyst composition using XPS. Probably the catalyst always returns to a stable composition when dried and exposed to air. If this is the case, ex-situ measurements are not the appropriate approach to find the Ru species susceptible to dissolution.

Further experiments should assess the effectiveness of anode catalyst preleaching and address the influence of potential changes / cycling of the fuel cell. Other interesting parameters are the methanol concentration in the fuel feed and the fuel cell temperature, both also affecting the production of formic acid. Also the influence of methanol crossover on the migration of ruthenium should be investigated. If the ruthenium is transported by the methanol, membranes currently developed to reduce the methanol permeation (e.g. sPEEAN [125] or sPEAK [126]) will consequently decrease the ruthenium crossover.

7. Acknowledgments

My special thanks go to Prof. Dr. Christina Roth and Prof. Dr. Wolfgang Ensinger for their efforts to act as referees for this work. I am grateful to Prof. Roth for the opportunity to join her group and the Canadian German project „Kanadisch-Deutsche Brennstoffzellenkooperation - Verbesserung der Leistung und Alterungsstabilität von Direktmethanol-Brennstoffzellen der kW-Klasse“. For our fruitful collaboration and all the helpful discussions I thank my project partners at Forschungszentrum Jülich, Fraunhofer Institut für Solare Energiesysteme Freiburg and the Institute for Chemical Process and Environmental Technology of the National Research Council Canada. And I thank the German Federal Ministry of Economy for their financial support of the aforementioned project.

For their help with and advice on measurements, data analysis and interpretation I thank David Batchelor (XRF), Renate Benz (ICP-OES), Manuela Borchert (XRF), Michael Bruns (XPS), Matthias Herrmann (XAS), Jean Christophe Jaud (XRD), Ulrike Kunz (SEM), Sebastian Kaserer (CV), Frank Kuppler (ICP-MS), Micheal Murphy (XAS), Dominic Stürmer (XRD), Adam Webb (XAS), Andre Weidner (XRD) and Edmund Welter (XAS).

My sincere thanks go also to my working group members at Technische Universität Darmstadt, Karlsruher Institut für Technologie, Freie Universität Berlin and all alumni for their support in the laboratory and our memorable barbecues.

Last but not least I want to express my deep gratitude to my family and friends for their constant backup throughout the whole process of the PhD. Especially for enduring my moaning!

8. Appendix

Example FullProf config file

```
COMM Pt auf C
! Current global Chi2 (Bragg contrib.) =      10.9381
! Files => DAT-file: ccm-1k.dat,  PCR-file: ccm-1k

!Job Npr Nph Nba Nex Nsc Nor Dum Iwg Ilo Ias Res Ste Nre Cry Uni Cor Opt Aut
   0   7   1   8   2   0   0   0   0   2   0   0   0   0   0   0   0   0   0
!
!Ipr Ppl Ioc Mat Pcr Ls1 Ls2 Ls3 NLI Prf Ins Rpa Sym Hkl Fou Sho Ana
   0   0   1   0   1   0   4   0   0  -3  10   0   1   0   0   1   0
!
! Lambda1  Lambda2    Ratio     Bkpos     Wdt     Cthm      muR    AsyLim   Rpolarz  2nd-muR -> Patt# 1
 0.709233 0.709233   1.00000    30.000 20.0000   0.9534   0.0100    90.00    0.5000   0.0000
!
!NCY  Eps  R_at  R_an  R_pr  R_gl      Thmin        Step        Thmax     PSD     Sent0
  5  0.10  1.00  1.00  1.00  1.00       5.0600    0.010003     59.9900    0.000    0.000
!
!2Theta/TOF/E(Kev)   Background  for Pattern#  1
        11.2263         485.2610          31.00
        14.4535         371.5505          41.00
        23.2745         306.0865          51.00
        27.0396         298.3623          61.00
        39.6794         292.4666          71.00
        44.5202         303.5279          81.00
        50.8133         293.2142          91.00
        58.7737         321.7436         101.00
!
! Excluded regions (LowT  HighT) for Pattern#  1
        5.00        11.00
       59.00       180.00
!
!
      12    !Number of refined parameters
!
!  Zero    Code    SyCos    Code   SySin    Code  Lambda     Code MORE ->Patt# 1
 -0.00582   21.0  0.00000     0.0  0.00000     0.0 0.709233    0.00    0
!-------------------------------------------------------------------------------
!  Data for PHASE number:   1  ==> Current R_Bragg for Pattern#  1:     2.44
!-------------------------------------------------------------------------------
Pt
!
!Nat Dis Ang Pr1 Pr2 Pr3 Jbt Irf Isy Str Furth       ATZ     Nvk Npr More
   1   0   0 0.0 0.0 1.0   0   0   0   0   0        780.110   0   7   0
!
F m -3 m                  <--Space group symbol
!Atom   Typ       X         Y         Z      Biso       Occ      In Fin N_t Spc /Codes
Pt1    Pt      0.00000   0.00000   0.00000   0.00000    0.02083   0   0   0     0
                  0.00      0.00      0.00      0.00       0.00
!-------> Profile Parameters for Pattern #  1
```

```
!  Scale         Shape1       Bov       Str1       Str2       Str3    Strain-Model
 0.10582E-03    0.00000    0.00000    0.00000    0.00000    0.00000        0
     11.00000       0.000    0.000       0.000       0.000       0.000
!        U           V           W           X           Y         GauSiz    LorSiz Size-Model
    0.060170   -0.003621    0.008223    0.000000    0.773289    0.000000    0.000000     0
        0.000       0.000       0.000       0.000     111.000       0.000       0.000
!      a           b           c         alpha       beta        gamma       #Cell Info
    3.915517    3.915517    3.915517   90.000000   90.000000   90.000000
   121.00000   121.00000   121.00000    0.00000     0.00000     0.00000
!   Pref1     Pref2       Asy1      Asy2      Asy3      Asy4       S_L       D_L
   0.00000   0.00000   0.00000   0.00000   0.00000   0.00000   0.02150   0.02150
      0.00      0.00      0.00      0.00      0.00      0.00      0.00      0.00
!   2Th1/TOF1     2Th2/TOF2   Pattern # 1
       19.500       39.500        1
```

Example PyMca config file

```
[attenuators]
absorber = 0, -, 0.0, 0.0, 1.0
Co = 1, Co, 8.9, 0.002, 1.0
Matrix = 0, MULTILAYER, 0.0, 0.0, 45.0, 45.0, 0, 90.0
BeamFilter1 = 0, -, 0.0, 0.0, 1.0
window = 0, -, 0.0, 0.0, 1.0
BeamFilter0 = 0, -, 0.0, 0.0, 1.0
contact = 0, Au1, 19.37, 1e-06, 1.0
Ti = 1, Ti, 4.54, 0.0015, 1.0
Filter 6 = 0, -, 0.0, 0.0, 1.0
Filter 7 = 0, -, 0.0, 0.0, 1.0
Detector = 0, Si1, 2.33, 0.5, 1.0
Cu = 1, Cu, 8.94, 0.004, 1.0

[peaks]
Ru = Ka, Kb
Co = Ka, Kb
Pt = L, L1, L2, L3
Fe = Ka, Kb
Pd = Ka, Kb
Ti = Ka, Kb
Cu = Ka, Kb

[fit]
stripwidth = 1
linearfitflag = 0
xmin = 0
scatterflag = 1
snipwidth = 30
stripfilterwidth = 1
escapeflag = 1
exppolorder = 6
fitweight = 1
stripflag = 1
```

```
stripanchorsflag = 0
use_limit = 1
maxiter = 10
stripiterations = 20000
continuum_name = None
sumflag = 1
linpolorder = 5
stripalgorithm = 0
deltaonepeak = 0.01
deltachi = 0.001
continuum = 0
hypermetflag = 1
stripconstant = 1.0
xmax = 3000
fitfunction = 0
energy = 26.0
stripanchorslist = 0, 0, 0, 0
energyscatter = 1
energyweight = 1.0
energyflag = 1

[multilayer]
Layer3 = 0, -, 0.0, 0.0
Layer2 = 0, -, 0.0, 0.0
Layer1 = 0, -, 0.0, 0.0
Layer0 = 0, -, 0.0, 0.0
Layer7 = 0, -, 0.0, 0.0
Layer6 = 0, -, 0.0, 0.0
Layer5 = 0, -, 0.0, 0.0
Layer4 = 0, -, 0.0, 0.0
Layer9 = 0, -, 0.0, 0.0
Layer8 = 0, -, 0.0, 0.0

[tube]
windowdensity = 1.848
anodedensity = 10.5
windowthickness = 0.0125
anodethickness = 0.0002
transmission = 0
alphax = 90.0
deltaplotting = 0.1
window = Be
filter1thickness = 0.0
anode = Ag
voltage = 30.0
filter1density = 0.000118
alphae = 90.0
filter1 = He

[materials]

[materials.Kapton]
Comment = Kapton 100 HN 25 micron density=1.42 g/cm3
Density = 1.42
```

```
Thickness = 0.0025
CompoundFraction = 0.628772, 0.066659, 0.304569
CompoundList = C1, N1, O1

[materials.Teflon]
Comment = Teflon density=2.2 g/cm3
Density = 2.2
CompoundFraction = 0.240183, 0.759817
CompoundList = C1, F1

[materials.Gold]
Comment = Gold
CompoundFraction = 1.0
CompoundList = Au
Thickness = 1e-06
Density = 19.37

[materials.Air]
Comment = Dry Air (Near sea level) density=0.001204790 g/cm3
Density = 0.0012048
Thickness = 1.0
CompoundFraction = 0.000124, 0.75527, 0.23178, 0.012827, 3.2e-06
CompoundList = C1, N1, O1, Ar1, Kr1

[materials.Water]
Comment = Water density=1.0 g/cm3
CompoundFraction = 1.0
CompoundList = H2O1
Density = 1.0

[materials.Viton]
Comment = Viton Fluoroelastomer density=1.8 g/cm3
Density = 1.8
CompoundFraction = 0.009417, 0.280555, 0.710028
CompoundList = H1, C1, F1

[materials.Goethite]
Comment = Mineral FeO(OH) density from 3.3 to 4.3 density=4.3 g/cm3
CompoundFraction = 1.0
Density = 4.3
Thickness = 0.1
CompoundList = Fe1O2H1

[materials.Mylar]
Comment = Mylar (Polyethylene Terephthalate) density=1.40 g/cm3
Density = 1.4
CompoundFraction = 0.041959, 0.625017, 0.333025
CompoundList = H1, C1, O1

[concentrations]
usemultilayersecondary = 0
reference = Auto
area = 30.0
flux = 10000000000.0
```

time = 1.0
useattenuators = 1
usematrix = 1
mmolarflag = 0
distance = 10.0

[detector]
detene = 1.742
noise = 0.1
fixednoise = 0
fixedgain = 0
deltafano = 0.114
ithreshold = 1e-07
sum = 1e-08
deltasum = 1e-08
deltazero = 0.1

fano = 0.114
fixedsum = 0
fixedzero = 0
zero = 0.00201818181819

deltagain = 0.001
ethreshold = 0.02
fixedfano = 0
deltanoise = 0.05
detele = Si
nthreshold = 4
gain = 0.00999752066116

[peakshape]
lt_arearatio = 0.02
fixedlt_arearatio = 0
fixedeta_factor = 0
st_arearatio = 0.05
deltalt_arearatio = 0.015
deltaeta_factor = 0.02
deltalt_sloperatio = 7.0
deltastep_heightratio = 5e-05
st_sloperatio = 0.5
lt_sloperatio = 10.0
fixedlt_sloperatio = 0
deltast_arearatio = 0.03
eta_factor = 0.02
fixedst_sloperatio = 0
fixedst_arearatio = 0
deltast_sloperatio = 0.49
step_heightratio = 0.0001
fixedstep_heightratio = 0

Example control macro for sample changer (XRF)

```
{
umv x -4.2
umv y 11.85
umv z -12.53
umv phi -45

loopscan 5 1

umv y -3.15
umvr z -1
umv x -4.1
loopscan 5 20

umvr z 1
loopscan 5 20

umvr z 1
loopscan 5 20
umvr z -1

umvr z 24
umvr z -1
umv x -3.9
loopscan 5 20

umvr z 1
loopscan 5 20

umvr z 1
loopscan 5 20
umvr z -1

umv 11.85
umv z -12.53
umvt phi -45

loopscan 5 1

[…]
}
```

List of figures

List of tables

List of abbreviations

CV	Cyclic Voltammetry
DAFC	Direct Alcohol Fuel Cell
DMFC	Direct Methanol Fuel Cell
EDX	Energy Dispersive X-ray analysis
EtOH	Ethanol
EXAFS	Extended X-ray Absorption Fine Structure
FC	Fuel Cell
ICP-MS	Inductively Coupled Plasma – Mass Spectrometry
MDL	Minimum Detection Limit
MEA	Membrane Electrode Assembly
MeOH	Methanol
MOR	Methanol Oxidation Reaction
NAA	Neutron Activation Analysis
ORR	Oxygen Reduction Reaction
PEMFC	Polymer Electrolyte Membrane Fuel Cell
SEM	Scanning Electron Microscopy
TEM	Transmission Electron Microscopy
XANES	X-ray Absorption Near Edge Structure
XAS	X-ray Absorption Spectroscopy
XPS	X-ray Photoelectron Spectroscopy
XRD	X-Ray Diffraction
(syn)XRF	(synchrotron) X-ray Fluorescence Spectroscopy

References

[1] "Multi-Year Research, Development and Demonstration Plan." U.S. Department of Energy's (DOE's) Office of Energy Efficiency and Renewable Energy (EERE), Jul-2013.

[2] M. Watanabe and S. Motoo, "Electrocatalysis by ad-atoms," *J. Electroanal. Chem. Interfacial Electrochem.*, vol. 60, no. 3, pp. 275–283, Apr. 1975.

[3] S. Wasmus and A. Küver, "Methanol oxidation and direct methanol fuel cells: a selective review," *J. Electroanal. Chem.*, vol. 461, no. 1–2, pp. 14–31, Jan. 1999.

[4] Y. Guo, D. Zheng, H. Liu, A. Friedrich, and J. Garche, "Investigations of Bifunctional Mechanism in Methanol Oxidation on Carbon-Supported Pt and Pt-Ru Catalysts," *J. New Mater. Electrochem. Syst.*, vol. 9, no. 1, pp. 33–39, 2006.

[5] T. Iwasita, H. Hoster, A. John-Anacker, W. F. Lin, and W. Vielstich, "Methanol Oxidation on PtRu Electrodes. Influence of Surface Structure and Pt−Ru Atom Distribution," *Langmuir*, vol. 16, no. 2, pp. 522–529, Jan. 2000.

[6] F. Buatier de Mongeot, M. Scherer, B. Gleich, E. Kopatzki, and R. . Behm, "CO adsorption and oxidation on bimetallic Pt/Ru(0001) surfaces – a combined STM and TPD/TPR study," *Surf. Sci.*, vol. 411, no. 3, pp. 249–262, Aug. 1998.

[7] E. Antolini, "The problem of Ru dissolution from Pt–Ru catalysts during fuel cell operation: analysis and solutions," *J. Solid State Electrochem.*, vol. 15, no. 3, pp. 455–472, Jun. 2010.

[8] H. A. Gasteiger, N. Markovic, P. N. Ross, and E. J. Cairns, "Carbon monoxide electrooxidation on well-characterized platinum-ruthenium alloys," *J. Phys. Chem.*, vol. 98, no. 2, pp. 617–625, Jan. 1994.

[9] D. Gerteisen, "Realising a reference electrode in a polymer electrolyte fuel cell by laser ablation," *J. Appl. Electrochem.*, vol. 37, no. 12, pp. 1447–1454, Nov. 2007.

[10] D. Gerteisen, "Transient and steady-state analysis of catalyst poisoning and mixed potential formation in direct methanol fuel cells," *J. Power Sources*, vol. 195, no. 19, pp. 6719–6731, Oct. 2010.

[11] P. Piela, C. Eickes, E. Brosha, F. Garzon, and P. Zelenay, "Ruthenium Crossover in Direct Methanol Fuel Cell with Pt-Ru Black Anode," *J. Electrochem. Soc.*, vol. 151, no. 12, p. A2053, 2004.

[12] Forschungszentrum Jülich, *IEF-3 Report 2007: von Grundlagen bis zum System*. Jülich: Forschungszentrum Jülich GmbH, 2007.

[13] N. Kimiaie, K. Wedlich, M. Hehemann, R. Lambertz, M. Müller, C. Korte, and D. Stolten, "Results of a 20 000 h lifetime test of a 7 kW direct methanol fuel cell (DMFC) hybrid system – degradation of the DMFC stack and the energy storage," *Energy Environ. Sci.*, vol. 7, no. 9, p. 3013, Jun. 2014.

[14] T. I. Valdez, S. Firdosy, B. Koel, and S. R. Narayanan, "Investigation of Ruthenium Dissolution in Advanced Membrane Electrode Assemblies for Direct Methanol Based Fuel Cell Stacks," 2006, vol. 1, pp. 293–303.

[15] Z.-B. Wang, H. Rivera, X.-P. Wang, H.-X. Zhang, P.-X. Feng, E. A. Lewis, and E. S. Smotkin, "Catalyst failure analysis of a direct methanol fuel cell membrane electrode assembly," *J. Power Sources*, vol. 177, no. 2, pp. 386–392, Mar. 2008.

[16] Z.-B. Wang, X.-P. Wang, P.-J. Zuo, B.-Q. Yang, G.-P. Yin, and X.-P. Feng, "Investigation of the performance decay of anodic PtRu catalyst with working time of direct methanol fuel cells," *J. Power Sources*, vol. 181, no. 1, pp. 93–100, Jun. 2008.

[17] D. Dixon, K. Wippermann, J. Mergel, A. Schoekel, S. Zils, and C. Roth, "Degradation effects at the methanol inlet, outlet and center region of a stack MEA operated in DMFC," *J. Power Sources*, vol. 196, no. 13, pp. 5538–5545, Jul. 2011.

[18] T. Arlt, I. Manke, K. Wippermann, C. Tötzke, H. Markötter, H. Riesemeier, J. Mergel, and J. Banhart, "Investigation of the three-dimensional ruthenium distribution in fresh and aged

membrane electrode assemblies with synchrotron X-ray absorption edge tomography," *Electrochem. Commun.*, vol. 13, no. 8, pp. 826–829, Aug. 2011.
[19] P. Hartmann and D. Gerteisen, "Local degradation analysis of a real long-term operated DMFC stack MEA," *J. Power Sources*, vol. 219, pp. 147–154, Dec. 2012.
[20] N. Wongyao, A. Therdthianwong, S. Therdthianwong, S. M. Senthil Kumar, and K. Scott, "A comparison of direct methanol fuel cell degradation under different modes of operation," *Int. J. Hydrog. Energy*, vol. 38, no. 22, pp. 9464–9473, Jul. 2013.
[21] G.-S. Park, C. Pak, Y.-S. Chung, J.-R. Kim, W. S. Jeon, Y.-H. Lee, K. Kim, H. Chang, and D. Seung, "Decomposition of Pt–Ru anode catalysts in direct methanol fuel cells," *J. Power Sources*, vol. 176, no. 2, pp. 484–489, Feb. 2008.
[22] T. T. H. Cheng, N. Jia, and P. He, "Characterization of the Degree of Ru Crossover and Its Performance Implications in Polymer Electrolyte Membrane Fuel Cells," *J. Electrochem. Soc.*, vol. 157, no. 5, p. B714, 2010.
[23] M. K. Jeon, K. R. Lee, K. S. Oh, D. S. Hong, J. Y. Won, S. Li, and S. I. Woo, "Current density dependence on performance degradation of direct methanol fuel cells," *J. Power Sources*, vol. 158, no. 2, pp. 1344–1347, Aug. 2006.
[24] L. Liu, L. Zhang, X. Cheng, Y. Zhang, and Q. Fan, "On-Time Determination of Ru Crossover in DMFC," 2009, pp. 43–51.
[25] J.-Y. Park, K.-Y. Park, K. B. Kim, Y. Na, H. Cho, and J.-H. Kim, "Influence and mitigation methods of reaction intermediates on cell performance in direct methanol fuel cell system," *J. Power Sources*, vol. 196, no. 13, pp. 5446–5452, Jul. 2011.
[26] A. R. Corpuz, T. S. Olson, P. Joghee, S. Pylypenko, A. A. Dameron, H. N. Dinh, K. J. O'Neill, K. E. Hurst, G. Bender, T. Gennett, B. S. Pivovar, R. M. Richards, and R. P. O'Hayre, "Effect of a nitrogen-doped PtRu/carbon anode catalyst on the durability of a direct methanol fuel cell," *J. Power Sources*, vol. 217, pp. 142–151, Nov. 2012.
[27] T. Arlt, I. Manke, K. Wippermann, H. Riesemeier, J. Mergel, and J. Banhart, "Investigation of the local catalyst distribution in an aged direct methanol fuel cell MEA by means of differential synchrotron X-ray absorption edge imaging with high energy resolution," *J. Power Sources*, vol. 221, pp. 210–216, Jan. 2013.
[28] Z.-B. Wang, X.-P. Wang, P.-J. Zuo, B.-Q. Yang, G.-P. Yin, and X.-P. Feng, "Investigation of the performance decay of anodic PtRu catalyst with working time of direct methanol fuel cells," *J. Power Sources*, vol. 181, no. 1, pp. 93–100, Jun. 2008.
[29] B. J. Hwang, L. S. Sarma, C. H. Chen, M. T. Tang, D. G. Liu, and J. F. Lee, "Depth profile of alloying extent and composition in bimetallic nanoparticles investigated by in situ x-ray absorption spectroscopy," *Appl. Phys. Lett.*, vol. 91, no. 2, p. 023108, 2007.
[30] D. Dixon, K. Wippermann, J. Mergel, A. Schoekel, S. Zils, and C. Roth, "Degradation effects at the methanol inlet, outlet and center region of a stack MEA operated in DMFC," *J. Power Sources*, vol. 196, no. 13, pp. 5538–5545, Jul. 2011.
[31] S. Stoupin, E.-H. Chung, S. Chattopadhyay, C. U. Segre, and E. S. Smotkin, "Pt and Ru X-ray Absorption Spectroscopy of PtRu Anode Catalysts in Operating Direct Methanol Fuel Cells," *J. Phys. Chem. B*, vol. 110, no. 20, pp. 9932–9938, May 2006.
[32] Z. Liang, W. Chen, J. Liu, S. Wang, Z. Zhou, W. Li, G. Sun, and Q. Xin, "FT-IR study of the microstructure of Nafion® membrane," *J. Membr. Sci.*, vol. 233, no. 1–2, pp. 39–44, Apr. 2004.
[33] A. Alentiev, J. Kostina, and G. Bondarenko, "Chemical aging of Nafion: FTIR study," *Desalination*, vol. 200, no. 1–3, pp. 32–33, Nov. 2006.
[34] N. M. Marković, T. J. Schmidt, V. Stamenković, and P. N. Ross, "Oxygen Reduction Reaction on Pt and Pt Bimetallic Surfaces: A Selective Review," *Fuel Cells*, vol. 1, no. 2, pp. 105–116, Jul. 2001.

[35] F. A. de Bruijn, V. A. T. Dam, and G. J. M. Janssen, “Review: Durability and Degradation Issues of PEM Fuel Cell Components,” *Fuel Cells*, vol. 8, no. 1, pp. 3–22, Feb. 2008.
[36] J.-M. Leger and C. Lamy, “The Direct Oxidation of Methanol at Platinum Based Catalytic Electrodes: What is New Since Ten Years?,” *Berichte Bunsenges. Für Phys. Chem.*, vol. 94, no. 9, pp. 1021–1025, Sep. 1990.
[37] B. Beden, F. Kadirgan, C. Lamy, and J. M. Leger, “Electrocatalytic oxidation of methanol on platinum-based binary electrodes,” *J. Electroanal. Chem. Interfacial Electrochem.*, vol. 127, no. 1–3, pp. 75–85, Oct. 1981.
[38] L. Dubau, C. Coutanceau, E. Garnier, J.-M. Léger, and C. Lamy, “Electrooxidation of methanol at platinum–ruthenium catalysts prepared from colloidal precursors: Atomic composition and temperature effects,” *J. Appl. Electrochem.*, vol. 33, pp. 419–429, 2003.
[39] E. A. Batista, G. R. P. Malpass, A. J. Motheo, and T. Iwasita, “New mechanistic aspects of methanol oxidation,” *J. Electroanal. Chem.*, vol. 571, no. 2, pp. 273–282, Oct. 2004.
[40] Y. Ishikawa, M.-S. Liao, and C. R. Cabrera, “Oxidation of methanol on platinum, ruthenium and mixed Pt–M metals (M=Ru, Sn): a theoretical study,” *Surf. Sci.*, vol. 463, no. 1, pp. 66–80, Aug. 2000.
[41] C. Roth, A. J. Papworth, I. Hussain, R. J. Nichols, and D. J. Schiffrin, “A Pt/Ru nanoparticulate system to study the bifunctional mechanism of electrocatalysis,” *J. Electroanal. Chem.*, vol. 581, no. 1, pp. 79–85, Jul. 2005.
[42] P. Liu, A. Logadottir, and J. K. Nørskov, “Modeling the electro-oxidation of CO and H2/CO on Pt, Ru, PtRu and Pt3Sn,” *Electrochimica Acta*, vol. 48, no. 25–26, pp. 3731–3742, Nov. 2003.
[43] H. Nitani, T. Nakagawa, H. Daimon, Y. Kurobe, T. Ono, Y. Honda, A. Koizumi, S. Seino, and T. A. Yamamoto, “Methanol oxidation catalysis and substructure of PtRu bimetallic nanoparticles,” *Appl. Catal. Gen.*, vol. 326, no. 2, pp. 194–201, Jul. 2007.
[44] J. W. Long, R. M. Stroud, K. E. Swider-Lyons, and D. R. Rolison, “How To Make Electrocatalysts More Active for Direct Methanol OxidationAvoid PtRu Bimetallic Alloys!,” *J. Phys. Chem. B*, vol. 104, no. 42, pp. 9772–9776, Oct. 2000.
[45] T. P. Luxton, M. J. Eick, and K. G. Scheckel, “Characterization and dissolution properties of ruthenium oxides,” *J. Colloid Interface Sci.*, vol. 359, no. 1, pp. 30–39, Jul. 2011.
[46] K. Totsuka, “Investigation of Reaction Mechanisms of Direct Methanol Fuel Cell by Quantitative Analysis of Effluents,” *JARI Res. J.*, vol. 24, no. 2, 2002.
[47] K. Totsuka, S. Watanabe, and T. Haraguchi, “Effect of Particle Size of Anode Catalyst for Direct Methanol Fuel Cell on Formation of Formic Acid and Formaldehyde,” *J. Soc. Powder Technol. Jpn.*, vol. 43, no. 2, pp. 92–97, 2006.
[48] Z. Qi and A. Kaufman, “Open circuit voltage and methanol crossover in DMFCs,” *J. Power Sources*, vol. 110, no. 1, pp. 177–185, Jul. 2002.
[49] A. Jablonski, P. J. Kulesza, and A. Lewera, “Oxygen permeation through Nafion 117 membrane and its impact on efficiency of polymer membrane ethanol fuel cell,” *J. Power Sources*, vol. 196, no. 10, pp. 4714–4718, May 2011.
[50] J. B. Benziger, M. B. Satterfield, W. H. J. Hogarth, J. P. Nehlsen, and I. G. Kevrekidis, “The power performance curve for engineering analysis of fuel cells,” *J. Power Sources*, vol. 155, no. 2, pp. 272–285, Apr. 2006.
[51] J. Larminie, *Fuel cell systems explained*. Chichester [England] ; New York: Wiley, 2000.
[52] M. J. N. Pourbaix, J. Van Muylder, and N. de Zoubov, “Electrochemical Properties of the Platinum Metals,” *Platin. Met. Rev.*, vol. 3, no. 3, pp. 100–106, 1959.
[53] M. Pourbaix, *Atlas of electrochemical equilibria in aqueous solutions.* [S.l.]: Nat’L Assoc. Of Corrosion, 1974.

[54] D. Liu, J. Lee, and M. Tang, “Characterization of Pt-Ru/C catalysts by X-ray absorption spectroscopy and temperature-programmed surface reaction,” *J. Mol. Catal. Chem.*, Aug. 2005.
[55] C. Roth, N. Benker, M. Mazurek, F. Scheiba, and H. Fuess, “Pt-Ru fuel cell catalysts subjected to H2, CO, N2 and air atmosphere: An X-ray absorption study,” *Appl. Catal. Gen.*, vol. 319, pp. 81–90, Mar. 2007.
[56] B. J. Hwang, C.-H. Chen, L. S. Sarma, J.-M. Chen, G.-R. Wang, M.-T. Tang, D.-G. Liu, and J.-F. Lee, “Probing the Formation Mechanism and Chemical States of Carbon-Supported Pt−Ru Nanoparticles by in Situ X-ray Absorption Spectroscopy,” *J. Phys. Chem. B*, vol. 110, no. 13, pp. 6475–6482, Apr. 2006.
[57] A. J. Frenkel, M. S. Nashner, C. W. Hills, R. G. Nuzzo, and J. R. Shapley, “Evolution of Pt-Ru catalysts from molecular precursors to bimetallic nanoparticles,” *NSLS Act. Rep.*, pp. 50–53, 1999.
[58] C. Roth, N. Benker, S. Zils, R. Chenitz, A. Issanin, and H. Fuess, “The Oxidation Behaviour of Ruthenium in the Presence of Platinum and its Effect on the Electrocatalytic Activity of Pt-Ru Fuel Cell Catalysts,” *Z. Für Phys. Chem.*, vol. 221, no. 11–12, pp. 1549–1567, Dec. 2007.
[59] V. Radmilovic, “Structure and Chemical Composition of a Supported Pt-Ru Electrocatalyst for Methanol Oxidation,” *J. Catal.*, vol. 154, no. 1, pp. 98–106, Jun. 1995.
[60] D. R. Rolison, P. L. Hagans, K. E. Swider, and J. W. Long, “Role of Hydrous Ruthenium Oxide in Pt−Ru Direct Methanol Fuel Cell Anode Electrocatalysts: The Importance of Mixed Electron/Proton Conductivity,” *Langmuir*, vol. 15, no. 3, pp. 774–779, Feb. 1999.
[61] M. Gasik and M. & M. Institute of Materials, *Materials for fuel cells*. Cambridge; Boca Raton: Woodhead Pub. and Maney Pub. on behalf of the Institute of Materials, Minerals & Mining ; CRC Press, 2008.
[62] T. Loučka, “The potential-pH diagram for the Ru−H2O−Cl− system at 25°C,” *J. Appl. Electrochem.*, vol. 20, no. 3, pp. 522–523, May 1990.
[63] T. M. Arruda, B. Shyam, J. S. Lawton, N. Ramaswamy, D. E. Budil, D. E. Ramaker, and S. Mukerjee, “Fundamental Aspects of Spontaneous Cathodic Deposition of Ru onto Pt/C Electrocatalysts and Membranes under Direct Methanol Fuel Cell Operating Conditions: An in Situ X-ray Absorption Spectroscopy and Electron Spin Resonance Study,” *J. Phys. Chem. C*, vol. 114, no. 2, pp. 1028–1040, Jan. 2010.
[64] Y. Sugawara, A. P. Yadav, A. Nishikata, and T. Tsuru, “EQCM Study on Dissolution of Ruthenium in Sulfuric Acid,” *J. Electrochem. Soc.*, vol. 155, no. 9, p. B897, 2008.
[65] Y. Park, B. Lee, C. Kim, Y. Oh, S. Nam, and B. Park, “The effects of ruthenium-oxidation states on Ru dissolution in PtRu thin-film electrodes,” *J. Mater. Res.*, vol. 24, no. 09, pp. 2762–2766, Feb. 2011.
[66] S. Mukerjee, L. Gancs, B. N. Hult, and N. Hakim, “The Impact of Ru Contamination of a Pt⁄C Electrocatalyst on Its Oxygen-Reducing Activity,” *Electrochem. Solid-State Lett.*, vol. 10, no. 9, p. B150, 2007.
[67] B. M. Gordon, “Sensitivity calculations for multielemental trace analysis by synchrotron radiation induced X-ray fluorescence,” *Nucl. Instrum. Methods Phys. Res.*, vol. 204, no. 1, pp. 223–229, Dec. 1982.
[68] W. M. Kwiatek, B. Kubica, C. Paluszkiewicz, and M. Gałka, “Trace element analysis by means of synchrotron radiation, XRF, and PIXE: selection of sample preparation procedure,” *J. Alloys Compd.*, vol. 328, no. 1–2, pp. 283–288, Oct. 2001.
[69] U. Metz, P. Hoffmann, S. Weinbruch, and H. M. Ortner, “A comparison of X-ray fluorescence spectrometric (XRF) techniques for the determination of metal traces, especially in plastics,” *Mikrochim. Acta*, vol. 117, no. 1–2, pp. 95–108, Mar. 1994.
[70] A. J. Klimasara, “XRF Analysis - Theory, Experiment and Regression,” *ICDD Adv. X-Ray Anal.*, vol. 40, 1997.

[71] A. Kuczumow, Z. Rzączyńska, and M. Szewczak, “Matrix effects in the x-ray fluorescence method,” *X-Ray Spectrom.*, vol. 11, no. 3, pp. 135–139, Jul. 1982.
[72] S. Pessanha, A. Guilherme, and M. L. Carvalho, “Comparison of matrix effects on portable and stationary XRF spectrometers for cultural heritage samples,” *Appl. Phys. A*, vol. 97, no. 2, pp. 497–505, May 2009.
[73] J. M. Ablett, J. C. Woicik, and C. C. Kao, “New Correction Procedure for X-ray Spectroscopic Fluorescence Data: Simulations and Experiment,” *ICDD Adv. X-Ray Anal.*, vol. 48, 2005.
[74] F. R. Feret, H. Hamouche, and Y. Boissonneault, “Spectral Interference in X-ray Fluorescence Analysis of Common Materials,” *ICDD Adv. X-Ray Anal.*, vol. 46, 2003.
[75] P. Lechner, C. Fiorini, R. Hartmann, J. Kemmer, N. Krause, P. Leutenegger, A. Longoni, H. Soltau, D. Stötter, R. Stötter, L. Strüder, and U. Weber, “Silicon drift detectors for high count rate X-ray spectroscopy at room temperature,” *Nucl. Instrum. Methods Phys. Res. Sect. Accel. Spectrometers Detect. Assoc. Equip.*, vol. 458, no. 1–2, pp. 281–287, Feb. 2001.
[76] W. T. Elam, B. Scruggs, M. Solazzi, and J. Nicolosi, “Improving Trace Element Detection in EDXRF by Reducing Pileup Artifacts,” *Adv. X Ray Anal. - CD-ROM Ed.*, vol. 52, no. 12, 2009.
[77] G.-B. Jung, C.-H. Tu, P.-H. Chi, A. Su, F.-B. Weng, Y.-T. Lin, Y.-C. Chiang, C.-Y. Lee, and W.-M. Yan, “Investigations of flow field designs in direct methanol fuel cell,” *J. Solid State Electrochem.*, vol. 13, no. 9, pp. 1455–1465, Nov. 2008.
[78] C. Roth, “Strukturelle und elektrochemische Charakterisierung rußgeträgerter Pt-Ru und Pt-Ru-W Katalysatoren für die Anwendung in Membran-Brennstoffzellen.” ULB Darmstadt, 17-Oct-2008.
[79] V. A. Solé, E. Papillon, M. Cotte, P. Walter, and J. Susini, “A multiplatform code for the analysis of energy-dispersive X-ray fluorescence spectra,” *Spectrochim. Acta Part B At. Spectrosc.*, vol. 62, no. 1, pp. 63–68, Jan. 2007.
[80] F. Ettingshausen, J. Kleemann, A. Marcu, G. Toth, H. Fuess, and C. Roth, “Dissolution and Migration of Platinum in PEMFCs Investigated for Start/Stop Cycling and High Potential Degradation,” *Fuel Cells*, vol. 11, no. 2, pp. 238–245, Apr. 2011.
[81] F. Ettingshausen, “Elektrodendegradation in Polymerelektrolyt-Membran-Brennstoffzellen = Electrode degradation in polymer electrolyte membrane fuel cells,” Cuvillier, Göttingen, 2011.
[82] G. Bunker, *Introduction to XAFS: a practical guide to X-ray absorption fine structure spectroscopy*. Cambridge, UK; New York: Cambridge University Press, 2010.
[83] M. Newville, “IFEFFIT: interactive EXAFS analysis and FEFF fitting,” *J Synchrotron Rad*, vol. 8, pp. 322–324, 2001.
[84] B. Ravel and M. Newville, “ATHENA, ARTEMIS, HEPHAESTUS: data analysis for X-ray absorption spectroscopy using IFEFFIT,” *J. Synchrotron Radiat.*, vol. 12, no. 4, pp. 537–541, Jun. 2005.
[85] D. Beauchemin, “Inductively Coupled Plasma Mass Spectrometry,” *Anal. Chem.*, vol. 82, no. 12, pp. 4786–4810, Jun. 2010.
[86] S. F. Boulyga and K. G. Heumann, “Direct determination of platinum group elements and their distributions in geological and environmental samples at the ng g−1 level using LA–ICP–IDMS,” *Anal. Bioanal. Chem.*, vol. 383, no. 3, pp. 442–447, Aug. 2005.
[87] C. J. Corcoran, H. Tavassol, M. A. Rigsby, P. S. Bagus, and A. Wieckowski, “Application of XPS to study electrocatalysts for fuel cells,” *J. Power Sources*, vol. 195, no. 24, pp. 7856–7879, Dec. 2010.
[88] K. L. Parry, A. G. Shard, R. D. Short, R. G. White, J. D. Whittle, and A. Wright, “Synthesis and characterisation of human transferrin-stabilized gold nanoclusters - Supporting information,” *Surf Interface Anal*, vol. 38, p. 1497, 2006.
[89] J. H. Scofield, “Hartree-Slater subshell photoionization cross-sections at 1254 and 1487 eV,” *J Electron Spectr Relat Phenom*, vol. 8, p. 129, 1976.

[90] S. Tanuma, C. J. Powell, and D. R. Penn, “Calculations of electron inelastic mean free paths. V. Data for 14 organic compounds over the 50-2000 eV range,” *Surf. Interface Anal.*, vol. 21, no. 3, pp. 165–176, Mar. 1994.
[91] W. Friedrich, P. Knipping, and M. Laue, “Interferenz-Erscheinungen bei Röntgenstrahlen (Interference appearances in X-rays),” *Proc. Bavar. Acad. Sci. Sber Bayer Akad Wiss*, pp. 303–322, 1912.
[92] W. H. Bragg and W. L. Bragg, “The Reflection of X-rays by Crystals,” *Proc. R. Soc. Math. Phys. Eng. Sci.*, vol. 88, no. 605, pp. 428–438, Jul. 1913.
[93] T. Hyde, “Final Analysis: Crystallite Size Analysis of Supported Platinum Catalysts by XRD,” *Platin. Met. Rev.*, vol. 52, no. 2, pp. 129–130, Apr. 2008.
[94] P. Scherrer, “Bestimmung der Größe und der inneren Struktur von Kolloidteilchen mittels Röntgenstrahlen,” *Nachrichten Von Ges. Wiss. Zu Gött.*, pp. 98–100, 1918.
[95] J. I. Langford and A. J. C. Wilson, “Scherrer after sixty years: A survey and some new results in the determination of crystallite size,” *J. Appl. Crystallogr.*, vol. 11, no. 2, pp. 102–113, Apr. 1978.
[96] J. Rodriguez-Carvajal, “FULLPROF: a program for Rietveld refinement and pattern matching analysis,” *Satell. Meet. Powder Diffr. XV Congr. IUCr*, vol. 127, Jul. 1990.
[97] J. Rodriguez-Carvajal, “Recent developments of the program FULLPROF,” *Comm. Powder Diffr. IUCr Newsl.*, vol. 26, pp. 12–19, Dec. 2001.
[98] J. Rodriguez-Carvajal and T. Roisnel, “FullProf. 98 and WinPLOTR: New Windows 95/NT Applications for Diffraction. Commission for Powder Diffraction, International Union of Crystallography,” *Newsletter*, vol. 20, p. 35, May 1998.
[99] T. Roisnel and J. Rodríguez-Carvajal, “WinPLOTR: A windows tool for powder diffraction pattern analysis,” *Mater. Sci. Forum*, vol. 378, no. 1, pp. 118–123, Oct. 2001.
[100] A. J. Bard, *Electrochemical methods: fundamentals and applications*, 2nd ed. New York: Wiley, 2001.
[101] R. Holze, *Experimental electrochemistry: a laboratory textbook*. Weinheim: Wiley-VCH, 2009.
[102] É. C. G. Rufino and P. Olivi, “The effect of methanol on the stability of Pt/C and Pt–RuOx/C catalysts,” *Int. J. Hydrog. Energy*, vol. 35, no. 24, pp. 13298–13308, Dec. 2010.
[103] S.-A. Sheppard, S. A. Campbell, J. R. Smith, G. W. Lloyd, F. C. Walsh, and T. R. Ralph, “Electrochemical and microscopic characterisation of platinum-coated perfluorosulfonic acid (Nafion 117) materials†,” *The Analyst*, vol. 123, no. 10, pp. 1923–1929, 1998.
[104] J. Melke, *Study of the ethanol oxidation in fuel cell operation using X-ray absorption spectroscopy and electrochemical methods*. Uelvesbüll: Der Andere Verl., 2011.
[105] R. J. Mathew and A. E. Russell, “XAS of carbon supported platinum fuel cell electrocatalysts: advances towards real time investigations,” *Top. Catal.*, vol. 10, no. 3/4, pp. 231–239, 2000.
[106] R. J. K. Wiltshire, C. R. King, A. Rose, P. P. Wells, M. P. Hogarth, D. Thompsett, and A. E. Russell, “A PEM fuel cell for in situ XAS studies,” *Electrochimica Acta*, vol. 50, no. 25–26, pp. 5208–5217, Sep. 2005.
[107] C. Roth, N. Martz, T. Buhrmester, J. Scherer, and H. Fuess, “In-situ XAFS fuel cell measurements of a carbon-supported Pt–Ru anode electrocatalyst in hydrogen and direct methanol operation,” *Phys. Chem. Chem. Phys.*, vol. 4, no. 15, pp. 3555–3557, Jul. 2002.
[108] M. Shao, P. Liu, J. Zhang, and R. Adzic, “Origin of Enhanced Activity in Palladium Alloy Electrocatalysts for Oxygen Reduction Reaction,” *J. Phys. Chem. B*, vol. 111, no. 24, pp. 6772–6775, Jun. 2007.
[109] X. Li, Q. Huang, Z. Zou, B. Xia, and H. Yang, “Low temperature preparation of carbon-supported PdCo alloy electrocatalysts for methanol-tolerant oxygen reduction reaction,” *Electrochimica Acta*, vol. 53, no. 22, pp. 6662–6667, Sep. 2008.

[110] H. Chan, “High-Pressure Oxidation of Ruthenium as Probed by Surface-Enhanced Raman and X-Ray Photoelectron Spectroscopies,” *J. Catal.*, vol. 172, no. 2, pp. 336–345, Dec. 1997.
[111] D. Rochefort, P. Dabo, D. Guay, and P. M. A. Sherwood, “XPS investigations of thermally prepared RuO2 electrodes in reductive conditions,” *Electrochimica Acta*, vol. 48, no. 28, pp. 4245–4252, Dec. 2003.
[112] E. Antolini, L. Giorgi, F. Cardellini, and E. Passalacqua, “Physical and morphological characteristics and electrochemical behaviour in PEM fuel cells of PtRu/C catalysts,” *J. Solid State Electrochem.*, vol. 5, no. 2, pp. 131–140, Feb. 2001.
[113] A. S. Aricò, P. L. Antonucci, E. Modica, V. Baglio, H. Kim, and V. Antonucci, “Effect of Pt-Ru alloy composition on high-temperature methanol electro-oxidation,” *Electrochimica Acta*, vol. 47, no. 22–23, pp. 3723–3732, Aug. 2002.
[114] M. S. Paterson, “X-Ray Diffraction by Face-Centered Cubic Crystals with Deformation Faults,” *J. Appl. Phys.*, vol. 23, no. 8, p. 805, 1952.
[115] A. I. Ustinov and N. M. Budarina, “Influence of planar defects on powder diffractograms of fcc metals,” *Powder Diffr.*, vol. 17, no. 04, pp. 270–277, Mar. 2012.
[116] T. Kandemir, I. Kasatkin, F. Girgsdies, S. Zander, S. Kühl, M. Tovar, R. Schlögl, and M. Behrens, “Microstructural and Defect Analysis of Metal Nanoparticles in Functional Catalysts by Diffraction and Electron Microscopy: The Cu/ZnO Catalyst for Methanol Synthesis,” *Top. Catal.*, vol. 57, no. 1–4, pp. 188–206, Feb. 2014.
[117] C. Solliard and M. Flueli, “Surface stress and size effect on the lattice parameter in small particles of gold and platinum,” *Surf. Sci.*, vol. 156, pp. 487–494, Jun. 1985.
[118] C.-M. Lai, J.-C. Lin, K.-L. Hsueh, C.-P. Hwang, K.-C. Tsay, L.-D. Tsai, and Y.-M. Peng, “On the Accelerating Degradation of DMFC at Highly Anodic Potential,” *J. Electrochem. Soc.*, vol. 155, no. 8, p. B843, 2008.
[119] B. J. Hwang, Y. W. Tsai, J. F. Lee, P. Borthen, and H. H. Strehblow, “In situ EXAFS investigation of carbon-supported Pt clusters under potential control,” *J. Synchrotron Radiat.*, vol. 8, no. Pt 2, pp. 484–486, Mar. 2001.
[120] W. Chen, G. Sun, Z. Liang, Q. Mao, H. Li, G. Wang, Q. Xin, H. Chang, C. Pak, and D. Seung, “The stability of a PtRu/C electrocatalyst at anode potentials in a direct methanol fuel cell,” *J. Power Sources*, vol. 160, no. 2, pp. 933–939, Oct. 2006.
[121] J.-Y. Park, M. A. Scibioh, S.-K. Kim, H.-J. Kim, I.-H. Oh, T. G. Lee, and H. Y. Ha, “Investigations of performance degradation and mitigation strategies in direct methanol fuel cells,” *Int. J. Hydrog. Energy*, vol. 34, no. 4, pp. 2043–2051, Feb. 2009.
[122] G. Lodi, E. Sivieri, A. Battisti, and S. Trasatti, “Ruthenium dioxide-based film electrodes: III. Effect of chemical composition and surface morphology on oxygen evolution in acid solutions,” *J. Appl. Electrochem.*, vol. 8, no. 2, pp. 135–143, Mar. 1978.
[123] B. E. Conway, V. Birss, and J. Wojtowicz, “The role and utilization of pseudocapacitance for energy storage by supercapacitors,” *J. Power Sources*, vol. 66, no. 1–2, pp. 1–14, May 1997.
[124] B. E. Conway, “The Electrochemical Behavior of Ruthenium Oxide (RuO2) as a Material for Electrochemical Capacitors,” in *Electrochemical Supercapacitors*, Boston, MA: Springer US, 1999, pp. 259–297.
[125] S. Hurter, M. Muller, K. Wippermann, M. D. Guiver, L. Scoles, and D. Stolten, “Membrane Electrode Assemblies Based on Hydrocarbon Electrolytes with Nitrile Groups for Direct Methanol Fuel Cells,” *ECS Trans.*, vol. 50, no. 2, pp. 2139–2149, Mar. 2013.
[126] Q. Zhang, B. Liu, W. Hu, W. Xu, Z. Jiang, W. Xing, and M. D. Guiver, “Poly(arylene ether) electrolyte membranes bearing aliphatic-chain-linked sulfophenyl pendant groups,” *J. Membr. Sci.*, vol. 428, pp. 629–638, Feb. 2013.